Body Deformation Correction for SPECT Imaging

Songxiang Gu

A dissertation submitted to the faculty of Worcester Polytechnic Institute in partial fulfillment of the requirements for the degree of Doctor of Philosophy in the Department of Computer Science.

7-8-2009

Approved by:

Prof. Michael A. Gennert, Advisor

Prof. Michael A. King, Co-advisor

Prof. Matthew O. Ward , Committee Member

Prof. Emmanuel Agu, Committee Member

Prof. Stephen C. Moore, Committee Member

ABSTRACT

Single Photon Emission Computed Tomography (SPECT) is a medical imaging modality that allows us to visualize functional information about a patient's specific organ or body systems. During 20 minute scan, patients may move. Such motion will cause misalignment in the reconstruction, degrade the quality of 3D images and potentially lead to errors in diagnosis. Body bend and twist are types of patient motion that may occur during SPECT imaging and which has been generally ignored in SPECT motion correction strategies. To correct for these types of motion we propose a deformation model and its inclusion within an iterative reconstruction algorithm. One simulation and three experiments were conducted to investigate the applicability of our model. The simulation employed simulated projections of the MCAT phantom formed using an analytical projector which includes attenuation and distance-dependent resolution to investigate applications of our model in reconstruction. We demonstrate in the simulation studies that twist and bend can significantly degrade SPECT image quality visually. Our correction strategy is shown to be able to greatly diminish the degradation seen in the slices, provided the parameters are estimated accurately. To verify the correctness of our deformation model, we design the first experiment. In this experiment, the return of the post-motion-compensation locations of markers on the body-surface of a volunteer to approximate their original coordinates is used to examine our method of estimating the parameters of our model and the parameters' use in undoing deformation. Then, we design an MRI based experiment to validate our deformation model without any reconstruction. We use the surface marker motion to alter an MRI body volume to compensate the deformation the volunteer undergoes during data acquisition, and compare the motion-compensated volume with the motionless volume. Finally, an experiment with SPECT acquisitions and modified MLEM algorithm is designed to show the contribution of our deformation correction for clinical SPECT imaging. We view this work as a first step towards being able to estimate and correct patient deformation based on information obtained from marker tracking data.

ACKNOWLEDGMENTS

I have to thank Professors Michael A. Gennert and Michael A. King for their guidance and advice throughout the project. I'd like to thank Joseph McNamara for his helpful comments and assistance. By the way, he did fix a lot of equipment that I broke. Also thank Karen Johnson for the clinic data. Thanks to Howard Gifford, Andre Lehovich, Joyoni Dey, Joyeeta Mitra, Hendrik Pretorius and Yu Chen for all their selfless help. Without them, I could not finish this project.

Thank all of you again.

TABLE OF CONTENTS

LIST OF TABLES

LIST OF FIGURES

LIST OF ABBREVIATIONS

SPECT	Single Photon Emission Computed Tomography
MLEM	Maximum-Likelihood Expectation-Maximization
DOF	Degrees of Freedom
MRI	Magnetic Resonance Imaging
NCAT	Nurbs-based Cardiac-Torso
MCAT	Mathematical Cardiac Torso
VTS	Visual Tracking System
FBP	Filter Back-Projection
OSEM	Ordered-Subset Expectation-Maximization
PET	Positron Emission Tomography
RBM	Rigid Body Motion
RM	Respiratory Motion
ROI	region of interest

Chapter 1

Introduction

1.1 Motivation

1.1.1 Single Photon Emission Computed Tomography (SPECT) Imaging

SPECT is a nuclear imaging modality that allows us to visualize functional information about patients' specific organs, such as the heart, lung and liver. Before imaging, a pharmaceutical labeled with a radioactive isotope is either injected, ingested or inhaled. Such a pharmaceutical is called a radiopharmaceutical, or tracer. While the patient lies supine in the SPECT machine, the tracer decays, resulting in the emission of gamma rays from regions of high uptake. A gamma camera collects gamma rays that are emitted from within organs of interest, allowing us to acquire 2-dimensional projections (Figure 1.1). Each projection is a sum of the body perfusion volume in one direction. Usually, 68 angular samples are required for one SPECT imaging process. With these projections, a 3D reconstruction algorithm, such as Maximum-Likelihood Expectation-Maximization (MLEM) or Filter Back-Projection (FBP), reconstructs the 3D body volume. Ideally, the reconstructed 3D body volume is an accurate reflection of the real organ function.

SPECT is complementary with CT or Magnetic Resonance Imaging (MRI) which are both structural imaging modalities. Typically, SPECT imaging needs 20 minutes to acquire the 2D projections of a patient. During that long imaging time patients inevitably has some movement. Such movements cause misalignment in the projections,

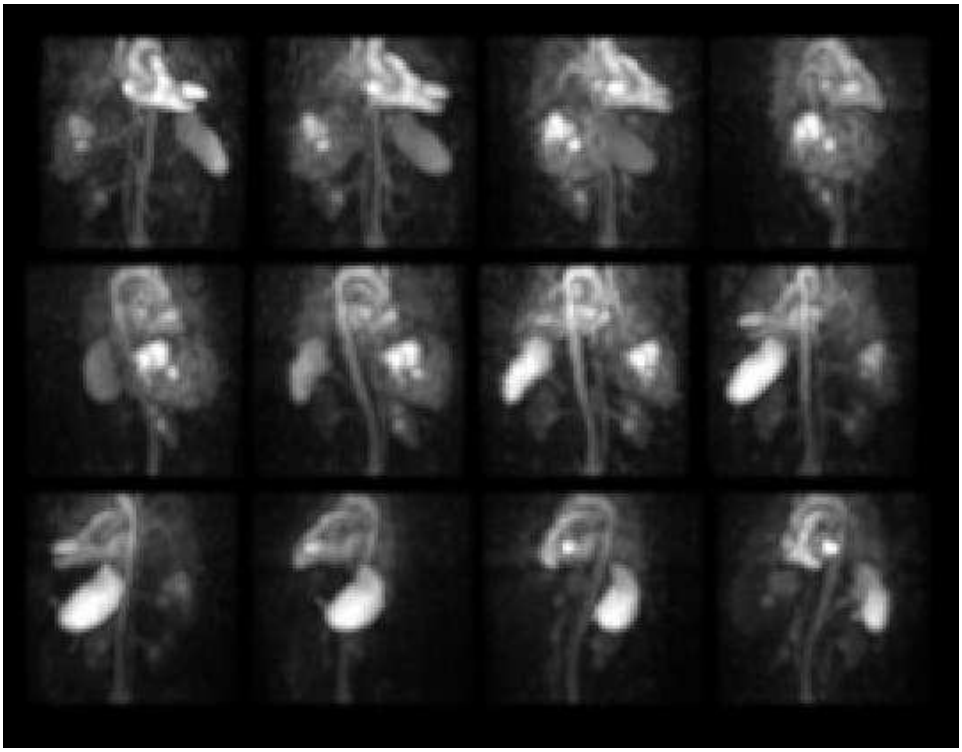

Figure 1.1: Projections by SPECT Imaging. (Wang and Royal, 1996)

which, in turn, degrades the imaging quality. To improve the quality of the SPECT imaging, we have to correct for such misalignments.

Since such misalignment is caused by the patient motion, we need to answer the following questions: 1) how many kinds of motion might a patient have during the imaging, 2) how to measure those motions and 3) how to use the motion information to correct within the reconstruction and improve the final imaging results.

1.1.2 Motion Categories

Patient motion is mostly composed of Rigid Body Motion (RBM), Respiratory Motion (RM) and non-rigid body motion. Each kind of motion has its own properties and has to be treated independently. For RBM, we can consider the patient as a whole object and omit the relative movement between the patient organs. Therefore, RBM is described by 3 Degrees of Freedom (DOF) of patient translation and 3 DOF of patient rotation (Feng et al., 2003).

Respiratory motion is another type of motion. The property of this motion is that the patient organs are driven by periodic breathing, but in considering the patient as a whole, there is no movement. So we can say the respiratory motion is a special non-rigid periodic motion. A lot of work (Reyes et al., 2007) (Lamare et al., 2007) has been done to measure and compensate for this motion.

The third kind of motion, which we focus on in this dissertation, is non-rigid and non-periodic body motion, or so called body deformation. This happens when a patient changes his pose. During SPECT imaging, a patient lies supine on the table for about 20 minutes. Patient deformation usually occurs if the patient feels uncomfortable during the SPECT imaging. It is especially difficult for some older patients, who are the majority of patients requiring scans, to maintain the same position for up to 20 minutes. After a patient changes his pose, such as by twisting his body and stretching his arms, the relative distances between organs are also changed. Just as for the other two motions, body deformation also changes the body volume. As shown in Figure 1.2, such body deformation will change the density of the gamma ray emission distribution and, in turn, will alter the projections. If we ignore such an influence and perform a reconstruction as before, some parts of the body may be brightened abnormally, while some other parts of the body may appear abnormally dark. Unfortunately, such abnormal hot or cold spots in the 3D reconstruction volume might be considered as disease in the diagnosis (Figure 1.3).

1.1.3 Motion Measurement

Motion measurement and motion estimation is an important part of SPECT imaging correction. Though we are aware of all the kinds of motions, we have to find a way to measure them during the imaging process. There are two major methods for motion capture. Firstly, we have to quantify the patient motion by the projections themselves. In this approach, each projection image is separated by different time windows. Then a registration method is used to estimate the motion between the frames (Kyme et al., 2003). Currently, one of the major algorithms for image registration is optical flow based registration. This method is widely used for motion correction, especially in SPECT brain motion correction (Noumeir et al., 1996) (Cooper and Ritter, 2003). However, for the torso, the motion is more complex and non-periodic. To make it worse,

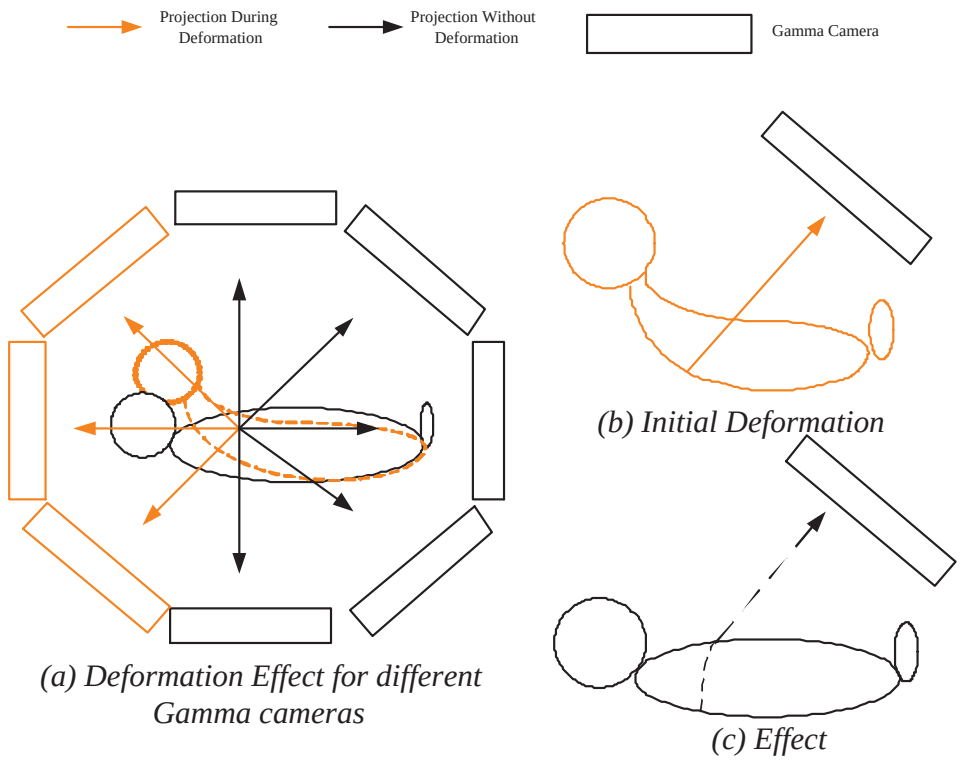

Figure 1.2: Body Deformation During the SPECT Imaging.

projections are acquired from different angles sequentially. We are lack of knowledge of the projection image without motion. Therefore, the optical flow registration can hardly help the torso motion during the reconstruction.

One important observation regarding patient motion is that internal body motion affects the patient surface motion inevitably. On the other hand, the patient surface motion is a good indicator of the internal body motion. If we can monitor the patient surface motion, this surface motion information can be used to infer the interior motion to some extent. In this project, we are trying to monitor the patient surface motion and estimate the patient body motion from the surface motion. It is true that the entire patient surface motion can not be monitored or described in an efficient way and can not be used within the reconstruction easily. To make it worse, the patient body is so complex and flexible that it is not easily separated from the background. This means that we can not get our motion data by monitoring the patient body directly. However, instead of tracking the whole patient surface, we can put some retro-reflective

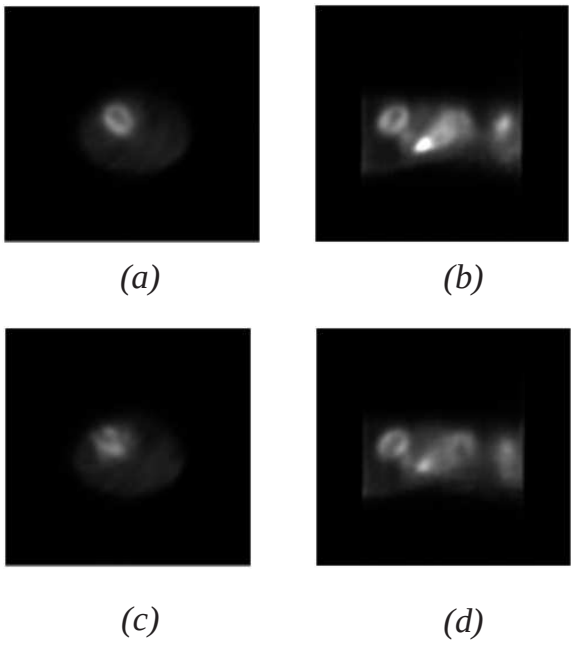

Figure 1.3: (a,b) Transverse (Coronal) slice from the reconstructed volume without motion effect; (c,d) Transverse (Coronal) slice from the reconstructed volume with some deformation effect.

markers on the patient body, which can be tracked with a set of cameras. The cameras are placed in various directions around the patient to avoid blocking views by the SPECT machine or the patient body anatomy. Since the patient motion can be closely represented by the retro-reflective markers, we try to track the motion of these markers and consider these markers' motion as an indicator of the patient surface motion.

There are several motion capture systems that can meet this requirement. For example, Bruyant (Bruyant et al., 2004) (Bruyant et al., 2002) developed a motion capture system, called a Visual Tracking System (VTS), to track patient motion with video cameras. Currently, we have adopted for clinical usage a commercial system (VICON MX, Oxford, UK) because of its flexibility and ease of calibration (McNamara et al., 2007). The markers are attached to elastic bands wrapped about the chest and abdomen of the patient. Figure 1.4 shows a volunteer in the supine imaging position on the table of our SPECT system with 2 bands with attached markers, and 2 of the 5 VICON cameras we employ for motion-tracking. In this project, we wrap two belts, each with 4-5 retro-reflective markers, on the chest and abdomen of the patient respectively.

Figure 1.4: Illustration of viewing geometry for markers on stretchy bands and a volunteer in the supine position for motion-tracking during SPECT imaging.

During the motion tracking, each camera records a sequence of marker images. If a marker is viewed by at least 2 cameras at one time, the 3D surface marker trajectories can be triangulated from 2D coordinates. The motion of the chest markers can be combined to estimate the RBM of the chest, and the vertical motion of markers on the abdomen allows us to track respiration (Mukherjee et al., 2009). Therefore, the patient surface motion is indicated by the markers' 3D coordinate sequences. Finally, the gross motion data will be determined from the position sequences of the markers. Once such gross motion data is acquired by the motion tracking system, a motion separation process (Mitra et al., 2007) is used to separate the motion into three compositions (RBM, RM and Deformation), which is described in the Section 1.1.2.

What we have considered so far is just the marker motion. A motion model is required to build the relationship between the marker's motion and the patient volume motion. With such a connection, we can use the marker's motion to correct within the volume reconstruction.

1.1.4 Reconstruction

A 3D reconstruction algorithm (Li et al., 1994) (Shepp and Vardi, 1982a) (Lange and Carson, 1984a) is used to build body volume data from 2D projection images. We can get 2D projection images from CT or SPECT. The structure is not very visible in

these projection images. To visualize it better, the 2D projection images have to be reconstructed to a 3D volume. Regardless of motion blur, the reconstruction algorithm uses all the projections to build a 3D body volume for clinical diagnosis.

When we take the patient motion into consideration, the reconstruction method has to be modified. Since we have to take the motion data into consideration, a set of details should be carefully considered, such as the reconstruction formula adjustment, volume data interpolation and synchronization between the projections and the motion data. For the iterative reconstruction algorithm, the iteration number to reach the best result also may have to be adjusted.

Of all the three kinds of motion, the correction of the RBM has been the most rigorously developed (Feng et al., 2005) (Feng et al., 2006). By inputting the RBM component, Feng (Feng et al., 2003) improved the reconstruction algorithm to correct the RBM effect within iterative reconstruction. The respiratory signal can also be used for RM correction (Dey et al., 2007) (Dey et al., 2006) (Ue et al., 2005) (Kovalski et al., 2007).

However, the human body is not a true rigid object. When the human body undergoes a motion, part of the body has to deform to reach the destination followed by other parts of the body, especially when the patient is lying down. Therefore, residual motion always present even after removing RBM and RM. In our analysis we will term such non-rigid non-periodic motion as body deformation. If there is some deformation component in the gross motion, the body organs undergo relative movements, which can not be corrected with the RBM and RM correction alone. Figure 1.5 shows the coordinate sequence of a chest marker for 12 minutes of a real SPECT acquisition. We can see that the patient moved unexpectedly after 10 minutes. This motion could not be described by RBM alone. Figure 1.6 shows this sample motion before and after the RBM correction. The residual motion of markers shows that the patient body was undergoing a deformation. Our aim will focus on the deformation correction within the reconstruction.

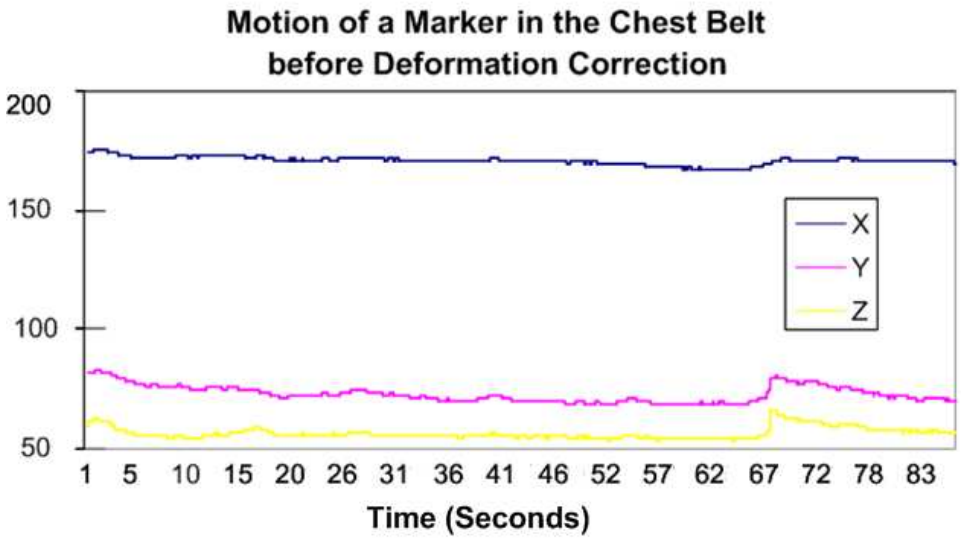

Figure 1.5: 3D coordinate sequence of a chest marker on patient body during a real SPECT acquisition.

1.2 Dissertation Overview

1.2.1 Project Description

The goal of this research is to eliminate or minimize the misalignment caused by body deformation in 3D volume reconstruction. Before we describe the project, we have to describe the input and output parameters. Basically, we have two kinds of input data. The first is the marker coordinates for deformation. After our cameras capture the marker motion; the motion separation module separates the motion into 3 parts based on the motion categories. We take the data for non-periodic and non-rigid deformation as our input motion data. The second part is the 3D volume reconstruction from 2D projections of SPECT. The 3D volume from the reconstruction module is the only output data.

There are many potential types of patient body deformation. In this dissertation, however, we focus on two kinds of deformation which involve the spine: twist and bend. We define twist as a progressive rotation around the backbone along the foot-head axis, and bend as a progressive curving along the backbone resulting in it being bent. Bend can occur in any direction; however a vertical bend upward (sitting up) would be difficult for a patient to maintain for any extended period. Thus lateral bending is the

more likely to occur when for example the patient wiggles to get comfortable. Therefore, the twist motion defines one degree of freedom—twist, and the bend motion defines two degrees of freedom—bend and bend direction. Our deformation computation deals with these three degrees of freedom. Without correcting for body deformation, the reconstruction will degenerate, which could impact diagnostic accuracy.

Even after we have acquired the marker data, we still have no specific idea of the patient torso deformation. We can consider the marker coordinates as a set of sparse points on the torso. How to use those sparse points to indicate the whole volume deformation is the question we have to answer. This paper presents three steps we have developed for correction of bending and twisting: 1) creation of a body model with parameters describing the extent of twist and bend, 2) using patient observations in the estimation of the deformation parameters of this model, and 3) image reconstruction employing the model and parameters. Our body model is for imaging in the chest and abdomen region, and is based on a simple mechanical model of the spine within that volume. That is, we assume the spine does not stretch or compress in length but just twists and bends (in addition to any RBM). A set of inherent body variables, such as the spine length and center, are specified to apply the model for each patient. The residual body deformation data remaining after removing RM and RBM from the set of marker motions are processed by the deformation model to estimate the deformation parameters (twist angle, bend angle, and the bend direction). The sequences of marker coordinates are used to compute the sequence of the real-time deformation parameters. We will discuss the model and assumptions in detail in Chapter 4.

Finally, the SPECT projections, the specified deformation model, and the deformation parameters are used in a modified reconstruction algorithm to correct the misalignment caused by the body deformation during the reconstruction. We modify the mathematical reconstruction formula first by considering the deformation correction. The new algorithm can interact with the deformation data and combine the motion computation with the reconstruction. In the projection image, the regular counts are less than 10 usually. Therefore, during the reconstruction of the low counts number projections, we have to adopt Gaussian interpolation, instead of the traditional bilinear interpolation, to improve the resolution and to minimize the alias. The final results might not be as good as the result without deformation, but should be much better than the result with deformation but no correction.

1.2.2 Project Structure

Figure 1.7 depicts the block diagram for this project. Based on the goal we have, this project is composed of three major parts, *Deformation Model*, *Model Parameters Estimation*, and *Volume Reconstruction*. The deformation model will be described in Chapter 4. All the marker-related computation and volume related computation is described in the Chapter 5.

In the *Deformation Model* chapter, we will describe the deformation procedure, the parameters that we have to estimate and how to put the markers on the patient body. *Model Parameters Estimation* is composed of *Initial Body Pose Estimation* to specify the body pose using a set of patient body inherent variables, such as spine location and spine length, *Pattern Independent Deformation Estimation* to create the deformation parameter sequence (twist, bend and bend direction) as indicators of the deformation, *Camera to SPECT System Mapping* to associate the markers with the target volume, *Deformation Matrix* to show a mathematical deformation expression, and *Modified Volume Reconstruction*, to embed our deformation model-based motion correction module into the traditional reconstruction algorithm for the purpose of deformation correction. Given the initial body pose and the deformation parameter sequence, the modified reconstruction algorithm can generate a 3D motion-free volume. The deformation parameters and the projections should also be synchronized for reconstruction accuracy. The six sections are exactly the six steps in the deformation correction procedure. The reconstructed body volume is deformed by the deformation model and parameters to simulate the real deformation of the patient and counteract the motion effects.

The major contributions of the project are included in the following three modules, *Initial Body Pose Estimation*, *Pattern Independent Deformation Estimation*, *Deformation Matrix* and *Modified Iterative Reconstruction*.

1.2.3 Experiment and Simulation

Before we can use our method for motion correction, we have to verify our deformation model. We propose two experiments for verification purposes in this project (Figure 1.8). Firstly, we want to verify that our deformation model is reversible, which means the deformed volume can be reset to the initial pose with our deformation model and parameters. We call such a reset operation as "undeformation". The markers can be

considered as a set of special voxels in the volume, which also can be moved back from the deformed position to the initial position with an undeformation computation (Note: this is not an exact inverse computation). Such an undeformation computation for the markers can be used as one of the deformation model validation tools. Based on a set of markers based deformation data from real volunteers, we estimate all the deformation parameters. Then an undeformation computation is made for the deformed marker coordinates with our deformation model. Ideally, if our model is a perfect reversible model, the undeformed marker coordinates should be the same as the initial ones. Since the model directly affects the correctness of the deformation computation, our second step is to design an MRI based experiment to verify the correctness of our deformation model. A volunteer with retro-reflective markers is scanned twice by MRI, with and without deformation respectively. Two sets of body volumes from the same volunteer, with and without deformation are acquired. We estimate the deformation parameters and undeform the body volume with our deformation model. The purpose of this experiment is to test that our model is not restricted to the case of some special markers, but that is generalized to the whole torso. If our model is correct, the undeformed volume will be very close to the motionless volume.

Not only the model, but also the modified reconstruction algorithm should be checked before we use it for correction. Therefore, a simulation procedure is designed with the Mathematical Cardiac Torso (MCAT) phantom. The goal of the simulation is to theoretically validate the correction modified reconstruction algorithm. The simulation is composed of three steps. One is to reconstruct the 3D volume without deformation; the second is to reconstruct the 3D volume with predesigned deformation but no correction; the last one is to reconstruct the 3D volume with predesigned deformation and our correction. Finally, we have to combine the model with the modified reconstruction and validate the whole system with real patient data. We propose a verification procedure with SPECT, similar to the MCAT phantom simulation.

The clinic based experiment is finally applied to a real patient. In this experiment, the patient is required to undergo two SPECT acquisitions, one for motionless and another for some motion including both rigid and non-rigid motion. Traditional MLEM algorithm will be used to reconstruct the first acquisition for the motionless volume and the second acquisition for the motion volume without correction. RBM motion estimation and our modified reconstruction is used to reconstruct the second acquisition

for the motion volume with correction. Then, our deformation estimation module and our modified reconstruction is used to reconstruct the second acquisition for the motion volume with all kinds of motion correction. Finally, these four volumes are compared to draw our conclusions.

1.3 Road Map

The remainder of this dissertation is organized as follows: Chapter 2 provides background knowledge of the work in this proposal; Chapter 3 discusses related research in the areas of motion data acquisition; Chapter 4 investigates the issues with deformation modeling; Chapter 5 describes the proposed approach; Chapter 6 outlines the simulation and experiments for verification and Chapter 7 discusses the future work of this project.

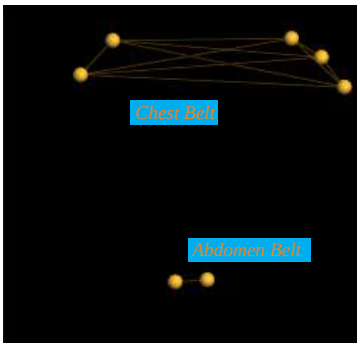

(a)

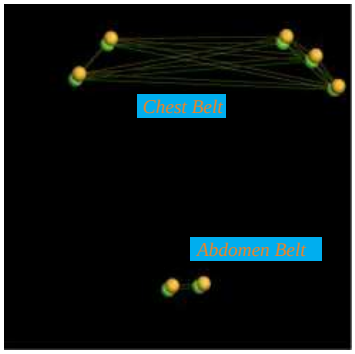

(b)

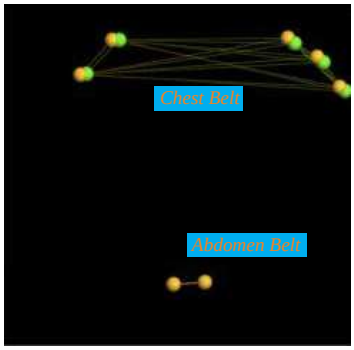

(c)

Figure 1.6: Shown as spheres are the coronal view locations of markers on the abdomen and chest belts of a patient during clinical cardiac SPECT imaging with motion tracking. (a) Initial marker positions; (b) Initial (yellow spheres) and post-deformation marker locations (green spheres); (c) Initial (yellow sphere) and post-deformation locations after RBM correction of abdominal sphere locations to match their initial positions (green spheres) as per the first step in the correction methodology proposed herein. Note residual marker motion is a combined CW twist when viewed from the direction of the patient's feet and bend to the left in 3D, and only the projection of this motion as viewed coronally is presented in this figure.

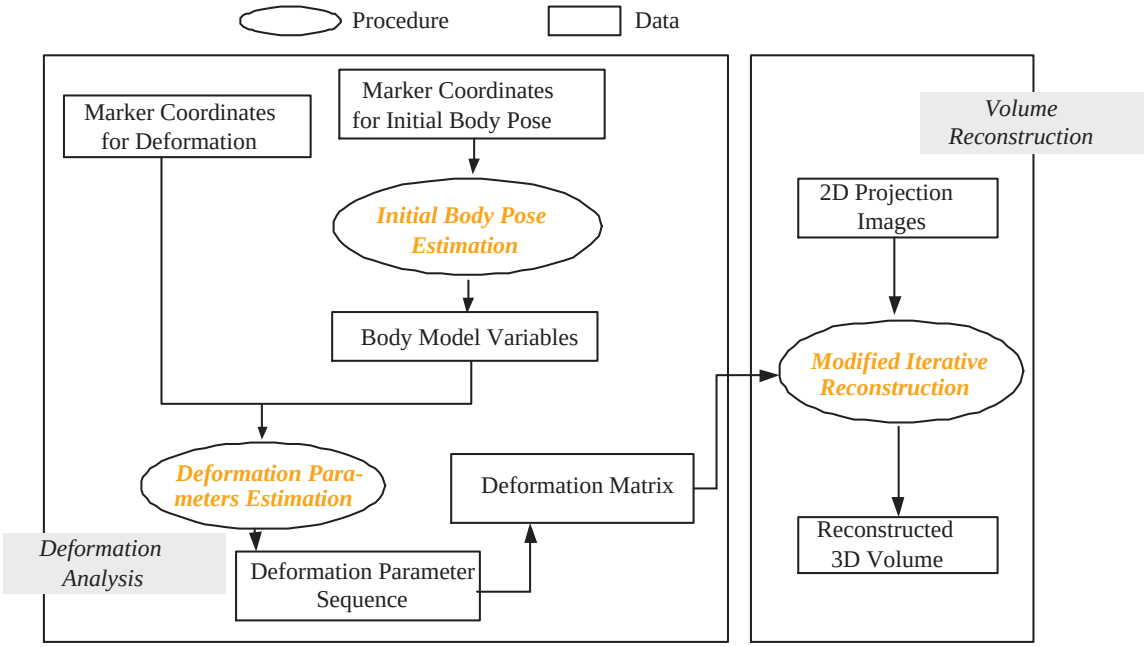

Figure 1.7: Block Diagram of the project. Notice: the orange module is the major contribution of this project.

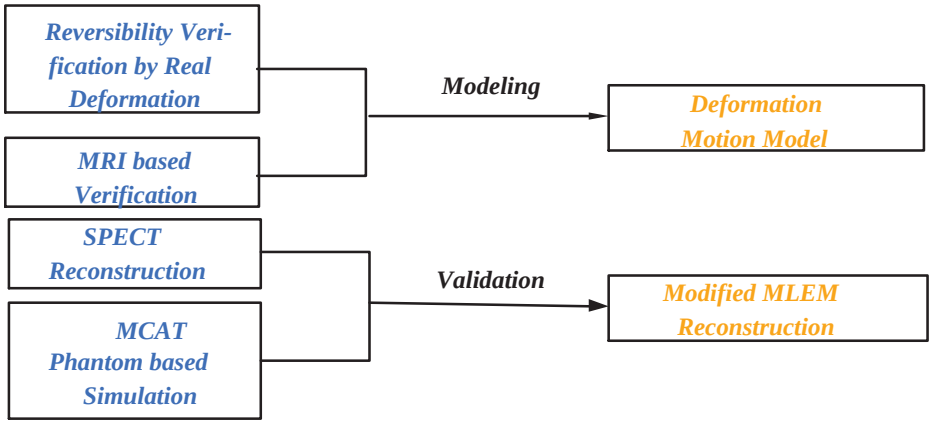

Figure 1.8: Deformation Model Verification and Systematic Verification.

Chapter 2

Background

2.1 SPECT Overview

SPECT is the primary modality for functional imaging in tumor detection or perfusion studies. A SPECT machine consists of gamma cameras, a patient table, a gantry, and an acquisition computer (Figure 2.1). The table can be translated to move the patient into the center of the gantry. By injecting a radiopharmaceutical, labeled with technetium-99m, iodine-123 and 131, gallium-67 or thallium-201 into the patient body, photons are emitted throughout the patient body. Though such radioactivity is attenuated by the body anatomy, it indicates the internal function of target organs. The gamma cameras, covered with collimators, detect the emission rays from the body. The electronics system can turn the photon events collected with the collimators into the intensity images, called projections. During imaging, the gamma cameras are rotating around the patient driven by the gantry. Currently, several companies, including *Siemens*, *GE*, *Toshiba* and *Philips*, are building SPECT imaging systems.

Because SPECT indicates functional information, it is effective in separating tumors from benign tissue (SNM, 2007). During emission of radioactivity, the body soft tissue attenuates the radiation and alters the projection images. SPECT is often used with an MRI or CT scanner to give a full three-dimensional view of an organ and the location of cancer within that structure. The newest scanners are a combination of SPECT and CT, so called SPECT-CT systems, which provide important metabolic information from SPECT superimposed on the high-quality anatomic information from CT. Such structural information provided from CT or MRI scans can also be used to

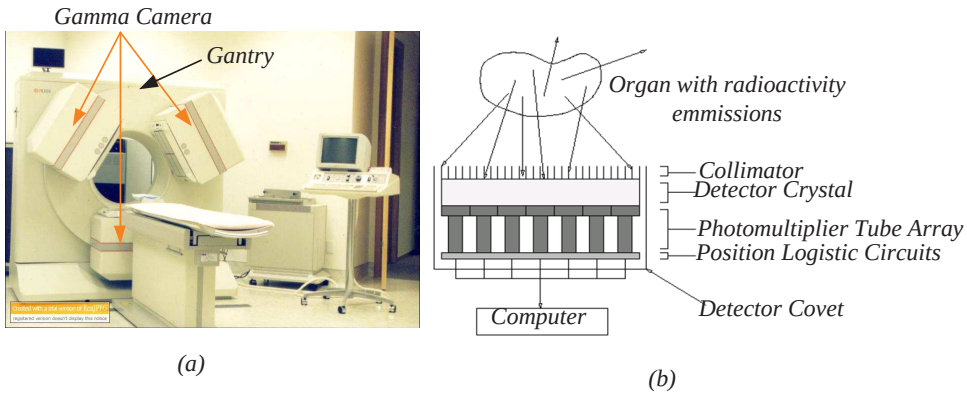

Figure 2.1: (a) SPECT Machine. (MedserVentures-Inc.,)(b) Mechanical Structure of a Gamma Camera in SPECT. (MIRG,)

create attenuation maps that will improve 3D reconstruction. Furthermore, with the anatomic information, it is easier to locate malignant tumors inside the body.

2.1.1 History of SPECT

To study the radioactive source distributions in the brain, crude spatial information were produced using a single detector positioned at various locations around the head as early as the 1940's. The rectilinear scanner was invented by Ben Classen to improve methods in the 1950's. This device produced planar images by mechanically moving a detector in a raster-like pattern over the area of interest. Current SPECT imaging equipment is also based on this technique. However, it requires 20 minutes of imaging time because of the sequential nature of the scanning, and the resolution is still quite low (Kuhl and Edwards, 1963).

Hal Anger developed a pin-hole based scanner in 1953. The image was projected onto a scintillating screen with photographic film behind it. This technique required extremely long exposure times because of the huge inefficiencies in the system (principally due to losses in the film). The inefficiencies in the system resulted in extremely high radiation doses to patients which caused side effects. To deal with this problem, Anger replaced the film and screen with a single NaI crystal and PMT array in the late 1950's. This formed the basis for the "Anger Camera" which is now the standard clinical nuclear imaging device. Modern Anger Cameras use a lead collimator perforated with many parallel, converging or diverging holes instead of the original pin-hole

configuration.

Kuhl and Edwards produced the first tomography from emission data in 1963. This was the beginning of the SPECT technology. Everett, Fleming, Todd and Nightengale suggested the use of the Compton effect for gamma-radiation imaging in 1977. This technique is currently in use in astronomy. Its adaptation to SPECT is non-trivial because of the vastly different source distributions and geometries involved. The investigation of the Compton Camera for SPECT began in 1983. Manbir Singh and David Doria proposed and experimented with a basic design using solid state detectors, performed an analysis of possible detector materials, and produced a small prototype for testing (James et al., 2004). At this time, the more conventional SPECT machine was already fully developed for clinical use.

Over the past several years, cardiac Positron Emission Tomography (PET), MRI, CT, and ultrasound have made significant advances while few new improvements in imaging hardware and radiopharmaceuticals have been realized for cardiac SPECT. Combining two or more imaging methods for diagnosis will significantly increase the accuracy. Based on this, SPECT-CT and SPECT-MRI equipment has been built for clinical use. Dynamic imaging can be performed for every cardiac SPECT procedure to provide improved lesion contrast and better evaluation of viable myocardium (G.T.Gullberg, 2004). Though the detection methods have been improved, the scanning time is still a big problem for SPECT. Some other problems related to long scanning time, such as patient motion blur, are popular research topics in the area of SPECT imaging.

2.2 Motion Capture

2.2.1 Motion Capture Introduction

Motion capture is a popular technique for generating human animation (Maiocchi,). Considerable literature exists on using and editing motion capture data in human animation. Motion capture yields an unstructured representation, which is a sequence of sampled marker trajectories (Bruderlin and Williams, 1995) (Witkin and Popovi'c, 1995). Such motion acquired from human beings can be analyzed for biomechanics (Zhou, 2001) or applied to animation in cartoons or video games.

The basic equipment for motion-capture consists of cameras around the perimeter of the tracking volume, a set of markers on the object, as well as hardware and software to process the data. Each camera captures synchronized images of the motion at a very high frame rate. All the cameras are synchronized so that it is easy to pair all the 2D coordinates from different cameras in one time slot. After we can identify a marker in 2 or more camera images at a given time, the 2D points pair can be triangulated into a 3D trajectory. Such a sequence of 3D coordinates is called "motion data". The triangulation algorithm is a sophisticated algorithm for 3D reconstruction from 2D images. Lots of work has been done using this method (Avidan and Shashua, 2000) (Bittar et al., 1995). Though the synchronized 2D coordinate pairs are acquired in real-time, the 3D reconstruction can be done off-line. Finally, we get the motion data of reflective markers as a sequence of 3D trajectories.

The motion capture system can be categorized into two types based on the approach used to identify different markers in different images from different cameras: systems with identifiable markers, and systems with uniform markers. Identifiable marker systems run with a set of distinguished markers. Such systems do not have the correspondence problem to identify each marker for different cameras. There are two ways to make the markers identifiable: powered and unpowered. It is helpful if we put some electrical power on each marker to make them shine. The powered markers are a set of LEDs that can flash in different time intervals or with different frequency. Thus each marker can be identified from different cameras. In this way, the environment can hardly disturb the marker identity. However, lots of applications forbid putting electrical wires on the human body, especially in medical applications. Therefore, the only choice for medical imaging is non-powered markers. If the markers are not powered, each marker has to be distinguished from other markers. Color is a simple choice (Brostow and Essa, 1999). It is convenient to acquire the correspondence information of the markers between different cameras. However, considering the background, it is quite difficult to specify each marker against the environment color. The lighting condition is another restriction for such a solution. Boutchko (Boutchko et al., 2007) also tried to identify markers with different shape, which requires complicated segmentation and registration techniques.

The motion capture system with uniform retro-reflective markers is another popular solution (Park et al., 2005) (Sundaresan and Chellappa, 2005) (McNamara et al., 2006)

(Bruyant et al., 2005a) (Bruyant et al., 2005b) without putting power on the target body. Passive and uniform markers give a lot of freedom to the motion capture system. Since there is no power, there are no wires and no extra equipment attached to the human body. Since the markers are uniform, theoretically, we can put as many as we want without considering identity conflicts. (Note: too close markers will cause ghost markers in the trajectory computation.)

For medical imaging purposes, the clinical environment is full of all kinds of color. Thus a system with uniform reflective markers is the only choice to capture the patient motion. The disadvantage of this type of motion capture is marker registration. Since each camera monitors the markers from different angles, the same marker appears in different positions for each camera image. To make it worse, when we back-project the 2D markers into 3D space for triangulation, ghost markers are created even if there is no real marker in that position because we are lack of accurate correspondence information for the 3D trajectory lines.

2.2.2 Calibration

Camera calibration is an important part of motion capture systems. Camera calibration is a method for calculating the camera parameters. Camera parameters include intrinsic parameters and extrinsic parameters. The intrinsic parameters are composed of the focal length, the principal point, the distortion parameters and skew. The extrinsic parameters are composed of the rotation and translation vectors, which indicate the camera pose. Currently, several major calibration techniques are available. The direct nonlinear minimization technique directly builds camera parameters to minimize the residual error by iterative computation (Abdel-Aziz and H.M.Karara, 1971). To avoid the iterative computation, phantom-based calibration is introduced. In this method, a set of 2D and 3D corresponding coordinates of the reference spheres are required. The intermediate parameters can be computed by solving linear equations and the final parameters are determined from intermediate parameters. However, lens distortions cannot be computed by this method (Ganapathy, 1984). Len (Len and Tsai, 1987) and Tsai (Tsai, 1986) (Tsai, 1987) introduced an improved solution for calibration which is a two-step method to compute the distortion and skew parameters. To improve the accuracy of one camera calibration based on the Tsai model, Zhang (Zhang, 1999) (Zhang,

2000) used a flexible method with Euclidean distance (Hartley and Zisserman, 2000), which only requires one camera and a set of grid board images. To make the calibration more convenient and avoid requiring 3D coordinates, Azarbayejani (Azarbayejani and Pentland, 1995) developed a one point multi-camera self-calibration method for at least three cameras. Svoboda (Svoboda et al., 2005) made this technique more robust.

2.2.3 Motion Capture Applications

Many motion capture systems are commercially available. VICON developed a motion capture system with retro-reflective markers. Animation and gait analysis were their first applications. A set of VICON cameras and related 3D reconstruction software, called "Nexus", were developed for the life sciences. There are other companies with similar products, such as *Phase Space Inc.* and *Motion-Analysis Inc.*

Other motion capture systems with powered active markers are also in use currently. *Moven* Inc. is building a motion capture system, in which the marker can send wireless signal to locate itself. The *Phase Space* company is also developing a system in which each marker can flash in a certain time interval to make itself distinguishable.

2.3 Motion Correction

The long scanning times for SPECT imaging causes some problems with the detection accuracy. The most important problem is the motion blur in the 3D reconstruction volumes. A SPECT system takes 2D projections one angle at a time. If the patient do not move, all the projections are from the same target. The reconstruction procedure can build a clear volume from these projection sets. However, a patient will inevitably have motion such as shifting, respiration or deformation, due to the long scanning time. That means some projections are coming from a moving torso, which will cause misalignment.

We can track this motion using a motion capture system as discussed before. The gross motion can be separated into 3 major components, RBM, RM and body deformation. Since it is a non-periodic motion, it consists of patient translation and patient rotation. At a given time, only one marker is required to calculate the rigid-body translation and at least three markers are required to calculate the rigid-body rotation

(a) *(b)* *(c)*

Figure 2.2: A sample from (Feng et al., 2005) for the RBM correction. (a) Reconstruction of the motion-free baseline acquisition. (b) The same trans-axial slice in the image summed for the 4 images acquired in 4 sequential acquisitions, without motion compensation in summing (Rigid Body Motion Only). (c) The same slice in the summed image with compensation for motion. No post-smoothing was applied to the images.

(Horn et al., 1988). If the translation vector and the rotation matrix are determined, Boening (Boening et al., 2004) provide a partial-reconstruction method to correct for RBM. This solution increases the resolution by reshaping the projection frames to correct the RBM. Also, Feng (Feng et al., 2005) published another method to estimate the patient rotation with generalized center-of-mass markers, which can be located with external cameras. To increase the resolution of the reconstruction, Feng (Feng et al., 2006) introduced a 3D Gaussian interpolation to substitute for the traditional bilinear interpolation. To improve this, Schumacher (Schumacher and Fischer, 2007) introduced a new approach to correct for abrupt rigid patient motion and the effects of gradual motion. Using RBM correction for SPECT has been well developed. However, none of the solutions model the relative motion between the markers, so that RBM correction methods cannot be extended to correct for non-rigid body deformation (Figure 2.2).

Respiration is another kind of body motion, with the property that it is periodic. During respiration, the patient body itself is deforming and the organs change their relative distances and orientation. Though we can measure the surface motion due to breathing, it is still difficult to deduce internal movement. Optical flow registration (Noumeir et al., 1996) (Cooper and Ritter, 2003) is used for brain motion correction. Gating (Livieratos et al., 2006) (Garbow et al., 2003) is a technique widely used for phase registration of the RM correction. With the gating information (the phase information of the periodic motion), Ablitt (Ablitt et al., 2004) tried to compensate for the RM by optical flow and partial least squares regression. However torso motion is larger

and more complicated than brain motion. Free-form registration, which introduces a set of control curves for the registration procedure, (Horn et al., 2003) (Rueckert et al., 1999) was introduced for torso RM correction. Based on a user-defined deformation path, free-form registration has more freedom to control the smoothness and the convergence time within the registration. Segmentation (Paik et al., 2004) (Armato et al., 1999) (Armato et al., 2001) has also been introduced for RM correction. Through segmenting the heart and lung out from other organs and gating the periodic motion, more precise correction could be achieved with the single organ volume reconstruction, such as cardiac or lung reconstruction. Combined with segmentation techniques, Dey (Dey et al., 2007) (Dey et al., 2006) introduced a more robust correction method for the RM related cardiac motion correction. Though a lot of progress has been made for RM correction, it is still not as well developed as RBM correction.

Based on the previous work described, RBM and RM can be corrected to some extent. On the other hand, there has still not been much work on deformation correction. Deformation correction for cardiac SPECT imaging is the focus of our project.

Chapter 3

Related Work

3.1 Motion Data Acquisition

Motion tracking and motion data acquisition is fully developed and widely used in varied applications. A modern motion tracking system is composed of high speed cameras, reflective markers, a high speed router and some other accessories (Figure 3.1). In our case, a VICON MX system, which is a flexible near infrared (NIR) multi-camera high-speed tracking system, was chosen. The VICON cameras can capture 242 frames per second with a resolution of 659×494. In this system, a set of reflective surface markers (Figure 3.3) are placed over the patient body (Figure 3.4). Several high speed cameras are positioned and calibrated in the SPECT clinic to track these reflective markers.

Two steps are required for the motion tracking acquisitions. Firstly, a multi-camera self-calibration method is adopted by VICON to calibrate all the cameras for the camera parameters (Figure 3.2). Currently, a multi-camera self-calibration method (Svoboda et al., 2005), which does the calibration by waving a wand of 3 markers is used. The accuracy of the calibration has great influence on the accuracy of the 3D coordinates. The data flow is shown in Figure 3.7. The calibration result is used for the computation of the trajectories of the retro-reflective markers. Secondly, the system records the coordinates of the markers during the motion capture procedure. For a 20 minutes' data acquisition, only several seconds is required to rebuild a 3D trajectory sequence of all the markers using a dual-core 2.0Ghz CPU. 3D trajectories of the reflective markers are called the motion data. Such motion data mixes all kinds of motion together. Before we can use it for motion correction, further processing is necessary to separate

(a) *(b)* *(c)*

Figure 3.1: Motion Capture System. (a)High Speed Camera. (b) Location of the cameras. (c) Reflective Markers.

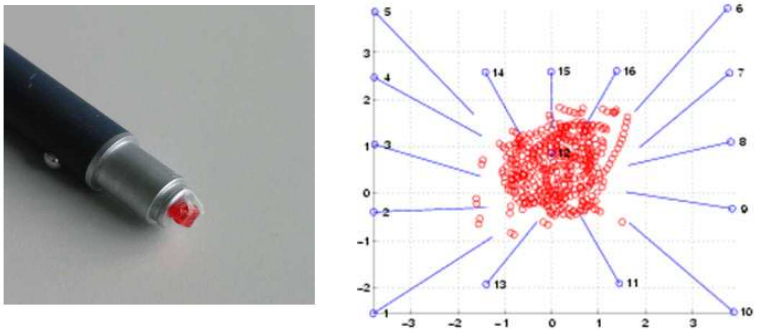

(a) *(b)*

Figure 3.2: Multi-Camera Self-Calibration (Svoboda et al., 2005). (a) A laser pointer with plastic tip. (b) Waving trace of the stick.

the various motions.

3.2 Motion Data Separation

Patient motion always includes RBM, RM as well as body deformation. How to separate them from the gross motion data is still an open question. For RBM, we assume that all markers move together as a whole rigid object. However, it is not true for the non-rigid body deformation and RM. These two motions change the relative distance between markers. The difference between them is that the RM is changing periodically and the body pose probably changes non-periodically.

Isaksson (Isaksson et al., 2005) introduced an adaptive approach based on a non-linear adaptive neural network to refine the RM. Beach (Beach et al., 2007) used this

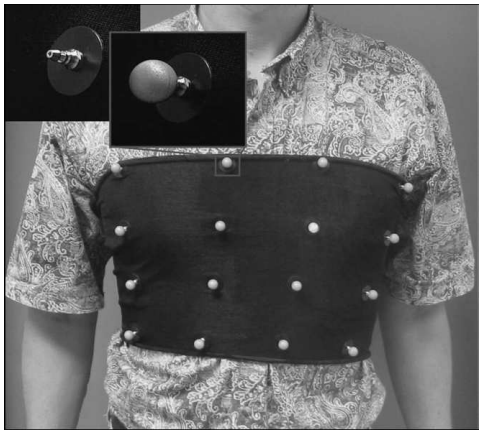

Figure 3.3: Sixteen highly retro-reflective spheres can be clipped on a garment made of black stretchable fabric. This garment is placed around the chest and the spheres 3-D motion is tracked by stereo techniques. Shown as inserts, are a mounting pin with and without sphere attached. (Bruyant et al., 2004)

technique to decompose the RBM and RM from gross motion. Though he did not consider non-rigid body deformation, he provided an efficient method based on a neural network technique to separate the RBM from the gross motion data. Based on the periodic difference between the RM and RBM, we can separate these two different motions by considering each marker oscillation individually (Mitra et al., 2007). Though the technique is not quite efficient in separating the deformation, we still can use it for an approximation.

Though total body motion is composed of three major components, these three motion components are not orthogonal. RM correction usually tracks individual markers only. RBM modeling can be approximated by considering at least three markers as one object and ignoring the inside relative deformation. Our body deformation model requires two belts on the patient body, one for the chest and one for the abdomen. We put 4-5 retro-reflective markers on each belt to help capture the patient surface motion. We consider each belt as one surface object and estimate the body deformation by the relative movement between the belts. In this research, we start with the RM extraction, followed by RBM extraction and consider the remaining motion as deformation. If we change the extraction order of the three components, the final result of the motion analysis may be different. It is very hard to tell which order is correct. We claim that our motion separation order works for our deformation correction purposes.

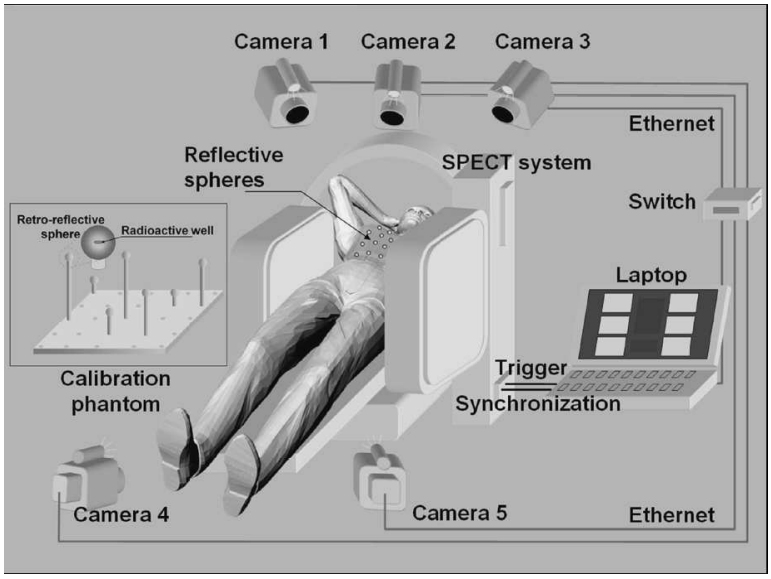

Figure 3.4: High Speed Cameras for Motion Tracking (Bruyant et al., 2004)

3.3 Synchronization

When we start the motion capture and SPECT acquisition, we have to synchronize the two systems so that we know the correspondence between the tracked motion and the projections. McNamara (McNamara et al., 2006) developed a synchronization method based on a square wave generated in the control box of VICON system. This square wave is sent with the trigger for SPECT and the motion capture system. Usually, the arrival times of the square wave to the motion capture system and the SPECT machine are almost the same. The time difference is less than 0.1 seconds and can be ignored. The SPECT machine will start working from this trigger after a short delay of 1-2 seconds. After the SPECT machine is started, the square wave is set to negative by the SPECT machine. The time interval between the start and the end of the square wave is recorded in the list most data as the synchronization information between the motion capture system and the SPECT machine. Based on the information provided by the square wave, we can adjust the start point of the records in the motion data to synchronize the start point of the SPECT machine. The square wave is sent once the SPECT gantry is ready for a new acquisition from a new angle. So the square wave triggers every projection acquisition to make sure the SPECT system and the motion capture system are synchronized well.

3.4 Reconstruction Algorithm

Reconstruction algorithms are used to reconstruct the 3D patient volume from the projections acquired by the SPECT imaging process. There are two major kinds of algorithms for SPECT reconstruction. The first one is a non-iterative method, such as FBP (Li et al., 1994). FBP is one of the earliest methods for reconstruction. This method is used not only for SPECT but also for CT (Xu and He, 2006). Though this method can reconstruct the 3D volume quickly, the quality of the reconstruction is not optimized. To improve the reconstruction, iterative algorithms are proposed. MLEM algorithm (Shepp and Vardi, 1982a) (Lange and Carson, 1984a) (Lalush and Tsui, 2000) (Krol et al., 2002) is a sophisticated method applied in emission tomography as an iterative technique for computing maximum likelihood estimates of the activity density parameters. Byrne (Byrne, 1998) accelerated the method using Poisson statistics. In this approach, the measured data are considered to be samples from a set of random variables whose probability density functions are related to the object distribution according to a mathematical model of the data acquisition process. Using this mathematical model, it is possible to calculate the probability that any initial distribution density in the object under study could have produced the observed data. In the set of all possible images, which represent a potential object distribution, the image having the highest probability is the maximum likelihood estimate of the original object. The mathematic expression of the MLEM is as follows:

$$f_j^{new} = \frac{f_j^{old}}{\sum_{i=1}^{n} a_{ij}} \sum_{i=1}^{n} \frac{g_i}{\sum_{j'=1}^{m} a_{ij'} f_{j'}^{old}} a_{ij} \tag{3.1}$$

Where the f_j is one voxel of the 3D reconstruction volume, a_{ij} is the projection matrix, and g_i is a 2D projection bin. Without motion, this iterative algorithm can reconstruct a 3D body volume from 2D projection images.

Ordered-Subset Expectation-Maximization (OSEM) algorithms (Hudson and Larkin, 1994) (Byrne, 1998) (Lalush and Tsui, 2000), which are related but much faster than MLEM, have quickly become the dominant iterative reconstruction procedures for SPECT in recent years. Marie(Marie et al., 2005) has proven that the OSEM algorithm works well for $^{201}T_l$ 16-interval gated SPECT. However, in our case, the patient motion is different for every projection. During the reconstruction, we have to study

each projection individually. Chen (Chen et al., 2007) changed MLEM by adding a motion term into the reconstruction formula and adjusting it for the RBM. If we want to treat the body as a deformable object and correct the deformation, we need to implement Chen's method with our special deformation terms and estimate the deformation matrix. Section 5.5 will show the details of such a modification.

3.5 Attenuation Correction

SPECT reconstructions are degraded by many physical factors, including attenuation, scatter and noise due to the random nature of the detection processes. This results in a loss of image quality and quantitative accuracy.

Part of the photons emitted from the patient body are absorbed by the patient body, such as in bone and soft tissue. That means the longer the photons travel through the body, the less likely they reach the collimator. That energy absorption creates some distortion in the 2D projection on the gamma cameras. If we omit attenuation correction, the final reconstruction volume will have some error.

The attenuation correction method is based on obtaining an attenuation coefficient map of the object through sequential transmission imaging. CT can be chosen for such transmission imaging since CT can differentiate between tissue types with varying attenuation coefficients. By segmenting different tissue types from the CT imaging, we can create an attenuation map to estimate the gamma ray loss in SPECT. A completely different approach was proposed by Natterer (Natterer, 1993), where the attenuation map is obtained without the additional acquisition of transmission images, which also avoids problems associated with the registration between different modalities. This method is based on the application of consistency conditions of the attenuated Radon transform to estimate the attenuation map from the emission projections. Researchers (Welch, 1997) (Krol, 2001) tested the method on simulated images of uniform and non-uniform attenuating regular geometrical objects in SPECT. The current trend is to measure and reconstruct the attenuation coefficient map using a transmission scan. The attenuation information is then incorporated into the reconstruction algorithm of the emission data by modifying the projector and the back-projector pair. This approach increases the SPECT acquisition time and requires special hardware (Noumeir and El-Daccache, 1998).

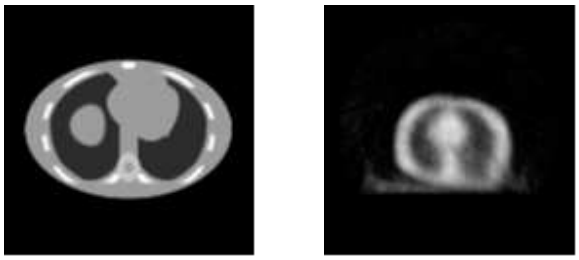

(a) *(b)*

Figure 3.5: Sample Slices from attenuation maps. (a) A slice from the MCAT phantom attenuation map. (b) A slice from real attenuation in clinic, acquired by transmission imaging.

Though all the approaches have their own advantages and problems, they provide us with a valid attenuation map for reconstruction. Furthermore, if some other methods to acquire the attenuation map are available, they can substitute for the previous ones in our application conveniently. Figure 3.5 shows some sample slices from attenuation map.

3.6 Scatter Correction

Scatter correction is another important correction during reconstruction. Quantification with SPECT images is degraded by photon scattering. When a beam of gamma ray interacts with atoms in a material, two scattering processes occur, Rayleigh scatter and Compton scatter. Rayleigh scatter will change the direction of a gamma ray, but will not change the energy level. Compton scatter will change the direction as well as the energy, depending on the scatter angle.

To correct the scatter effect, we have to estimate the magnitude of the scatter effect inside the body with a scatter map. A general idea for the magnitude of scatter in myocardial imaging is an estimate of the ratio of scattered to unscattered (primary) counts. Ogawa (Bruyant et al., 2002) introduced a triple energy window (TEW) method to estimate the scatter map. In this method, the scatter rejection windows (Figure 3.6) and the energy main window for the photon acceptance overlap each other. Then the scatter map can be estimated by the subwindow on both sides of the main window. Fujioka (Fujioka et al., 1997) applied the method for scatter correction in conventional

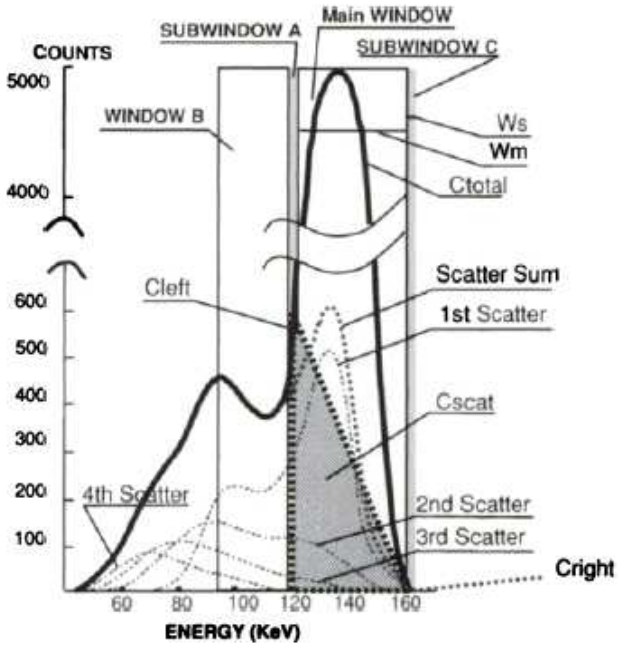

Figure 3.6: Position-dependent Scatter compensation method (TEW) and a simulated energy spectrum of using MonteCarlo modeling. This figure shows the total energy spectrum, the first to the fourth order scattering (1st Scatter, 4th Scatter), and the sum of all orders of scattering (Scatter Sum). Most of the scattered photons in the main window are first order scattered photons. To reduce scattered photons accurately, it is necessary to estimate the scatter sum. In the main window,which is shown as a shaded the angle using the counts in narrow scatter rejection windows A and C, adjacent to the main window. (Ichihara et al., 1993)

SPECT systems without any hardware for TEW acquisition. To avoid the issue of negative vales when the TEW estimate is subtracted from the acquired data, one can follow the methodology of (McNamara et al., 2007) and add the scatter estimate to the estimated scatter-free projection data in the denominator on the right-hand side of Eq 3.1. The advantage of this method is that TEW scatter correction does not require extra hardware and can be done to the projections before the reconstruction computation.

Effective scatter source estimation (ESSE)(Frey and Tsui, 1997) (Clough, 1986) (Frey and Tsui, 1993) is another scatter map estimation method developed for non-homogeneous scatter objects based on transmission maps (Welch et al., 1995). In this method, the scatter map can be estimated from the transmission map, which is a 3D

volume reconstructed from the transmission projections with an outside radioactive source. This method works well for anisotropic objects. Since the human body is an anisotropic object, we adopt this ESSE scatter estimation method in this project.

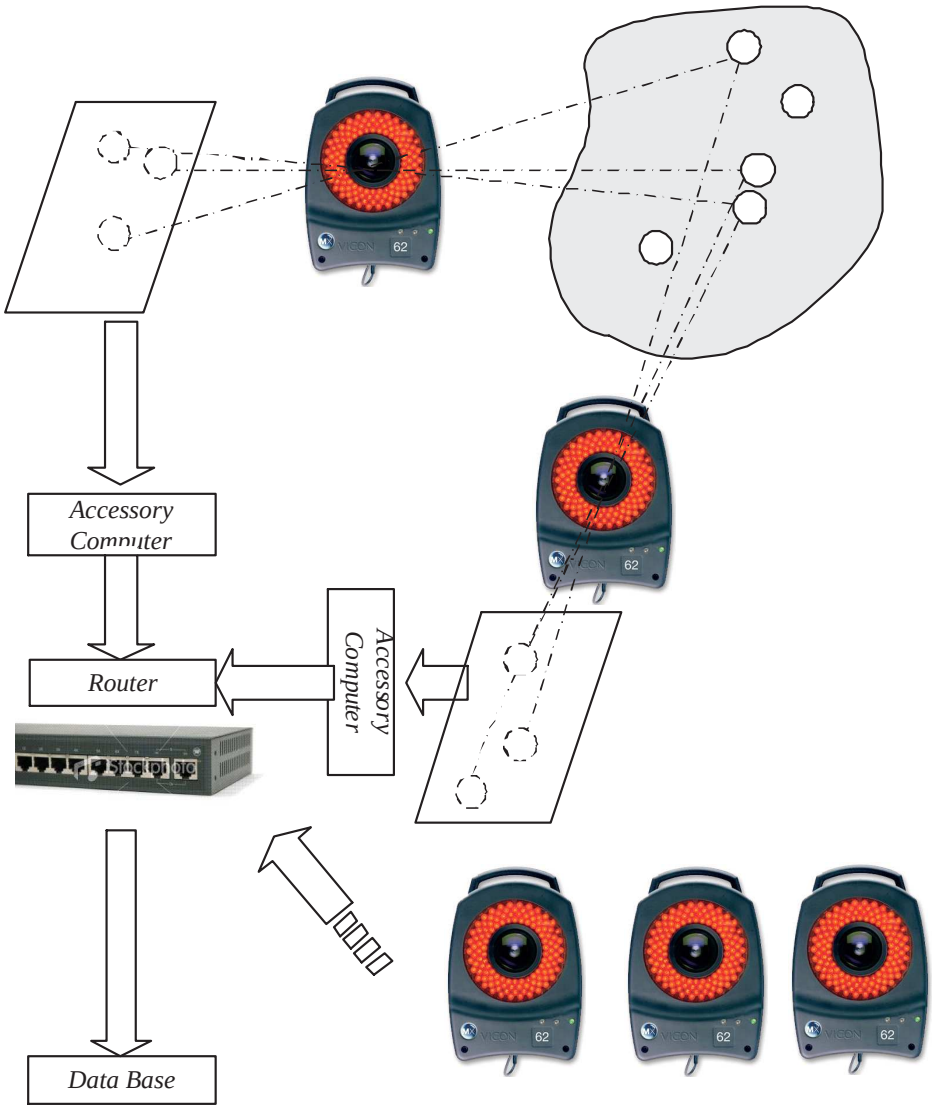

Figure 3.7: Data Flow of Motion Capture System

Chapter 4

Deformation Model

4.1 Previous Body Deformation Model

Body deformation simulation is an important topic not only in medical imaging but also in robotics. Lee (Lee and Arjunan, 1991) introduced a 3 DOF rotation computation model to model each joint of a robot. Chablat (Chablat and Wenger, 2005) built a robotic vertebrae with a set of 3 DOF joints, called roll, pitch and yaw angles, corresponding to the bending, bending direction and twist angle in this dissertation. Since a real human joint shares the same physical features with a robotic joint, we assume that we also can use the 3 DOF motion system to simulate a real human joint, particularly for the joints between vertebrae.

Another important factor on body deformation is the deformation distribution along the spine. Vorro (Vorro and Johnston, 2003) designed a method to detect the twist distribution of a human body. As shown in Figure 4.1, a volunteer who has attached a set of sensors in the muscles along the back is required to make only twist motion. Then the sensor measures the twist deformation of each muscle. Since the twist deformation of the muscle is caused by or leads to a corresponding twist in the joint between vertebrae, we can conclude how much contribution each vertebra made during the twist. Though there were only 9 subjects studied for these experiments, a rough distribution of the vertebra for the twist is drawn. However, such results are only for twist, not bend. Schwartz (Rozumalski et al., 2007) designed another experiment to detect the motion distribution of human lumbar vertebrae. To make the result more precise, Schwartz arranged a set of pins, each attached to a reflective marker (Figure 4.2), and stuck them

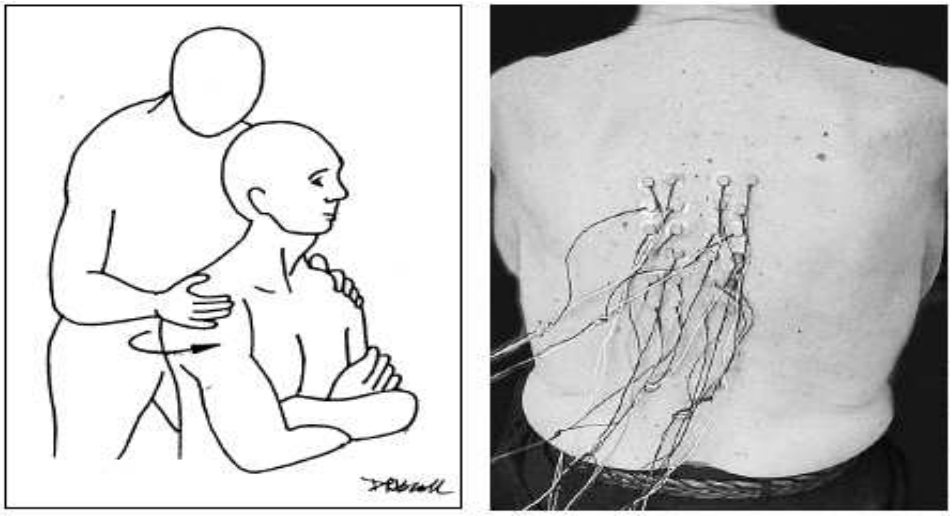

(a) *(b)*

Figure 4.1: Experiment for twist motion distribution study. (a) Passive regional shoulder rotation to the left in the seated position. (b) Electrode placement at thoracic levels 4 through 9. (Vorro and Johnston, 2003)

into each vertebra of the spine. The volunteers were required to make some bending deformations and two calibrated cameras recorded such deformation. Finally, the 3D coordinates of the reflective markers and the tops of the pins were computed to reveal the distribution of the bending among the joints in the spine. In his research, 10 sets of data from 10 different volunteers were used.

All the previous work has made contributions to our body deformation modeling. The joints of the human body are simulated by a 3 DOF hinge system in biomechanics research. Moreover, some methods to detect the distribution of body motion are being developed. However, such work is far from complete. These two experimental studies for spine modeling clearly provided a starting point, but both lack significant amounts of data. To deal with this general problem, we wish to more robustly model the spine with 3 DOF.

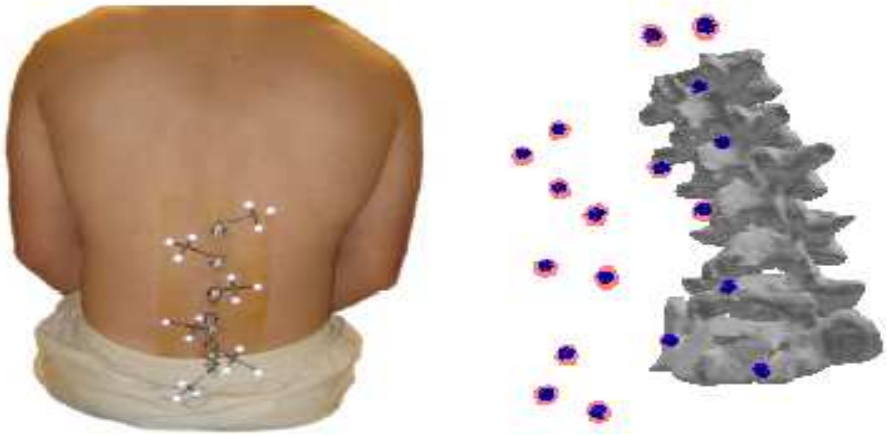

(a) *(b)*

Figure 4.2: Experiment for bending motion distribution study. (a) Experimental setup showing rigid triads mounted to Kirshner wires; (b) Subject-specific vertebral meshes (grey) and defining markers (blue) are shown. The faint red point clouds around the markers are CT-based marker meshes used to confirm proper registration (Rozumalski et al., 2007).

4.2 Vertebra Deformation

The body deformation of internal organs is driven by the motion of the skeletal system. Therefore, for our body deformation study, we are primarily concerned with body skeleton deformation. The body skeleton in the thoracic region is composed of the spine and ribs. To make the problem simpler, we only consider the spine motion and consider the ribs as extensions of the spine and always perpendicular to the spine. In the human body, the spine is composed of 33 vertebra. When some deformation happens on the body, the total deformation could be decomposed into unit deformations, each caused by a single joint between pairs of the vertebras. Since we know the mechanical structure of joints, we can study the degree of the deformation by a single joint and extend it to the whole spine.

Each joint of vertebras can be considered as the basic unit for our body deformation. The connection between the vertebras is quite similar to a hinge. For a regular 3D system, an object has 6 DOF to move, 3 degrees for translation and 3 degrees for rotation. In a hinge system, translation between the two parts is forbidden. Most hinge systems are modeled using only 3 DOF (Lee and Arjunan, 1991) (Chablat and

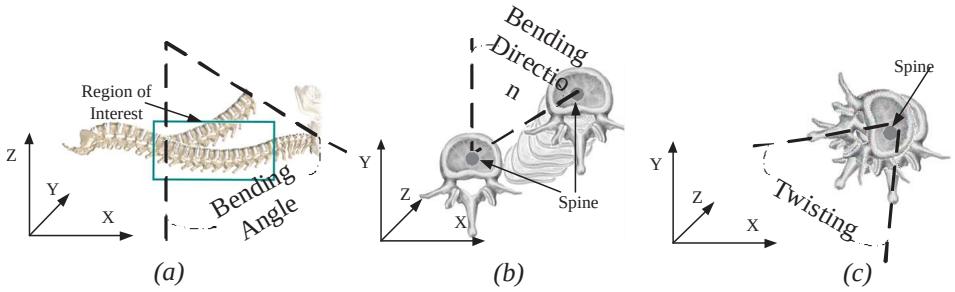

Figure 4.3: Three Degrees of Freedom. (a) Bending Angle; (b) Bending Direction; (c) Twist Angle.

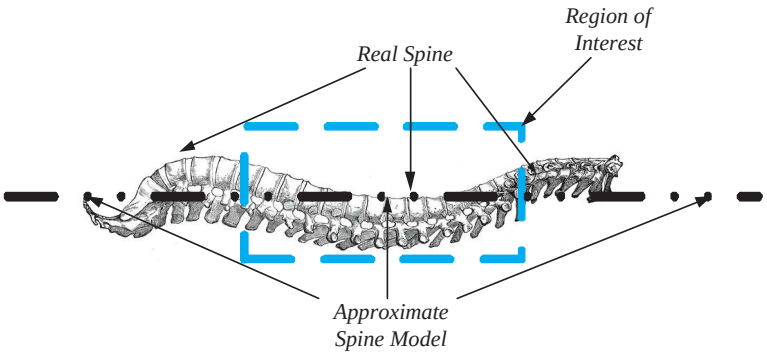

Figure 4.4: Approximate Spine Model.

Wenger, 2005), which is how we will represent the segments of the vertebrae. In our research, a hinge system with 3 DOF, called twist angle, bend angle and bend direction (Figure 4.3), is used to simulate the motion of the spine.

4.3 Spine Deformation

To measure the spine deformation distribution, we have to create a spine model that can be parameterized by the surface markers. We define body deformations as occurring solely within a region of interest (ROI) (Figure 4.4) consisting of a portion of the spine imaged by our SPECT system as defined by the placement of our motion-tracking markers. Usually, the ROI includes the body parts between vertebrae $C7$ to $T7$. A natural spine is more like a curve (Yang et al., 2007) than a straight line. However, when the patient is lying supine on an imaging table, the spine curve between the vertebrae

$C7$ to $T7$ is reduced compared to other postures. Figure 4.6 shows some examples MRI images of volunteer spines illustrating this. These spine shapes are close to a straight line in the ROI except due to the support provided for the patients head, shoulders and arms. Therefore, we approximate the spine as a straight line for computational simplicity (Figure 4.4).

It is too hard to measure the body deformation directly from the patient body. However, body deformation leads to surface deformation. On the other hand, we can measure the total body deformation parameters by the skin-based markers with geometric computations. Then we need to determine the contribution of each vertebra to the surface deformation so that we can estimate the deformation of each part inside the torso. The deformation of all the vertebras has a certain inherent distribution. Even if we know the total twist and bend angle, we still do not know the distribution along the spine. For example, suppose the twist angle is 1 unit, the first vertebra unit may contain 50% and the second one may only contribute 10%. We use an angle distribution map to define the contribution ratio of the spine deformation. The deformation map can be expressed as follows:

$$[B_i, T_i] = Distribution(B, D, T, i) \tag{4.1}$$

where i is the index for the current vertebra unit; B_i is the bending angle of i-th unit, T_i is the twist angle of i-th unit; $Distribution()$ is the approximate function that can be used to simulate the physical characteristic of the patient body. B is the total bend angle; D is the total bend direction and T is the total twist angle of the whole body. Since previous work has not provided a solid deformation model (Vorro and Johnston, 2003) (Rozumalski et al., 2007), a simple distribution model is proposed in our project. We assume that the bend distribution and the twist angle distribution of the spine both comply with a uniform distribution. That means all the bend and twist motion is equally shared by all the joints and each unit of the vertebra takes the same contribution for the total angle (Figure 4.5). The most significant advantage of this method is that it is easy to calculate. We do not need to define the $Distribution()$ function. However, if there is a better deformation distribution description in the future, our model can be adapted easily.

During torso bend, some parts of the body are compressed and other parts are

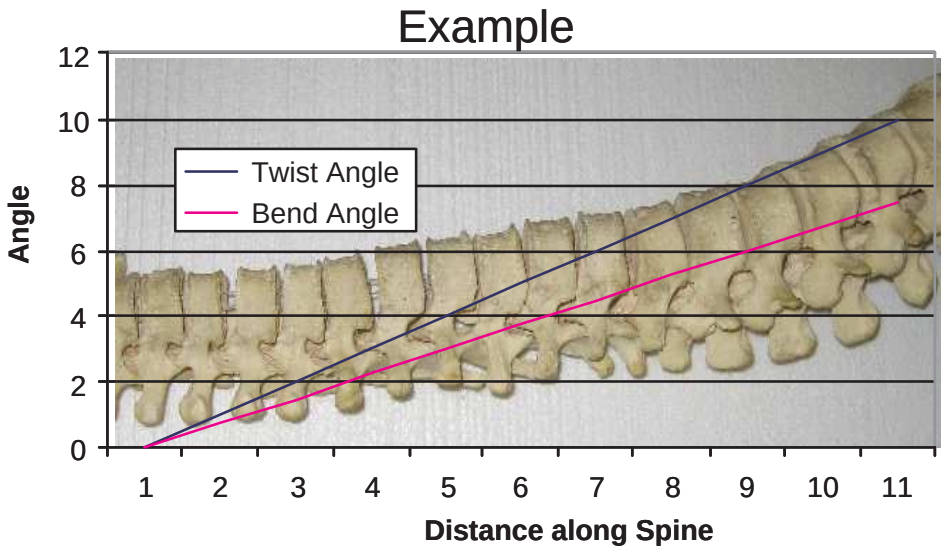

Figure 4.5: An example of the spine deformation with uniform distribution.

stretched. There must be a baseline that keeps the same length during the body bend. With the baseline, we can describe the body bend mathematically. Therefore, we make a second assumption that the length of the spine is not changed during the body bend. The spine is considered as the axis of the body twist. Since we assume the spine is a straight line along the z-axis, we can use the coordinates in the xy-plane to define the spine position. The spine location and the spine length are considered as the inherent parameters determined by the patient. These two inherent parameters will not change during the motion. The spine location we mentioned in this paper is the spine location in the start point of the ROI, beyond which all the deformation is ignored. During the whole deformation, the spine location in the start point of the ROI will not change.

Another important assumption for spine deformation is that when a spine is bending, the spine remains co-planer and incompressible. That means for all joints in the spine, the bend direction, D in Eq. 4.1, keeps the same value. And the spine length will not change during the deformation. All the assumptions are reasonable approximations for the medical imaging purposes, where patients are usually in a comfortable spine position. This assumption makes it easy for us to build a geometric description of the deformation. Though not an accurate assumption, it is a good starting point for our research. Now we can compute the bend direction directly from the markers

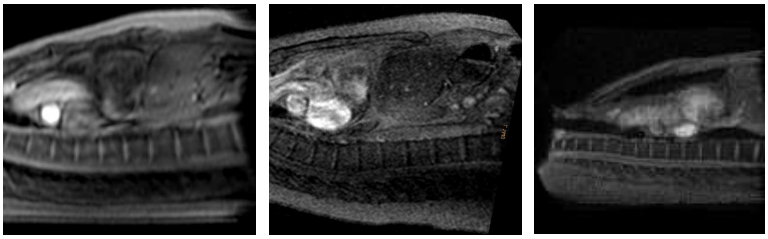

Figure 4.6: Spine images from MRI scans when patients are lying down supine.

attached to the patient.

With all these assumptions, we have the following simple estimation for the local twist and bend for voxel v:

$$T_v = T\frac{L_v}{L_s} \tag{4.2}$$

$$B_v = B\frac{L_v}{L_s} \tag{4.3}$$

where T_v and B_v are the local twist and bend angle for the v-th vertebra; L_s is the spine length in the ROI; L_v is the distance between the local voxel and the z-axis value of the abdomen belt, which is considered as the start point of the deformation.

4.4 Body Modeling

We define deformations as occurring solely within a region of interest (ROI) consisting of a portion of the spine imaged by our SPECT system as defined by the placement of our motion-tracking markers. The deformation happening outside of the ROI is considered as RBM. Usually, the ROI includes the upper thoracic vertebrae. When the patient is lying on a flat imaging table, the spine curve in this region is reduced compared to other postures. Figure 4.6 shows three example MRI images of the spines of volunteers illustrating this. These spine shapes are approximately a straight line in the ROI except due to the support provided for the patient's head, shoulders, and arms, which are raised to be out of the way during SPECT imaging. Therefore, we approximate the spine as a straight line.

Our simple deformation model utilizes 3 parameters: twist angle (T), bend angle

(B), and bend direction (D). The twist angle is defined as a rotation of the spine, with the rotation increasing from the pelvis to the head. The bend angle is defined as the extent of curving of the spine (apart from its usual curved shape) along an arc. The bend direction is defined as the angular direction for which the bend occurs with respect to the mid-sagittal plane. In Figures 4.7 and 4.8 we show the effects of twist and bend separately on a patient voxel. We take a voxel v_0 (Figures 4.7a and 4.8a) as the initial position. Figure 4.7b shows that the initial voxel v_0 would be moved to v_1 by twist. Bend can be decomposed into three steps: 1) rotate the body to make the bend upwards in the mid-sagittal plane; 2) make the body bend in this sagittal plane; and 3) then rotate the body back into the initial position. This process is illustrated in Figure 4.8. We rotate voxel v_1 to v_2 (Figure 4.8b). Bend is applied which moves the voxel from v_2 to v_3 (Figure 4.8c). Finally, we restore the desired bend direction by rotating voxel v_3 to the final deformed position v_4 (Figure 4.8d). Combining the bend direction and the bend angle, we can model bend motion in any direction (for example, laterally), and not just in the sagittal plane. The order in which the twist and bend operations are performed is arbitrary, but must be consistent throughout the model, as twist and bend do not commute. We have chosen the convention that twist precedes bend.

We acknowledge that this model is a gross simplification of what actually happens to the spine as patients move. The deformation is not necessarily uniform at each joint. Given more information about the spine mechanics one could model the probable fractional change at each vertebra. For example, Vorro (Vorro and Johnston, 2003) evaluated myoelectric data obtained from spinal motion dynamics involved in clinical rotation tests. A functional model is discussed for this myoelectric activity involving a helical spinal motor pattern with a focal area of transition that is dynamic in response to postural and motion demands. To understand human lumbar spine motion, Schwartz (Rozumalski et al., 2007) performed an in-vivo experiment to develop a method for visualizing the in-vivo motion of the entire human lumbar spine region, which is mostly composed of bend motion. However, these studies were made when the patient was sitting. In our case, the patient is lying supine during the SPECT imaging. The relationship between the vertebrae most likely depends on the patient pose. Therefore, in this research, we make a simple assumption that the distributions of bend and twist along the spine are both uniform. This means that all the deformations are equally

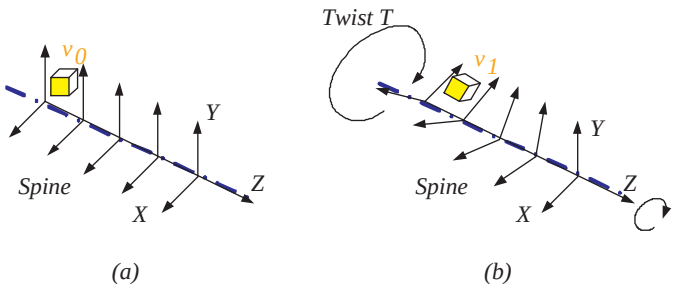

Figure 4.7: Model of twist. (a) Initial position; (b) Illustration of progressive body twist about spine which by our convention increases from abdomen to chest.

shared by all the joints with each unit of the spine contributing equally toward the total angle. This assumption is an over-simplification, which can be improved upon with refined models in the future.

Other important assumptions for the spine deformation are 1) the spine is incompressible, and 2) when the spine is bent, it continues to lie within a single plane. Though not perfectly accurate assumptions, they are good starting points for this research. With these assumptions, we can compute the bend angle and direction directly from the markers attached to the patient.

Based on all the assumptions mentioned above, we build an approximate deformation model of the general patient body. If we can quantify the three parameters, T, B, and D, we can map the initial patient body into the deformed one. Such a map also can be expressed as a motion matrix M, so that $\vec{f}_{deform} = M\vec{f}_{init}$ ($\vec{f}_{init}$ and $\vec{f}_{deform}$ are the motionless and deformed body).

This mapping between the motionless torso and the deformed torso can be described as a deformation matrix M. For a voxel v, the deformation matrix determines where it is after the deformation. So we have Eq. 4.4

$$M^v = M^v(T_i, B_i, D; L_s, L_v) \tag{4.4}$$

where M^v is the deformation matrix for voxel v; T_v is the local twist angle of the current voxel defined by Eq. 4.2; B_v is the local bend angle defined by Eq. 4.3; D is the bend direction; L_s is the spine location in xy-plane and L_v is the spine length from the voxel v to the abdomen belt alone z-axis. Then the deformation matrix for the total torso will be

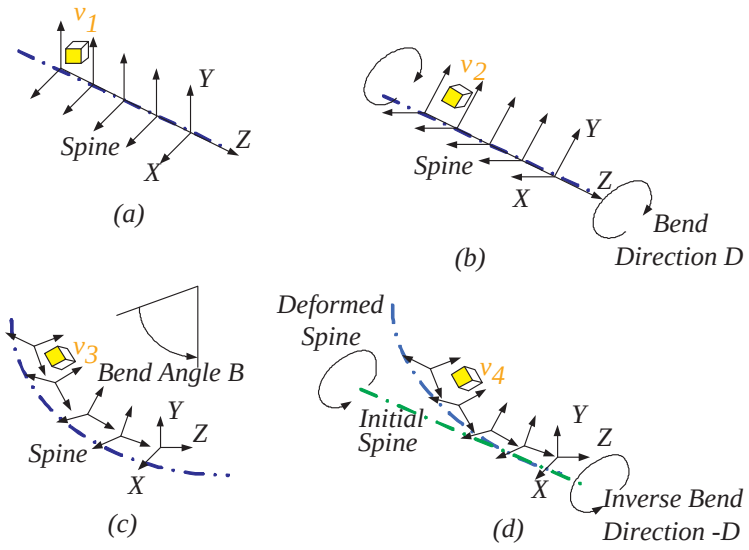

Figure 4.8: Model of Bend. (a) Initial position; (b) Rotation around spine by an amount equal to the bend direction so that we can apply bend in the sagittal planes; (c) Bend by the bend angle is performed; (d) Rotate back the slice data to its original orientation around the spine by application of the inverse of the bend direction.

$$M = \left[\; M^0 | M^1 \ldots | M^v | \ldots | M^{N-1} \; \right] \tag{4.5}$$

where N is the number of voxels.

4.5 Marker Deployment

Based on our strategy for motion detection, we have to put a set of markers on the patient surface to detect patient motion. Such detection can be done with a VICON motion capture system, which uses retro-reflective markers as indicators. In the clinic application, we have two realistic problems: 1) how to avoid the overlap and mismatching during the 3D trajectory computation; 2) how to use the marker position information to represent the body deformation.

Theoretically, we can put many markers on the patient body. However, we have learned that if we put too many markers on the body, we have a big matching problem, which is an NP-complete problem in computational geometry. When the VICON

system calculates the 3D trajectory from each 2D marker's snapshot, the 2D marker emits a 3D trajectory line into the 3D space. The VICON matching algorithm considers the closest line from other 2D marker's image as the correct matching and picks the crossing point as the position in 3D. If there are too many trajectory lines in the 3D space, mismatching will inevitably occur. Such mismatching will build some ghost markers, which do not exist, and will miss some real markers. To avoid this problem to some extent, we designed a marker deployment strategy.

In this research, we put two sticky plastic belts around the patient body. One belt is around the chest area and another belt is around the abdomen area. The area between these two belts is the body part where most of the deformation occurs. Based on our experience, the max number of markers in each belt should not be more than 5. Otherwise, there will be too many ghost markers created by the trajectory algorithm of the VICON motion capture system. Mathematically, one marker is the minimum requirement to detect the patient's rigid body shifts and 3 markers (not co-linear) are the minimum requirements to detect the rigid body rotation. Due to the deviation caused by the RM correction, we prefer some redundancy. However, in the body deformation estimation, we estimate the chest belt and abdomen belt motion separately. That means at least 3 markers for each belt are required for the deformation motion detection. Furthermore, most of the deformation computation will be based on the chest belt motion. Therefore, in this project, we use 5 markers on the chest belt and at least 3 markers on the abdomen belt.

The pattern of the markers on the belt determines the visibility of the markers during the motion capture procedure, which is crucial to the final motion estimation. The simplest pattern is the straight line. However, if we put the chest markers in a straight line, we probably will create some ill-conditional matrices during the motion estimation. Another requirement for the marker pattern is that the markers should not block each other. Patient bodies are different in terms of the shape, height, and gender. Due to the uncertainty of torso shapes, there is no one general pattern fit for all patients. Figure 4.9 shows some sample patterns that could be used for motion capture. Therefore, in this project, our deformation estimation module should work for all kinds of marker patterns that should be decided by clinic technicians.

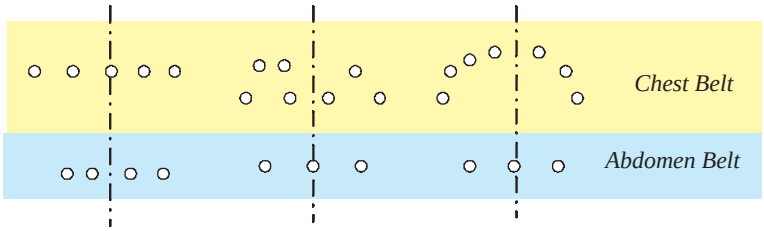

Figure 4.9: Sample marker patterns.

Chapter 5

MATERIALS AND METHODS

5.1 Initial Body Pose Estimation

Since we have described a deformation model, the motion data is used to specify the deformation parameters for our model. In our model, the patient spine length and spine location in xy-plane are two inherent parameters that will not change during the deformation. In the initial body pose estimation, we have to specify these two parameters: the spine location in xy-plane and the spline length along z-axis. These two parameters will be used for the reconstruction as well as for validation.

For motion-tracking, two belts are wrapped about the patient body; one is about the chest and the other about the abdomen, as shown in Figure 5.1. After we capture the markers' motion, we can assign some internal position of marker coordinates as our motionless pose. That means we consider these coordinate records as reference records. Usually, the reference records are selected from the first several second after the volunteer lies supine. Each reference record includes the coordinates of the chest markers and the abdomen markers.

In one set of the reference coordinates, we can compute a centroid of the chest markers and a centroid of the abdomen markers. Since the SPECT scan usually focus on the area between the belts, in this research, we consider the distance along the z-axis between these two centroids as the spine length. The torso within the these two centroids (along z-axis) is the ROI of our deformation corrections. The deformation of the torso outside of this region is either omitted or only considered as RBM.

Before the SPECT acquisition, we have to estimate the spine location in the xy-

plane. Accurately locating the spine is important for two reasons: it provides the center axis for twist (Figure 4.7) and the reference line for bend (Figure 4.8). If available we can use the CT slices of a SPECT/CT system to give precise localization. Based on MRI studies (see Figure 4.6) typically this height will be estimated as 1/3 the distance to the average anterior level of the chest belt from the surface of the imaging table. Since we do not have dual-modality for this study, in this paper we take this MRI observation based estimation as the approximate level of the spine. By this way, we can locate the spine in the xy-plane. We take the x coordinates of the chest marker centroid as the x coordinate of the spine location. Since such an estimation is not robust, the spine location estimation will cause some measurement error in the model. We evaluate the error caused by the spine location estimation in our simulation and experiments.

5.2 Pattern Independent Deformation Estimation

We have pointed out that there is no marker pattern applicable to all patients. Because of this variability in the pattern of markers on the belts, we developed a method of estimating our three parameters (twist T, bend B and bend direction D) for body deformation, which is independent of the marker pattern.

The chest and abdomen belts have a Velcro layer affixed to them which does not stretch, but does bend. Therefore, the marker patterns on these belts do not change much during the deformation. We take the abdomen belt as the baseline for computation in that any motion in that belt after the respiratory motion has been removed (Mukherjee et al., 2009) is taken to be rigid-body deformation. Using rigid-body correction, we return the abdomen belt to its initial pose. Then, patient deformation is indicated entirely by the chest belt. Therefore, in the remainder of this paper, we treat the respiratory and rigid-body motions as having been modeled, and henceforth consider the remaining input motion data to comprise only deformation.

In our model, each of the belts has an associated plane that goes through the centroid of the belt markers and intersects the patient spine (Figure 5.1). We call these planes as the chest key plane for the chest belt and the abdomen key plane for the abdomen belt. The chest key plane P_c and the abdomen key plane P_a are determined as the planes perpendicular to the spine that intersect the average axial location of the

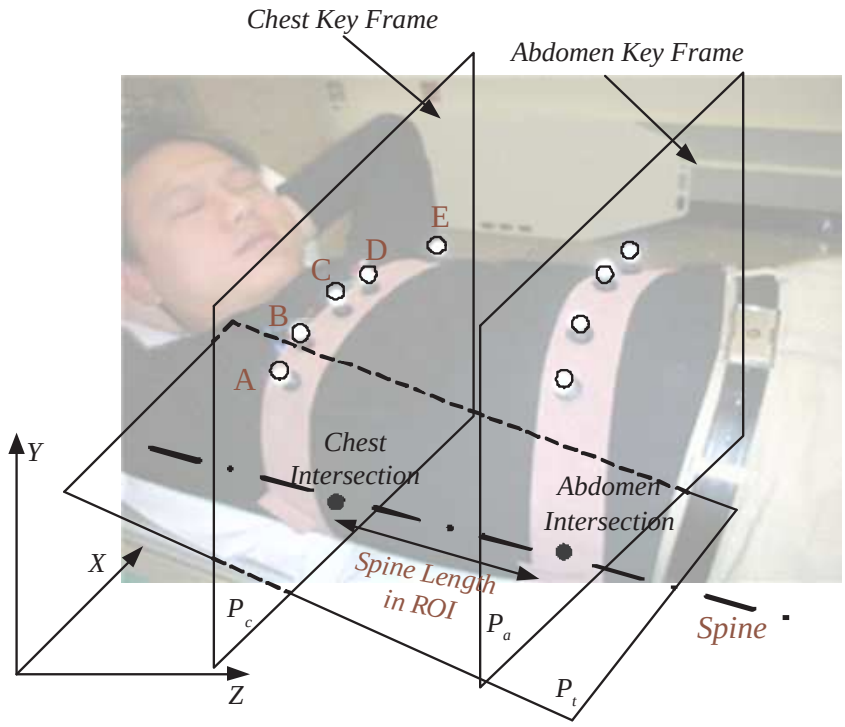

Figure 5.1: Body with belts showing chest markers $A - E$, table plane P_t, chest key plane P_c, abdomen key plane P_a, chest and abdomen intersections with the spine. Shown also is the coordinate system employed in this manuscript with X being the lateral axis, Y the vertical axis, and Z the axial axis.

markers on a given belt. We use these key planes as the start and end of the ROI for deformation measurement. By computing the distance between the two key planes, we estimate the length of a section of spine within the ROI.

We need a patient reference pose for motion correction; all motion computations are carried out with respect to this pose. We pick the initial patient position as the reference, justified by the observation that the ability of patients to remain still decreases over time. The reference pose is determined by the first set of chest marker coordinates $S = \{S_i\}$, where S_i is the i-th marker coordinates. After patient motion, the markers have another set of coordinates S'. Following RM and RBM correction based on the abdominal markers, the chest markers have a third set of coordinates S", providing the information needed to determine body deformation.

The affine transformation between S and S", which determines the deformation

parameters, is given by

$$S" = sR_{motion}S + \tau_{motion} \tag{5.1}$$

where s is a scale factor, R_{motion} is a rotation matrix, and τ_{motion} is a translation vector. Since we will not move the position of the cameras during the motion acquisition, the scale factor can be considered as 1.

To solve this equation, we have to consider two factors. The marker pattern could be symmetrical, which give some freedom for the technician to design the marker pattern. Another factor pertains to the marker trajectory. Since our motion capture system captures the motion at 30 fps. It is a reasonable hypothesis that the patient can not move more than 1 cm during 1/30 second. That means during the whole motion capture process, we can follow each marker and the marker correspondence information is always recorded by the motion capture system. Since we know the 3D coordinates and correspondence of S and $S"$, the rotation matrix R_{motion} can be computed as

$$R_{motion} = (S" - \bar{S"})(S - \bar{S})^{+} \tag{5.2}$$

where + is the pseudo-inverse operation; S and $S"$ are the coordinate sets of all the markers before and after RM and RBM correction, $\bar{S}$ is the average marker coordinate before the patient motion; and $\bar{S"}$ is the average marker coordinate after the RM and RBM correction. We account for the translation τ by aligning the markers' centroid of initial and deformed configurations. As long as the markers are not co-linear, matrix R_{motion} is a full rank matrix. With this method, the matrix R_{motion} is not guaranteed to be perfectly orthonormal due to the little belts deforming during the motion. We have to apply a SVD transformation to R_{motion} for normalization.

$$R_{motion} = U\sigma V^T \tag{5.3}$$

where U and V^T are orthonormal matrix; σ is a diagonal matrix. If R is a orthonormal matrix, σ should be an identity matrix. In our case, we expect σ to be very close to an identity matrix. Therefore, R can be adjusted to a closest orthonormal matrix UV^T.

In general, matrix R_{motion} can be uniquely decomposed into the three components as

$$R_{motion} = R_{D^{-1}} R_B R_D R_T \tag{5.4}$$

where $R_D = \begin{bmatrix} cos(D) & sin(-D) & 0 \\ sin(D) & cos(D) & 0 \\ 0 & 0 & 1 \end{bmatrix}$, $R_B = \begin{bmatrix} cos(B) & 0 & sin(B) \\ 0 & 1 & 0 \\ sin(-B) & 0 & cos(B) \end{bmatrix}$ and $R_T = \begin{bmatrix} cos(T) & sin(-T) & 0 \\ sin(T) & cos(T) & 0 \\ 0 & 0 & 1 \end{bmatrix}$, $R_{D^{-1}} = \begin{bmatrix} cos(D) & sin(D) & 0 \\ sin(-D) & cos(D) & 0 \\ 0 & 0 & 1 \end{bmatrix}$. Note $R_{D^{-1}}$ is equal to R_{-D} where D is replaced by$-D$. Since the twist and bend direction share the same rotation axis, we can simplify Eq. 5.4 to

$$R_{motion} = R_{-D} R_B R_{D+T} \tag{5.5}$$

where $R_D R_T = R_{D+T} = \begin{bmatrix} cos(D+T) & -sin(D+T) & 0 \\ sin(D+T) & cos(D+T) & 0 \\ 0 & 0 & 1 \end{bmatrix}$.

From the elements of R_{motion} we can thus determine the deformation model parameters. The bend angle B can be found from element R_{22} which is $cos(B)$; knowing B, the bend direction D can be found from $R_{02} = -sin(B)cos(D)$ or $R_{12} = sin(B)sin(D)$; knowing B and D, the twist angle T can be found from element $R_{20} = sin(B)cos(D+T)$ or $R_{21} = -sin(B)sin(D+T)$. Note when $B = 0$, D is not uniquely defined. In this case, we take $D = 0$ and find T in the usual way. By this way, we can estimate the total twist angle T, the total bend angle B and the bend direction D.

Since our chest belt is quite rigid and can not be warped easily, the motion modeled in Eq. 5.6 is almost an affine transformation between the initial chest markers and the deformed chest belt. Eq. 5.4 also illustrates the procedure that we use to model the deformation. We rotate the patient body with the bend direction to make the bend occur upward, bend the patient body with the bending angle, rotate the body back to counteract the first rotation and then make a twist movement with the twist angle. In this way our model can deal with the bend in a random direction and not just in the sagittal plane. Deformation throughout the volume of the ROI is modeled as the incremental decrease in B and T (Eq. 4.2 and Eq. 4.3) to zero as one proceeds axially from the chest side of the ROI to that of the abdominal side as illustrated in Figure

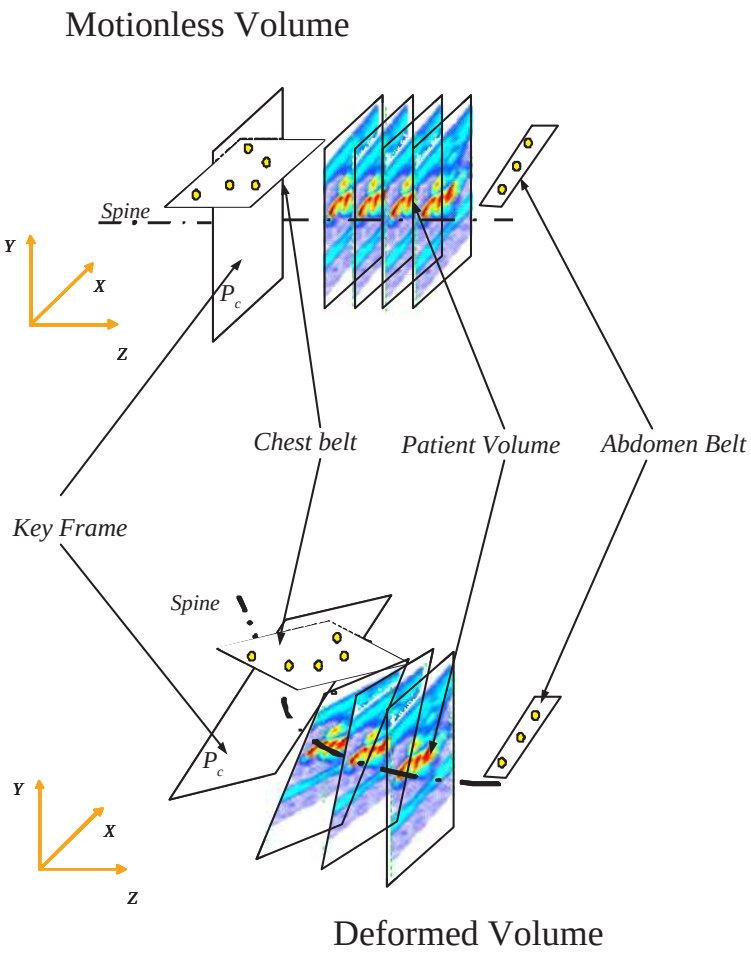

Figure 5.2: Chest key plane and chest belt.

5.2. We check the validity of our model with some experiments in Section 6.3.

5.3 Camera to SPECT System Mapping

To describe the relationship between the chest markers and the body volume, we define a key plane, which is a plane passing through the belt perpendicular to the patient's spine (Figure 5.1). The belts and their markers define the chest key plane P_c and the abdomen key plane P_a. The volume between these two planes is defined as the ROI. There are lots of way to define a plane by point sets. In this research, we just let the plane go though the centroid of the belt markers. With this definition, the rotation of the chest key plane P_c is determined by the rotation of the chest belt, which is caused by the body deformation. If we can map the key plane from the marker coordinate system to the SPECT coordinate system (Figure 5.2), the motion estimated from the markers can be used to estimate the body motion.

In this research, we use a 7-sphere phantom to build the affine transformation (Figure 5.3). The spheres are retro-reflective so that they can be captured by the motion capture system. The phantom also contains radioactivity for imaging with the SPECT camera. Comparison of the 3D coordinates of the blobs obtained from the camera system and from the SPECT reconstruction establishes an affine transformation between the two coordinate systems. We consider the coordinates of the marker's physical cetroids as the marker's coordinates. Given the marker coordinates X in the motion capture system and the marker coordinates X' in the SPECT system, we have

$$X'_i = sR_{trans}X_i + \tau_{trans} \tag{5.6}$$

where $X = \{X_i | iisthemarkernumber.\}$, $X' = \{X'_i | iisthemarkernumber.\}$, s is a scale factor, R_{trans} is a rotation matrix, and τ_{trans} is a translation vector. We have introduced a method to calculate the affine transformation in Section 5.1. We know the correspondence information in that case. However, in this case, we do not know the one to one correspondence of the markers between the SPECT system and the motion capture system. The searching space for the correspondence is $n!$, where n is the number of spheres. When we try to increase the number, the computation time for the searching will be large. In this procedure, we have two sets of coordinates, one from the motion capture system and another from the SPECT system. Physically, these two point sets X and X' are the same, so the residual error is expected to be close to zero. To solve this problem, we do not have to know the correspondence. Since

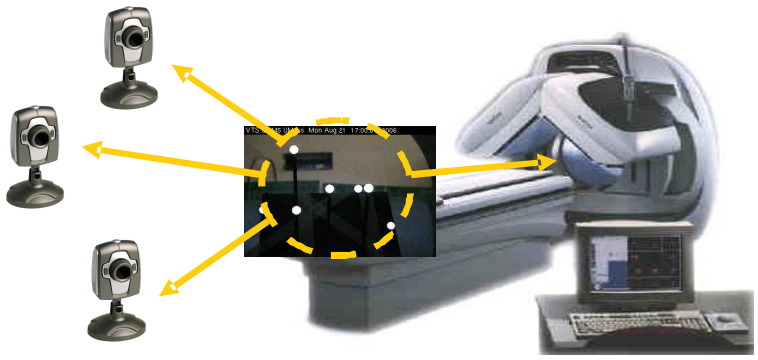

Figure 5.3: Affine transformation between the motion capture system and SPECT.

the phantom stays still during this data acquisition, given 3D coordinates of X and X', we can compute the rotation matrix R_{trans} (Horn et al., 1988) as

$$R_{trans} = (A(A^T A)^{-1/2}) \tag{5.7}$$

where $A = \sum_{i=0}^{n} ((X_i - \bar{X})(X_i' - \bar{X}'))$ with n is the marker number; and X and X' are the coordinates of the blobs from two coordinate systems, $\bar{X}$ and $\bar{X}'$ are the average marker coordinates from two coordinate systems. As long as the markers are not co-linear, matrix A is a full rank matrix and matrix R_{trans} is orthonormal.

5.4 Deformation Matrix

The spine location provides the central axis for the twist and the spine length provides the computational baseline for the bend. By computing the distance between the two intersection points, we can estimate the length of a section of spine within what we will take as our ROI. All the deformation should happen inside the ROI. The motion happening outside the ROI will be considered as RBM.

Combined with the simple spine model, the three parameters B, D, and T along with the level of the spine specify the deformation at each voxel of the body volume. Using Equations 4.4 and 4.5, we can map the initial body volume to the deformed body volume with the deformation matrix M. Since M may change as a function of time during acquisition, we use $M(t)$ for the deformation expression. Applying the deformation matrix $M(t)$ for the initial volume, we have

$$\vec{f_{deform}}(t) = M(t)\vec{f_{init}} \tag{5.8}$$

$$\vec{g} = \begin{bmatrix} \vec{g_0} \\ \vec{g_1} \\ \dots \\ \vec{g_{l-1}} \end{bmatrix} = \begin{bmatrix} A_0 & 0 & \dots & 0 \\ 0 & A_1 & \dots & 0 \\ \dots & \dots & \dots & \dots \\ 0 & 0 & \dots & A_l \end{bmatrix} \begin{bmatrix} M_0 \\ M_1 \\ \dots \\ M_{l-1} \end{bmatrix} \vec{f_{init}} \tag{5.9}$$

where $\vec{f_{init}}$ and $\vec{f_{deform}}$ are the motionless and deformed reconstruction volumes, respectively; $\vec{g_i}$ is the sub-matrix of the i-th angle of the projection's vector ; A_i is the sub-matrix of the system matrix A related to $\vec{g_i}$ and include imaging geometry, attenuation, scatter, and distance-dependent spatial resolution and $M_i = \int_{t=T_i}^{T_{i+1}} M(t)dt$. T_i is the start time of i-th projection and $M(t)$ is the deformation matrix at time t.

The deformation matrix is a mapping connecting the initial body with the deformed body for each of the series of intervals for which projections were acquired. Note that with list-mode acquisition motion correction can be made at a finer temporal resolution then the duration of acquisition of a projection. Currently, in this research, we still use the frame mode based reconstruction for its simplicity. To simplify the problem, we determine the $M(t)$ based on a set of mean parameters calculated with the marker coordinates during acquiring the current projection. The motion data rate is acquired at 30 frames per angle. On the other hand, the projection rate was around 20 seconds per image. Based on our synchronization, we can determine the motion data belonging to a certain projection time, in which a single projection image is detected. The motion data would be put into both the RM and RBM estimation modules and the deformation estimation module. There are 6 DOF in the RBM estimation module: 3 for translation and 3 for rotation. For the translation, we chose the mean values of the translation vector as the translation vector of the target projection. For the rotation, we had to extract the 3 rotation angles around the 3 axes from the rotation matrix first. The rotation order could be arbitrarily decided. However, this order had to be compatible with the following rotation matrix computation. The mean values of the 3 rotation angles were used to rebuild a rotation matrix based on the mean angles. Similarly, we could take the mean value of the deformation parameters (B, D and T) belonging to a certain projection as the mean deformation parameter. After

the synchronization computation, each projection image has a single set of parameters for RBM and deformation motion. Since the patient has different motions for different projections, we had to choose the MLEM algorithm for the reconstruction.

Based on the estimated motion parameters, we have an explicit motion matrix $M(t)$, which shall be represented simply as M_i in following. M_i includes the RBM, deformation, and interpolation necessary to implement the motion. For projection angles when the patient has not moved or deformed, M_i is the identity matrix.

5.5 Modified MLEM Reconstruction

There are lots of algorithms for SPECT reconstruction. However, in this project, we have to correct the patient deformation within each projection individually. The OSEM and RBI algorithms back-project several projections simultaneously. That will increase the deformation correction cost. Therefore, we choose the MLEM algorithm as our basic reconstruction method.

MLEM is an ideal reconstruction method (Shepp and Vardi, 1982a) (Lange and Carson, 1984a) (Byrne, 1998) (Lalush and Tsui, 2000) to be modified for motion correction purpose. The following is a modified MLEM algorithm based on the algorithm description by Bruyant (Bruyant, 2002). Shepp (Shepp and Vardi, 1982b) and Lange (Lange and Carson, 1984b) have introduced a basic way to derive the MLEM reconstruction method. In these works, the numbers of both the emitted and the detected counts are assumed to be Poisson random variables.

Let us consider f_j, the mean number of counts from pixel j, and the element a_{ij} of the matrix A, the probability that bin i detects a photon emitted from pixel j. The mean number of photons emitted from pixel j and detected by bin i (g_i) is the sum of the mean number of photons emitted from each pixel:

$$g_i = \sum_{j=1}^{l} a_{ij} f_j \tag{5.10}$$

It can be shown that the number of photons emitted from the l voxels and detected by bin i is a Poisson variable. If the patient has some deformation, deformation matrix

M_i should be factored into the projection. Eq. 5.10 can be rewritten as:

$$g_i = \sum_{j=1}^{l} \sum_{k=1}^{l} a_{ik} m_{kj} f_j \tag{5.11}$$

where m_{ij} are the elements of the deformation matrix M_i. Thus, the probability of detecting g_i with deformation is given by:

$$P(g_i) = \frac{e^{-g_i} g_i^{g_i}}{g_i!} \tag{5.12}$$

The i Poisson variables are independent, and the conditional probability $P(g|f)$ of observing the vector g when the emission map is f is the product of the individual probabilities $P(g_i)$. The likelihood function $L(f)$ is given by:

$$L(f) = P(g|f) = \coprod_{i=1}^{n} \frac{e^{-g_i} g_i^{g_i}}{g_i!} \tag{5.13}$$

The highest value for the likelihood $L(f)$ is found by computing its derivative. To maximize the expectation, one usually considers $l(f) = ln(L(f))$, where ln denotes the natural logarithm. Eq. 5.13 becomes:

$$l(f) = \sum_{i=1}^{n} -g_i + g_i ln(g_i) - ln(g_i!) \tag{5.14}$$

and using Eq. 5.10 to introduce f_j, we obtain:

$$l(f) = -\sum_{i=1}^{n} \sum_{j=1}^{l} a_{ij} f_j + g_i ln(\sum_{j=1}^{l} a_{ij} f_j) - ln(g_i!) \tag{5.15}$$

This equation, called the likelihood function, is one of fundamental importance in the MLEM algorithm, because it allows one to calculate the probability to observe a projection dataset for any mean image f. Then, we use the deformation projection

equation Eq. 5.11 to introduce f_j, we obtain:

$$l(f) = -\sum_{i=1}^{n}\sum_{j=1}^{l}\sum_{k=1}^{n} a_{ik}m_{kj}f_j + g_i ln(\sum_{j=1}^{l}\sum_{k=1}^{l} a_{ik}m_{kj}f_j) - ln(g_i!) \tag{5.16}$$

We want the image that has the highest probability to yield g, so the essential point here is that the vector f for which $l(f)$ is maximal is considered as the best estimate for the solution. The maximum is found when the derivative of $l(f)$ is zero.

$$\frac{\delta l(f)}{\delta f_j} = -\sum_{i=1}^{n}\sum_{k=1}^{l} a_{ik}m_{kj} + \sum_{i=1}^{n}\sum_{k=1}^{l} a_{ik}m_{kj}\frac{g_i}{\sum_{j'=1}^{l}\sum_{k'=1}^{l} a_{ik'}(m_{k'j'}f_{j'})} = 0 \tag{5.17}$$

One can also write:

$$f_j\frac{\delta l(f)}{\delta f_j} = -f_j\sum_{i=1}^{n}\sum_{k=1}^{l} a_{ik}m_{kj} + f_j\sum_{i=1}^{n}\sum_{k=1}^{l} a_{ik}m_{kj}\frac{g_i}{\sum_{j'=1}^{l}\sum_{k'=1}^{l} a_{ik'}(m_{k'j'}f_{j'})} = 0 \tag{5.18}$$

However, when we apply this reconstruction method for our purpose, we have to take the physical computation order into account. Deformation matrix M_i describes the deformation at each voxel of the body volume.

$$f_j^{new} = \frac{f_j^{old}}{\sum_{i=1}^{n} a_{ki}\sum_{k=1}^{l} m_{jk}} \cdot \sum_{i=1}^{n} a_{ki}\sum_{k=1}^{l} m_{jk}\frac{g_i}{\sum_{j'=1}^{l}\sum_{k'=1}^{l} a_{ik'}(m_{k'j'}f_{j'})} \tag{5.19}$$

where the a_{ij} is the projection matrix and m_{kj} is the motion estimation. More precision in the motion estimation matrix M_i leads to more precision in the motion corrected data. In our non-rigid deformation correction, the motion term m_{kj} is defined by the three degrees of freedom. In the algorithm implementation, the deformation operation is always followed by the back-projection. Therefore, we swap the order of M_i and A in the formula to match the computation order.

$$f_j^{new} = \frac{f_j^{old}}{\sum_{k=1}^{l} m_{jk}^T\sum_{i=1}^{n} a_{ki}^T} \cdot \sum_{k=1}^{l} m_{jk}^T\sum_{i=1}^{n} a_{ki}^T\frac{g_i}{\sum_{j'=1}^{l}\sum_{k'=1}^{l} a_{ik'}(m_{k'j'}f_{j'})} \tag{5.20}$$

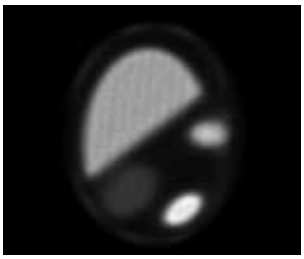

(a) Reconstruction Result with Bilinear Interpolation

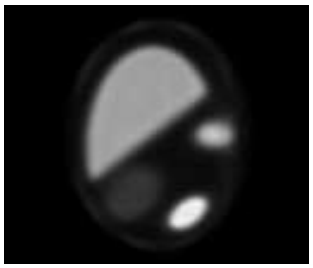

(b) Reconstruction with Gaussian Interpolation.

Figure 5.4: Comparison of different interpolation method.

During the reconstruction, we warp the body volume to simulate the real body deformation and get a better 3D reconstruction result. The spine plane works as an indicator, which is incompressible, so that we can apply the bending angle, bending direction and twisting angle into the 3D volume. Figure 5.6 is the procedure for reconstruction with deformation correction. More precise deformation estimation of the matrix M_i leads to more precise reconstruction of the body volume.

Interpolation is an important computation during such 3D deformation. Bilinear interpolation is the most popular interpolation method for its simplicity. The spectrum shape of the bilinear interpolation kernel is a triangle. It can not deal with the alias as well as the Gaussian interpolation kernel. To make it worse, if we consider the rotation, the alias problem will be worse if we choose the bilinear interpolation kernel. Gaussian interpolation is another interpolation method, which uses a Gaussian function as the interpolation kernel. It can reduce the alias caused by both the sampling and the rotation. Feng (Feng et al., 2006) extended the 2D Gaussian interpolation into 3D. Figure 5.4 shows the comparison of two interpolation methods. Gaussian interpolation produces a visibly better result.

An important concept in the modified MLEM update equation is back-deformation, which plays a role similar to back-projection. In traditional MLEM, the operation $\sum_i a_{ji}^T g_i$ is the back-projection of projection data g_i along the system matrix into the reconstruction volume, arising as an alternative to inverting system matrix A directly, which is at best an ill-posed problem. Analogously, in our modified MLEM algorithm, the operation $\sum_k m_{jk} \sum_i a_{ki}^T g_i$ is the back-deformation of deformed volume $\sum_i a_{ji}^T g_i$

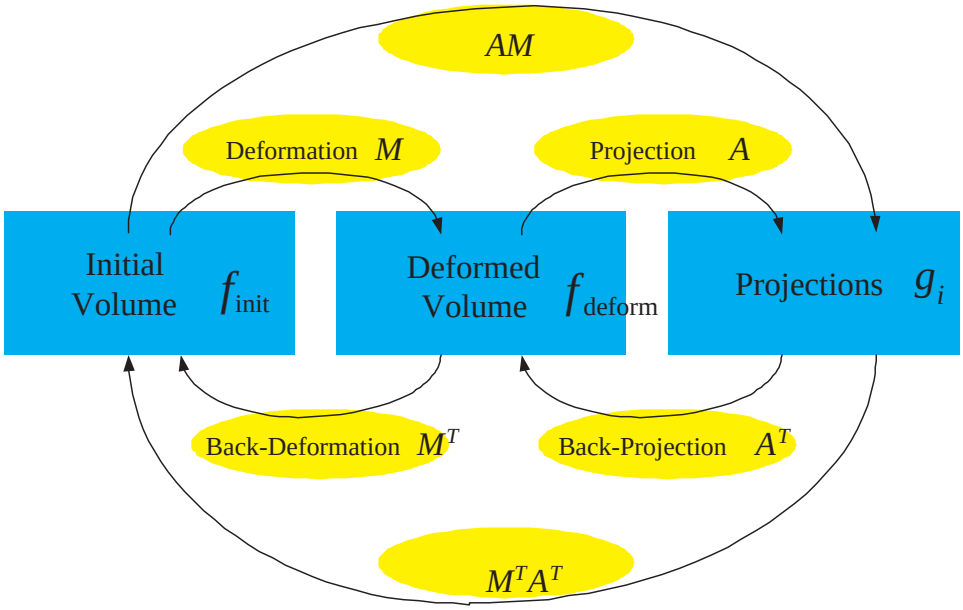

Figure 5.5: Relationship between the initial volume, deformed volume and the projections.

along the deformation matrix into the back-deformed volume, arising as an alternative to inverting deformation matrices M_i directly, which may also be ill-posed problems. Figure 5.5 shows the relationship between the initial volume, deformed volume and the projections.

5.6 Attenuation Correction and Scatter Correction

Note that system matrix A actually includes attenuation and scatter. Attenuation and scatters maps are used to estimate the energy attenuation and scatter effect when the photon goes through the body. Transmission maps, CT or MRI can be used to estimate the attenuation map for the SPECT reconstruction.

For simulation purposes, we already have the corresponding attenuation map for the MCAT phantom. To simplify this process one can employ the triple energy window (TEW) scatter estimation method (Ogawa et al., 1991). In this method, scatter is estimated from scatter windows acquired simultaneously with the photopeak data. Thus, the scatter estimate naturally matches the motion state of the patient. To avoid the issue of negative values when the scatter estimate is subtracted from the acquired data

one can follow the methodology of (M. A. King and Case, 1997) and add the scatter estimation to the scatter-free projection data.

Since the patient body is an anisotropic object, we choose the ESSE scatter correction method (Ogawa et al., 1991) for the anisotropic patient body. In the following clinical experiments, we scan the patient with 2 beacon sources attached to the gamma camera for the transmission projections. The transmission projections are reconstructed into a transmission map, which is used to estimate the attenuation and scatter map.

Note that the attenuation map and scatter estimate should be modified to match the patient RM, RBM, and body deformation. The same movement or deformation should also be applied to the attenuation and scatter map to make the reconstruction compatible.

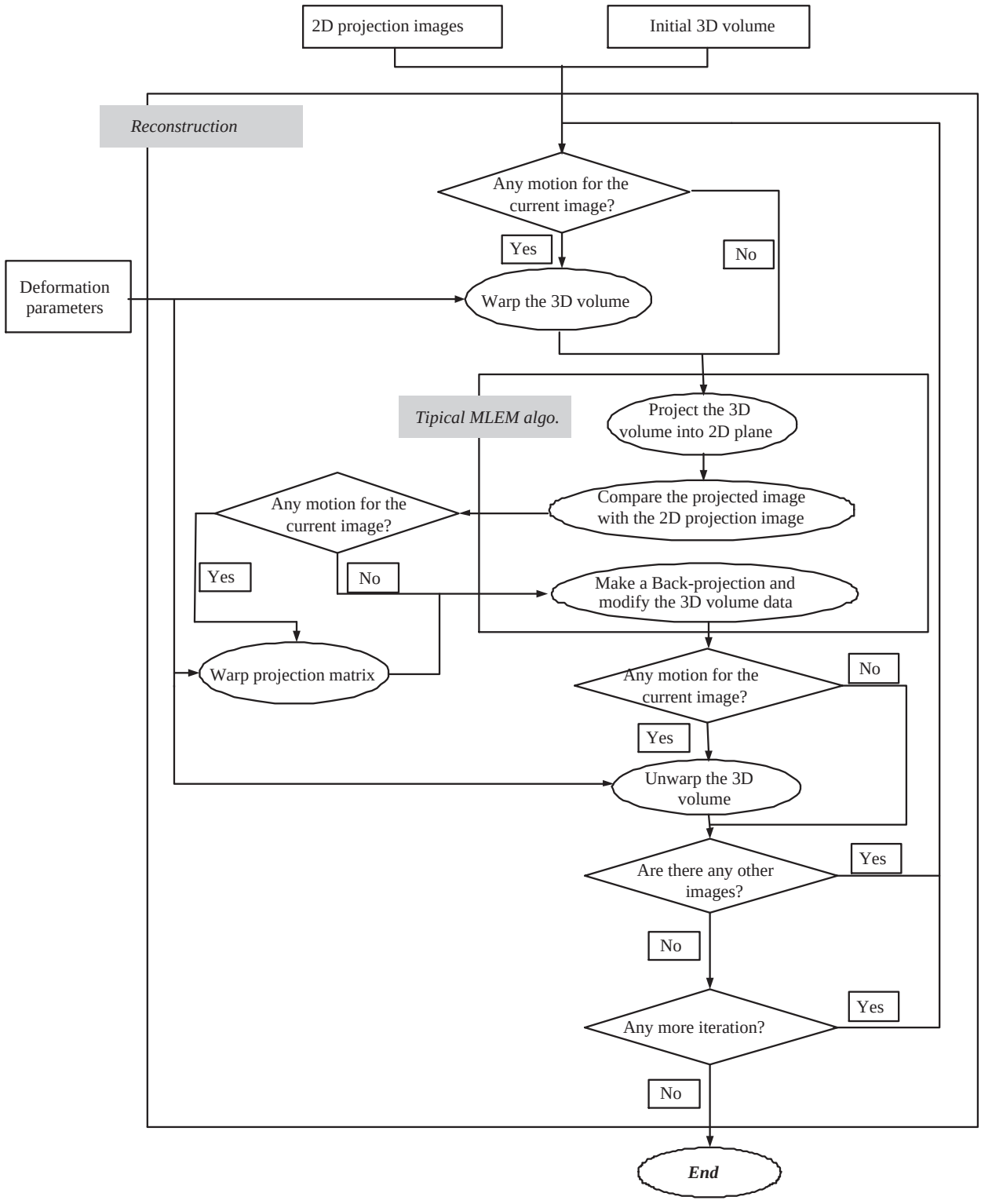

Figure 5.6: Procedure for the Modified MLEM algorithm.

Chapter 6

Simulation and Experiments

6.1 Marker Motion based Model Reversibility Verification

We have proposed a deformation model that is described by three major parameters: twist angle T, bend angle B, and bend direction D. Such parameters are computed by a set of marker coordinates. Before we use this model with volume data, we have to check the correctness of the model and verify its reversibility.

After parameters of the deformation model are determined, we should be able to back-deform any deformed voxel of the patient body to the initial position with the deformation parameters. The back-deformation operation is not a simple mathematical inverse computation for the chest belt, but a reverse operation of the deformation for the whole volume (Section 5.5). Since the deformation operation is composed of four steps— twist with T, rotation with $-D$, bend with B and rotation with D, the back-deformation also has four steps with the inverse order for each operation. Note the bend direction D keeps the same value for both the deformation and back-deformation procedure. In the back-deformation computation, we make a rotation with D, and bend with $-B$, rotation with $-D$ and twist with $-T$.

Returning now to motion detection, the surface markers that we have detected may be considered as a set of special voxels during the computation. We can back-deform the deformed surface markers to investigate the correctness of our back-deformation computation. Ideally, the initial chest markers (Figure 6.1a) should match the back-deformed chest markers (Figure 6.1b), which means the markers should also be reset

to the initial motionless positions. However, due to the inaccuracy of the motion estimation procedure, there will always be some errors in the back-deformation, leading to some discrepancy between these two results.

We performed an experiment to determine the extent of this discrepancy. For this experiment, a volunteer was outfitted with two belts with five markers each. The volunteer was instructed to make a series of deformations while lying on the imaging bed of the SPECT system. Optical cameras tracked the marker motion at a frame rate of 30 frames/sec. The location of the spine for use in these corrections was obtained by approximate measurement of 1/3 thickness of volunteer's body at the time of tracking. We first estimated and then applied RM and RBM corrections to make the abdomen belt stationary. The residual motion on the chest belt was considered as the input data for the body deformation computation. We then estimated body deformation as described above. Next, we applied a back-deformation operation to the chest markers to correct for the deformation. The deformation correction operation is the inverse of the deformation process. This back-deformation operation uses $-T$, $-B$, and D as the twist, bend, and bend direction to apply to the deformed markers. Thus, as an error measure we calculated the root-mean-square error $RMSE_{motion}$ for the x, y, and z components of the residual marker motions for each chest marker as

$$RMSE_{motion} = \sqrt{\frac{\sum_{i=0}^{K}\sum_{j=0}^{L}\left[(x_{jk}-x_{0k})^2+(y_{jk}-y_{0k})^2+(z_{jk}-z_{0k})^2\right]}{KL}} \tag{6.1}$$

where (x_{ij}, y_{ij}, z_{ij}) is the i-th marker's position in observation j, (x_{i0}, y_{i0}, z_{i0}) is the marker's reference position, L is the number of target markers, and K is the number of observations (valid records).

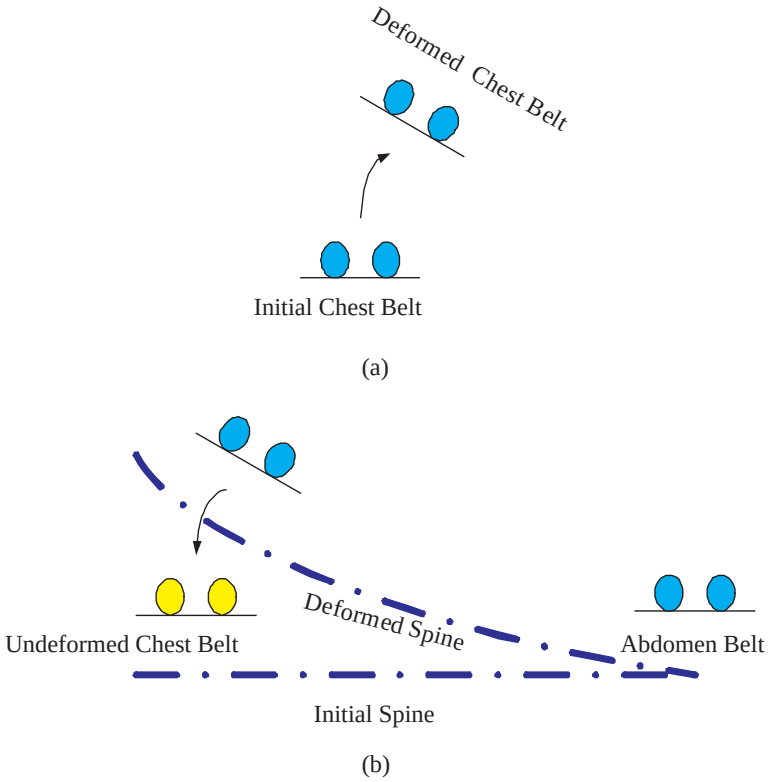

Figure 6.1: (a) Estimate twist, bend and bend direction with the chest belt only; (b) Back-deform the chest belt within the deformation model provided the twist, bend and bend direction as well as the abdomen belt position, the spine position and length.

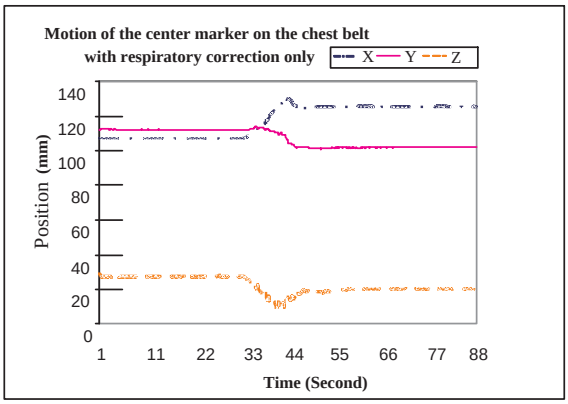

(a)

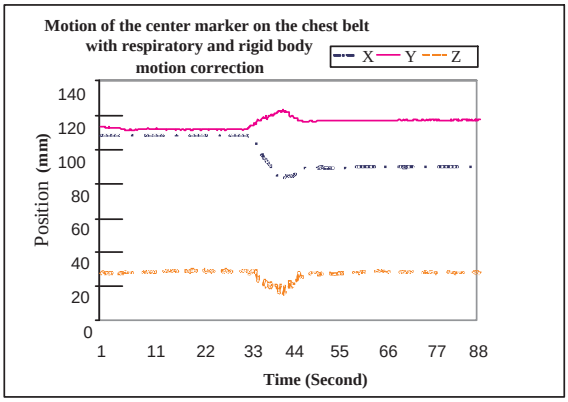

(b)

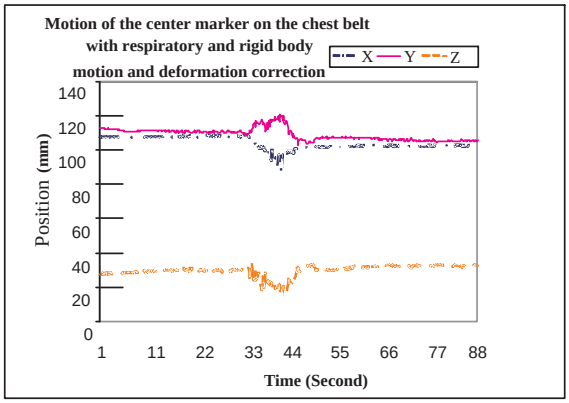

(c)

Figure 6.2: Comparison for the trace of one marker on the chest belt before and after deformation correction. (a) x, y, and z components of original tracked motion of center marker on chest band. (b) Motion after correction of rigid-body motion. (c) Motion after rigid-body and deformation correction. Note that stripping of respiratory motion is omitted here as it is small in amplitude for the chest marker compared to the other motions. The axes are illustrated in Figure 5.1. Note: in this experiment, we take the record 0 as the motionless pose of the volunteer.

Figure 6.2a shows the x, y, and z components (see Figure 5.1 of the tracked location of the center marker on the chest of a volunteer. Note that respiratory motion has been corrected before our processing (Mukherjee et al., 2009). We estimated the RBM based on the motion of the abdominal markers with the goal of making their locations stationary as required by our deformation model. After we acquired the RBM motion from the abdomen markers, we applied this RBM correction to the chest markers to estimate the chest marker's motion after the abdomen markers have been re-aligned to their initial positions (Figure 6.2b). Thus, any remaining motion of the chest markers indicates body deformation. We calculated the deformation parameters with the spine model as described above and applied deformation correction. The result, shown in Figure 6.2c, is a large decrease of the marker's motion in the x direction and moderate decreases of the marker's motion in the other 2 directions.

A comparison of the $RMSE_{motion}$ values for the five chest markers is shown in Figure 6.3. If there is no motion, $RMSE_{motion}$ is expected to be zero. We see that RBM correction reduced the $RMSE_{motion}$ value for some markers, while increasing it for others. Because rigid motion correction is with respect to the abdomen markers, this correction may increase the apparent motion of the chest markers. However, after deformation correction, the $RMSE_{motion}$ for all markers is greatly decreased. Another observation from Figure 6.3 is that if the marker is closer to the measurement center, the $RMSE_{motion}$ value is smaller. However, there are still some minor motions left. Thus unfortunately, totally robust results were not achieved because of model imprecision and measurement errors. We believe our model provides us a good starting point.

6.1.1 Spine Location Sensitivity

The spine position in the xy-plane is a crucial parameter for our motion estimation model. If available one can estimate the spine location from registered CT or MRI slices; however, this is not always available. Such was the case for the volunteer in this study. To measure the effect of errors caused by spine location mis-estimation, we investigated the effect of varying the spine location used in our deformation correction. The estimated locations varied from $-50mm$ to $+45mm$ in the x-axis and from $-65mm$ to $+60mm$ for the y-axis in $5mm$ steps about our selected location. A total of 520 spine locations were sampled in this way, giving us 520 sets of deformation parameters.

However, since the three parameters are highly correlated, it is hard to draw any conclusion by comparing the angle values directly. Then, we made the second step — a back-deformation computation based on these varying parameters. Therefore, we got 520 sets of back-deformation records of marker coordinates. Eq. 6.1 was used for $RMSE_{motion}$ value computation. Figure 6.4 shows the $RMSE_{motion}$ distribution map. The $RMSE_{motion}$ values vary from 9.65 to 14.34, increasing by the distance to the pre-measured spine location. The minimum $RMSE_{motion}$ value 9.65 is not far away from the $RMSE_{motion}$ value of the originally estimated spine location, which is 9.81. Therefore, the error caused by the spine location for the deformation parameter estimation is not large.

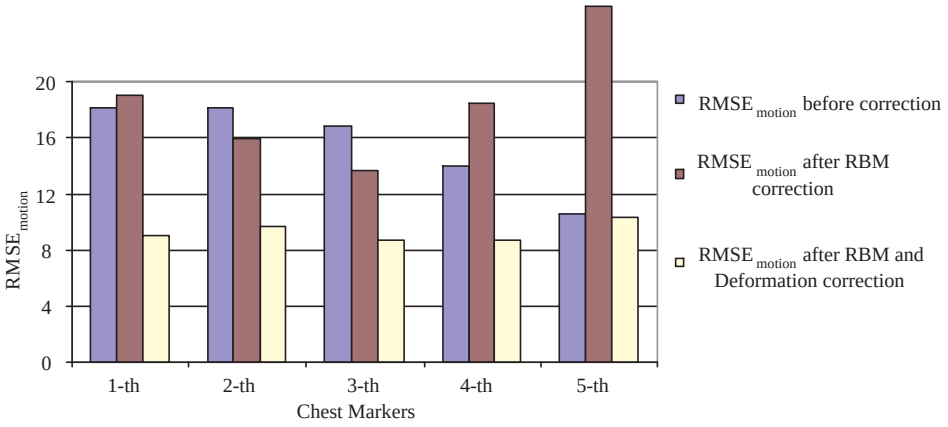

Figure 6.3: Comparison of $RMSE_{motion}$ for each marker on the chest belt.

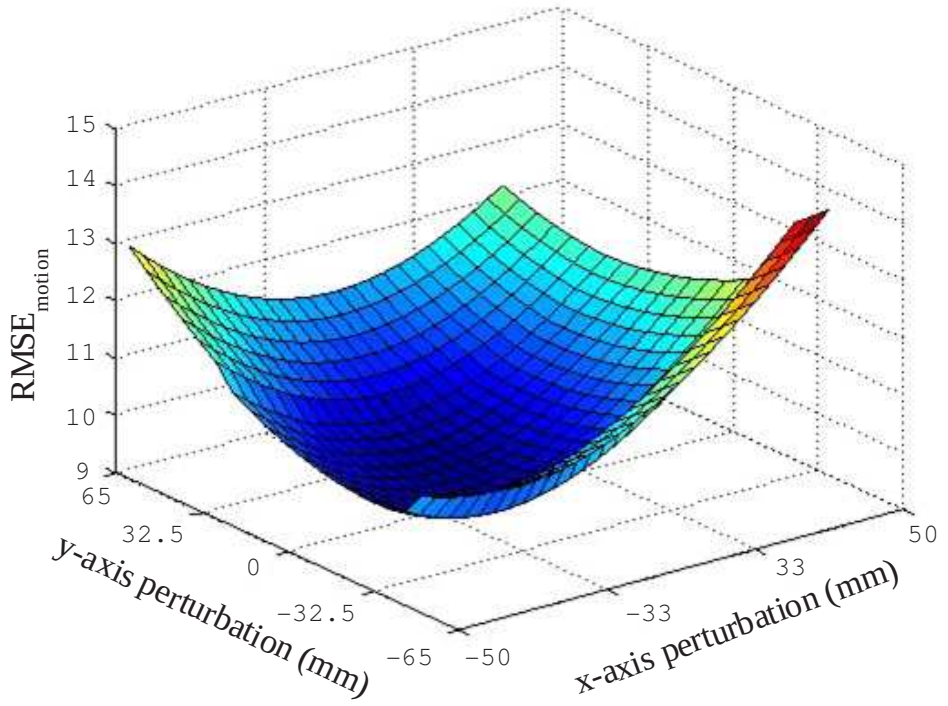

Figure 6.4: $RMSE_{motion}$ distribution for the xy-plane perturbation of the spine location.

6.2 MRI based Model Verification

Though we have shown that we can back-deform the markers to the initial positions, we still have to check whether we can correct all the voxels given the computed deformation parameters. We hypothesize that the total deformation is equally shared by all the joints and each unit of the vertebrae makes the same contribution to the total angle. Therefore, we can calculate the local twist angle T_v and local bend angle B_v for a given voxel v through Eq. 4.2 and Eq. 4.3. Though this is not completely accurate, this hypothesis should be reasonable.

To validate our hypothesis, we designed an MRI based experiment. First, we placed markers on a volunteer's torso and made sure the motion capture system could track them. Then, we had the volunteer undergo a regular MRI scan without any deformation. This MRI scan only required $20 - 30$ seconds. Thus, we expected that the 3D volume was not blurred by any deformation. Finally, the volunteer moved once and underwent a second scan, holding the same deformed pose throughout this second scan. In this motion, the volunteer's spine was expected to have some lateral curve. To minimize any respiratory effect, we required the volunteer to hold his breath during the entire two MRI scans. At the conclusion of the two scans, we had the 3D initial body volume data f_{init} and the deformed body volume data f_{deform}. After rigid-body motion correction, the volume f_{deform} was reshaped to the volume $f_{rigid-correct}$. Then, the 3D deformation parameters were computed as described. We next performed a back-deformation computation on the 3D deformed volume with the deformation model to build a new 3D body volume $f_{deform-corrected}$. There was no reconstruction computation required in this experiment. If our method is successful, the difference between the f_{init} and $f_{deform-corrected}$ should be quite small. In this research, we show two sets of MRI acquisition data, one shown from the coronal planes and another shown from the sagittal planes.

Figure 6.5 shows sample slices of MRI data taken from the same coronal views. The slice from f_{init} (Figure 6.5a) is evidently more different than the slice from f_{deform} (Figure 6.5b), especially around the spine area. After we corrected for the RBM (Figure 6.5c) and the body deformation with the deformation parameters specified in Section 4, we obtained $f_{deform-correct}$ (Figure 6.5d). The difference images between Figure 6.5a and Figure 6.5b,c,d are shown in Figure 6.5e,f,g. Figure 6.6 illustrates another sample of

	f_{init} vs. f_{deform}	f_{init} vs. $f_{rigid-correct}$	f_{init} vs. $f_{deform-correct}$
$RMSE_{MRI}$	15.57	14.52	12.17

Table 6.1: Comparison among the MRI volumes by $RMSE_{MRI}$.

similar motion and deformation correction using MRI data taken from a single sagittal plane.

Though we have required the volunteer to hold his breath, cardiac motion still exists during the MRI data acquisition. Since we did not perform cardiac gating, the heart is in constant motion during MRI data acquisitions, making it meaningless to compare the cardiac area among the three MRI data sets. However, the spine area had no such periodic motion. From Figure 6.6d, it is clear that spine, as shown in the corrected slice, is similar to the spine in the initial slice. On the other hand, the deformed slice (Figure 6.6b) only shows a part of the spine due to the deformation. Since the sagittal plane included the artery and heart area, which is not gated in our experiment, we choose the coronal plane based experiment to compare the correction results. We select the spine area in the MRI data as the target for comparison. We define the Root Mean Square Error ($RMSE_{MRI}$) value as:

$$RMSE_{MRI} = \sqrt{\frac{\sum_{i=0}^{n} |I_1 - I_2|^2}{n}} \tag{6.2}$$

where I is the image intensity. I_1 means the intensity of the corrected volume and I_2 means the intensity of the motionless volume. Error values are shown in Table 6.2. We see that using our model for deformation correction restores the deformed volume more closely to the initial back-deformed volume better than RBM correction only. Though we cannot restore the volume to the exact initial position, due to the model inaccuracy and measurement noise, we can make the deformed volume closer to the initial volume. From the result above, we claim that our correction method works reasonably for one subject and one movement.

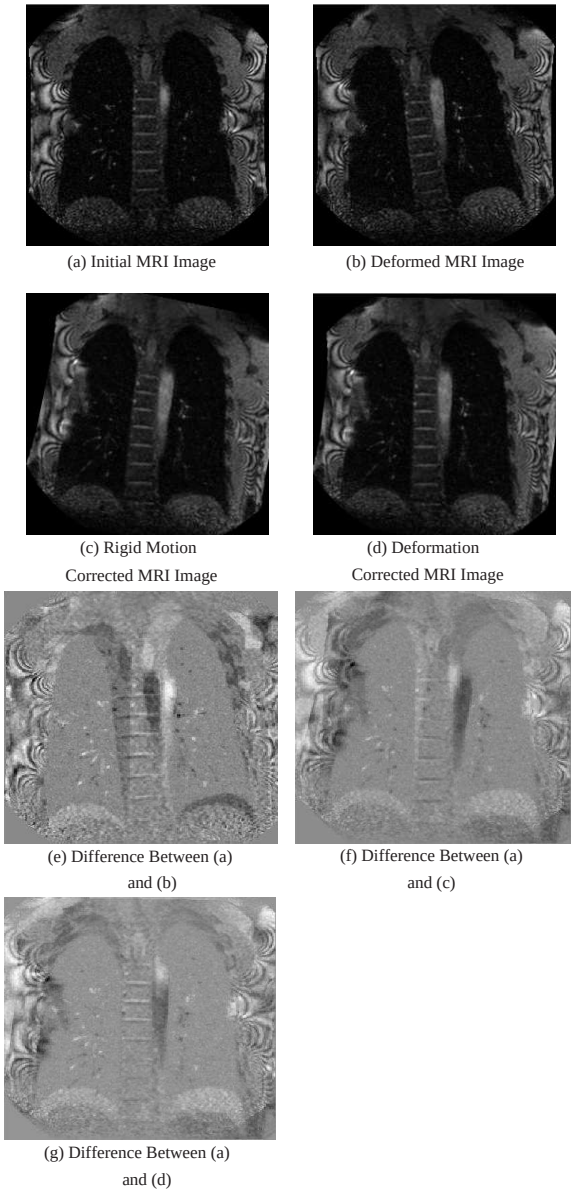

(a) Initial MRI Image

(b) Deformed MRI Image

(c) Rigid Motion Corrected MRI Image

(d) Deformation Corrected MRI Image

(e) Difference Between (a) and (b)

(f) Difference Between (a) and (c)

(g) Difference Between (a) and (d)

Figure 6.5: Comparison of a coronal slice in the MRI data with resolution $1.7mm \times 6.0mm \times 1.7mm$ for each voxel. (a) Slice from f_{init}; (b) Slice from f_{deform}; (c) Slice from $f_{rigid-corrected}$; (d) Slice from $f_{deform-correct}$; (e) Difference image between (a) and (b); (f) Difference image between (a) and (c); (g) Difference image between (a) and (d).

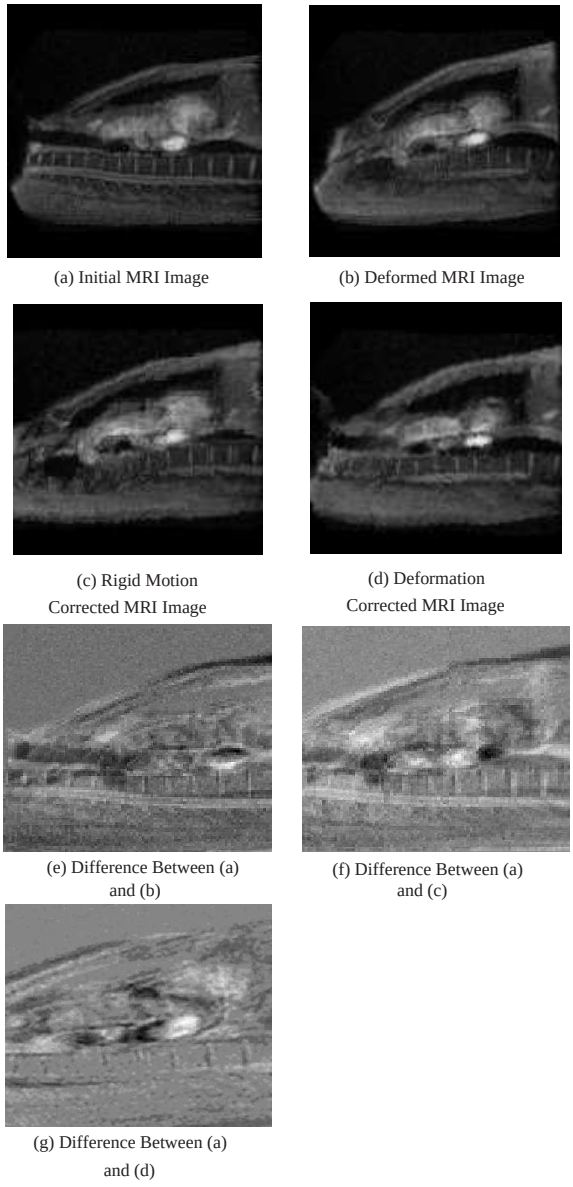

(a) Initial MRI Image

(b) Deformed MRI Image

(c) Rigid Motion Corrected MRI Image

(d) Deformation Corrected MRI Image

(e) Difference Between (a) and (b)

(f) Difference Between (a) and (c)

(g) Difference Between (a) and (d)

Figure 6.6: Comparison of a sagittal slice in the MRI data $6.0mm \times 1.7mm \times 1.7mm$ for each voxel. (a) Slice from f_{init}; (b) Slice from f_{deform}; (c) Slice from $f_{rigid-corrected}$; (d) Slice from $f_{deform-correct}$; (e) Difference image between (a) and (b); (f) Difference image between (a) and (c); (g) Difference image between (a) and (d).

6.3 Simulation with MCAT Phantom

To test our method of deformation correction we created source and attenuation distributions for Ga^{67} citrate imaging using the mathematical cardiac torso (MCAT) anthropomorphic phantom (Ue et al., 2005) (Kovalski et al., 2007). Ga^{67} citrate was selected as the radiopharmaceutical to investigate correction of body deformation due to it having uptake in spine and organs throughout the thorax. The relative distribution in the body structures was set to heart = 1.0, sternum and spine = 5.2, ribs = 2.6, spinal cord = 7.2, kidneys = 2.6, liver = 5.6, spleen = 8.2, lungs = 0.3, and background = 0.4 based on post-mortem studies of activity localization in humans (Mukherjee et al., 2009). The source distributions were $256 \times 256 \times 256$ with a voxel size of 0.208 cm. The values in the attenuation map were those for the effective value of the combination of imaging the two lower energy photo peaks of Ga^{67} (93 and 184 keV) (Cit,). The source and attenuation maps were deformed by varying all 3 of the deformation model parameters and with knowledge of the location of the spine height within the body, just like the volume deformation. We performed a simulation with bend angle B = 25^o, twist angle T = 15^o and bend direction of =15^o from coronal direction.

An analytical projector that included the impact of attenuation and distance-dependent spatial resolution was used to create the projections. We did not include scatter in our simulation. We modeled the acquisition from three camera heads at 120 degrees relative to each other, as for a bone SPECT acquisition on our Philips Irix SPECT system. The acquisition consisted of 120 projections in total with 40 acquired by each head. We made two projection sets. The first projection set P_{init} (Figure 6.7a) is projected without any deformation. The second projection set P_{deform} (Figure 6.7b) was projected with a pre-defined deformation. Since the following MLEM reconstruction included attenuation correction, the attenuation map was deformed corresponding to the deformation of the MCAT phantom when creating P_{deform}.

Once the projection sets were created, projections P_{init} from the original motion volume and projections P_{deform} from the deformed volume were mixed for a new projection file P_{mix} to simulate a simple patient deformation occurring halfway through the acquisition. Since we simulated a three head SPECT system, any motion affected 3 projections simultaneously. So we took 60 projections from P_{init} ($1-20$, $41-60$, $81-100$) and 60 projections from P_{deform} ($21-40$, $61-80$, $101-120$) and mixed them

for a new projection set P_{mix}.

The projection sets P_{init} and P_{mix} were reconstructed with 24 iterations of MLEM using Eq.. 5.20. All the reconstructions included attenuation correction. The attenuation map employed when deformation was present was that of the MCAT attenuation distribution deformed using the motion model employed within reconstruction. Scatter correction was not included as scatter was not included in forming the projections.

The reconstruction from P_{init} was taken as the standard against which the reconstructions of P_{mix} were compared for: 1) no motion compensation, 2) motion compensation using the correct spine location, and 3) motion compensation with inaccurate spine locations. The inaccuracy of the spine location would introduce an error into the deformation correction. We will investigate the error caused by spine location inaccuracy later.

The simulation procedure is shown as follows:

1. Get original 3D body data R_{init} from MCAT phantom.

2. Project R_{init} into 2D to get the projection image set P_{init}.

3. Reconstruct using P_{init} to get the benchmark $R_{no-deform}$.

4. Deform the original 3D data R_{init} to get deformed 3D data $R_{deformed}$ and deform the original attenuation map to get deformed attenuation map. We will assign the value for twist, bend and bend direction. Then with these three degrees of freedom, we can make an deformation computation. (Figure 6.7)

5. Project the deformed data $R_{deformed}$ to get the projection image set P_{deform} with the deformed attenuation map.

6. Replace several images in the image set P_{init} with the corresponding images in the image set P_{deform} and export these images as a new image set P_{mix}. This simulates a patient undergoing periods of non-rigid motion.

7. Reconstruct using image set P_{mix} with the traditional MLEM algorithm to produce the reconstruction result $R_{no-correction}$.

8. Reconstruct using image set P_{mix} with motion correction and the modified MLEM algorithm to produce the reconstruction result $R_{correction}$.

9. Compare the two reconstruction data volumes $R_{no-correction}$ and $R_{correction}$ with the original data $R_{no-deform}$, to conclude which result is better.

To quantitatively evaluate the impact of motion compensation, the root-mean-square error ($RMSE_{recon}$) of reconstruction (with and without motion compensation)

was calculated by

$$RMSE_{recon} = \sqrt{\sum_{i \in ROI} \frac{(counts_i - true_counts_i)^2}{N}} \tag{6.3}$$

where N is the number of voxels inside the ROI, $counts_i$ and $true_counts_i$ are the counts in the slices reconstructed from P_{init} for voxel i.

In this simulation, we have an attenuation map for the MCAT phantom in the initial position. Note that the attenuation map and scatter estimate should be modified to match the patient RM, RBM, and body deformation. To simplify the process, we did not apply scatter correction. Reconstruction was performed 24 iterations of MLEM.

The results of applying the deformation correction to SPECT simulations are illustrated in Figure 6.8, which shows transverse slices through the heart region of the MCAT phantom. Figure 6.8a is a slice from the reconstruction R_{init} when there was no motion in the projections; Figure 6.8b is a slice of $R_{no-correction}$ for when deformation was included in half of the projections without deformation correction in the reconstruction, and Figure 6.8c is a slice of $R_{correction}$ for when deformation was included in half of the projections and the deformation correction was included in reconstruction. Notice the significant degradation caused throughout the slice by the deformation and how well deformation correction returns the distribution to its original appearance. Numerically, deformation correction reduced the $RMSE_{recon}$ from 4.1×10^{-2} between R_{init} and $R_{no-correction}$ to 3.4×10^{-3} between R_{init} and $R_{correction}$, thus verifying the visual impression of a considerable improvement. Figure 6.9 shows coronal slices illustrating the impact of deformation and its correction on the spine, ribs, liver, and kidneys. Note the obvious bend of the spine laterally and its correction. Also note that the kidneys are not impacted by the bend or its correction as they were outside the ROI where it occurred.

6.3.1 Spine Location Sensitivity

The spine location is a crucial parameter for the accuracy of our correction algorithm. To apply our deformation correction method for clinical data, we have to understand how much effect the measure error will have on the reconstructed volume. Therefore, based on this simulation, we added a small perturbation, from $-15mm$ to $15mm$, to

the x, y coordinates of the spine location respectively, with each sample step $5mm$. So we had 49 reconstructed volume with different spine location perturbations. The $RMSE_{recon}$ values were computed between all the reconstructed volumes and the baseline volume $R_{no-deform}$. In this research, we consider an improvement when we have the less value of the $RMSE_{recon}$, which indicates how close tow volumes are.

Figure 6.10 shows the results of our study of the sensitivity of deformation correction to the identification of the spine location. The $RMSE_{recon}$ values increase quickly as the magnitude of error increases. The values vary from 3.4×10^{-3} to 2.1×10^{-1} when the spine location was uniformly distributed in the $900mm^2$ area about the actual location. Therefore, it appears that our methodology is sensitive to the spine location parameter used in deformation correction and that correction would work best when there are registered CT or MRI slices available to provide an accurate estimate of this location.

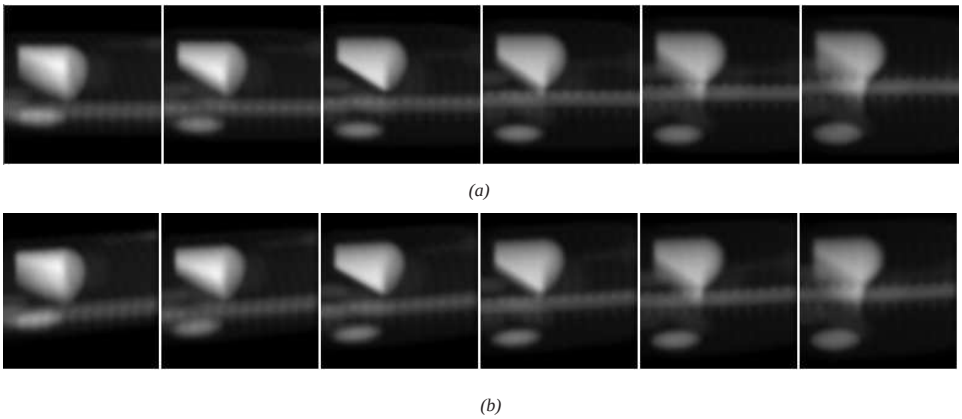

Figure 6.7: (a) Several projections of the initial phantom. (b) Several projections of the deformed phantom.

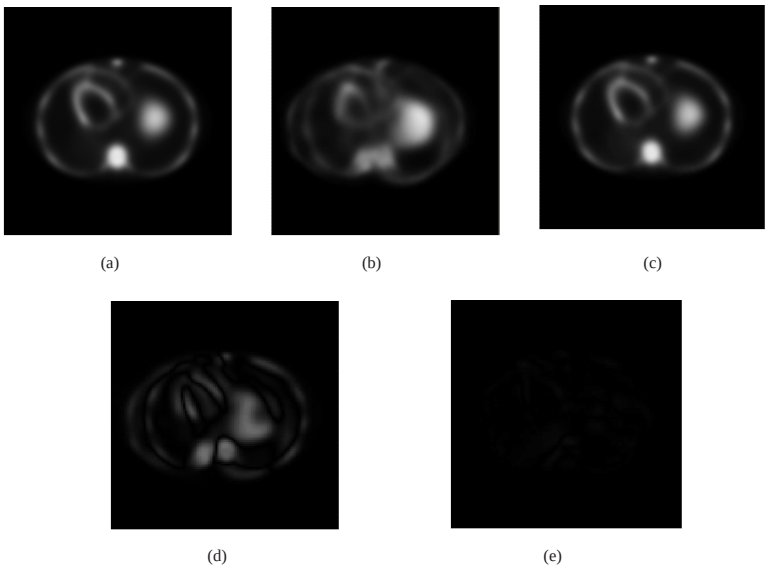

Figure 6.8: Comparison of transverse reconstruction slices from (a) MCAT projection set that did not include deformation, (b) MCAT projection set that included deformation but no reconstruction deformation correction, (c) MCAT projection set that included deformation and with deformation correction during reconstruction, (d) difference between (a) and (b), and (e) difference between (a) and (c).

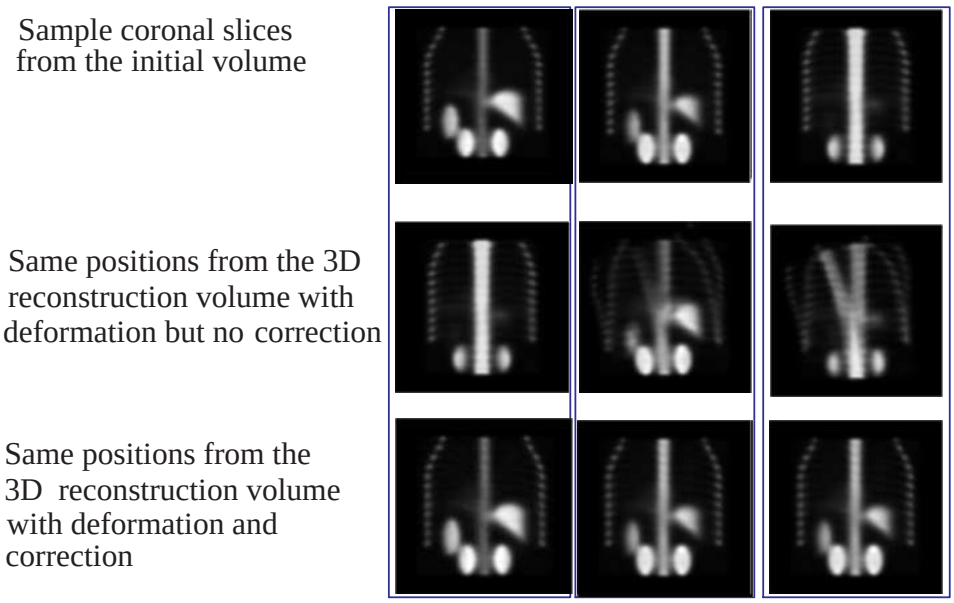

Figure 6.9: Coronal slices illustrating the impact of deformation and its correction on the spine, ribs, liver, and kidneys. Note the obvious bend of the spine laterally and its correction. Also note that the kidneys are not impacted by the bend or its correction as they were outside the ROI where it occurred.

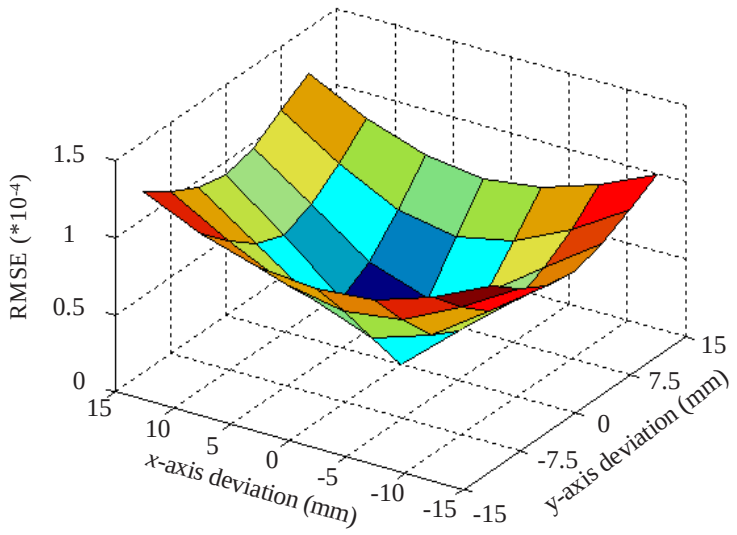

Figure 6.10: $RMSE_{recon}$ distribution of reconstruction results considering the xy-plane perturbation of the spine location.

6.4 SPECT Clinic based Experiment

To validate our motion correction methods, we designed an experiment with a patient. We made a 2-acquisition procedure, similiar to taht described in Section 6.3. This procedure is used to verify that our method was valid not only for a phantom, but also for a patient. Since RM correction was a very small part of motion compared with RBM and deformation, we did not apply RM correction in this experiment. We wanted to study practical problems that were not emphasized in the simulation.

6.4.1 Clinic Data Acquisition

Our target patient was a subject undergoing a Tl^{201} cardiac perfusion study. A motion capture system was set up in the clinic with three cameras observing the patient from the head end and two cameras observing from the foot end. The cameras were used to image retro-reflective markers attached to belts on the patient body, one belt on the chest and another on the abdomen. Five retro-reflective markers were put on the chest belt and three were placed on the abdomen belt. The marker patterns were carefully adjusted so that each marker was visible to at least two of the cameras at all times during the SPECT acquisition.

After the patient was positioned in the center of the SPECT machine, a transmission scan was acquired to obtain for a transmission map. To simplify the problem, the patient was required to stay still during this scan. Then our synchronization module was launched to trigger both the SPECT machine and the motion capture system. The synchronization module is used to relate the times between the SPECT data acquisition and the marker motion data. During the 12 minutes of SPECT data acquisition, the gamma camera rotated around the patient acquiring frames every three degrees, with 20 seconds acquisition time per frame. 68 projections (Figure 6.12) from two gamma cameras were collected as the projection data. During the acquisition, the infrared cameras were capturing the markers' positions at 30 frames/sec and the 3D trajectories of each marker were computed. The sequences of 3D trajectories were a motion data and used for the motion estimation.

In this experiment, we acquired two 12 minute SPECT acquisitions. Since the patient was required to remain still in the first acquisition, the reconstruction of the projections from this acquisition was considered as our motion-free baseline. In the

second acquisition, the patient was allowed to perform random movements on the table during the acquisition. The projections from the second acquisition were used for the reconstructions with and without deformation correction. After these acquisitions, we had two sets of projections corresponding to two sets of motion data from our motion capture system.

6.4.2 Data Processing

In this experiment, we used the frame mode based reconstruction for its simplicity. We assume that the patient position changes little during each frame and can be related to one set of corresponding motion parameters. We calculated the mean motion parameters for each projection. Note the motion data rate was 30 frames per second. On the other hand, the projection rate was around 20 seconds per image. We had to determine a time model for the motion of each frame. Based on the synchronization module, we could determine which motion data were collected within a certain projection. The motion data were put into both RBM estimation module (Feng et al., 2005) and our deformation estimation module. There are 6 DOF in the RBM estimation module-3 for translation and 3 for rotation. For the translation, we chose the mean values of translation vector as the translation vector of the target projection. For the rotation, we extracted the 3 rotation angles around the 3 axes from the rotation matrix. The rotation order could be arbitrarily decided. The mean values of the 3 rotation angles were taken as the rotation angles belonging to a certain projection. Then we calculated the rotation matrix with the mean rotation angles. Note that the axes angle order had to be preserved when we do the angle extraction.

As to the deformation model, each set of motion data had 3 parameters—twist angle, bend angle and bend direction. Similarly, we could take the mean value of each parameter sequence belonging to a certain projection as the deformation parameter.

The modified MLEM algorithm (Eq. 5.20) was used for the reconstruction because it could be adapted for motion correction. Since the patient undergoes different motions for different projections, the reconstruction volume should be moved or warped based on the motion parameter to properly align the reconstruction data. In turn, the attenuation map should also be moved or warped with the reconstruction volume. In our reconstruction computation, we used the ESSE scatter correction (Frey and Tsui,

1993), in which the scatter map was deduced from the attenuation map (Figure 6.11).

Figure 6.11: Sample images from the attenuation map.

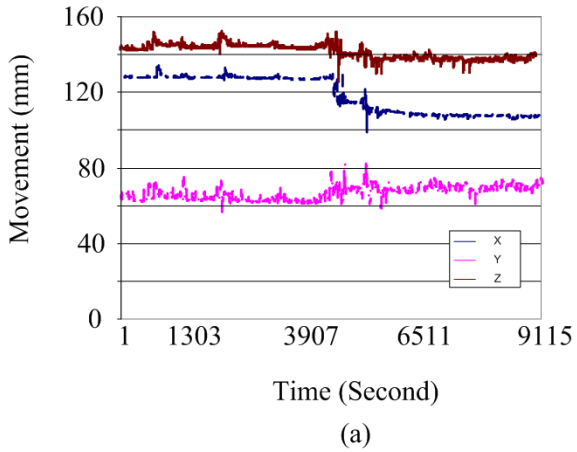

(a)

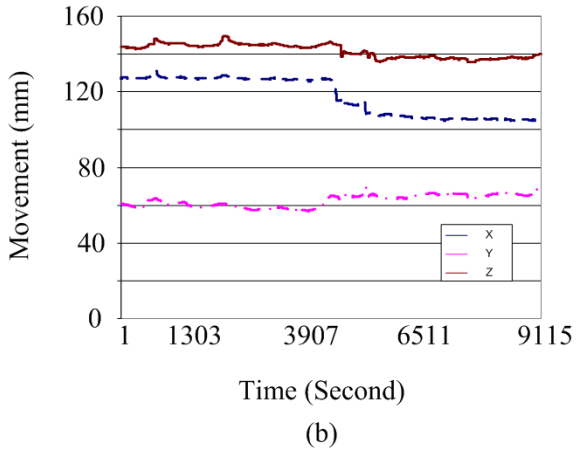

(b)

Figure 6.12: (a) Raw data of one chest marker motion during the second acquisition. (b) Motion after RM correction.

6.4.3 Results and Comparison

When we applied our correction methods to the reconstruction, the markers on the abdomen belt were used to estimate the RBM parameters. Figure 6.13a shows the motion trace of one chest marker after RM correction. Figure 6.13b shows the motion trace of that marker after the RM correction and the abdomen belt based RBM correction. Given the spine location and the marker remaining motion data, we used our deformation correction algorithm to measure the deformation parameters. A back-deformation computation was also applied to the marker motion data. Figure 6.13c shows the motion trace of one chest marker after RM, RBM and deformation correction. The $RMSE_{motion}$ (Eq. 6.1) decreased from 6.46 (RM correction only) to 6.07 (RM and RBM correction) to 5.42 (RM, RBM and deformation correction). After we estimated the deformation parameters, we could use the parameters to correct the second SPECT acquisition.

There are some unexpected pulses of the marker's positions after deformation reconstruction (Figure 6.13). In our model, we assume the spine length is fixed and each vertebra has the same contribution to the deformation, which is not completely accurate. When the patient was undergoing some motion, the deformation of the moving torso was highly unpredictable. However, when the patient stayed still again after the motion, the body would comply to our deformation model again.

Some of the projections in the first acquisition are shown in Figure 6.14a and some of the projections in the second acquisition are shown in Figure 6.14b. Though we had detected the patient motion by the motion capture system, it was hard to see the motion effect based on the projection images. Before the comparison, we performed a reconstruction with the traditional MLEM algorithm without any motion correction for both projection sets. Again, we used $R_{nomotion}$ for the reconstruction volume without any motion and $R_{no-correction}$ for the reconstruction volume with motion but no correction. One slice from $R_{nomotion}$ is shown in Figure 6.15a. The heart (bright circle) is fine. The slice for the same position from $R_{no-correction}$ is shown in Figure 6.15b. Without any correction, the heart (bright blur area) is highly distorted. It is quite clear that for the second acquisition motion correction is needed.

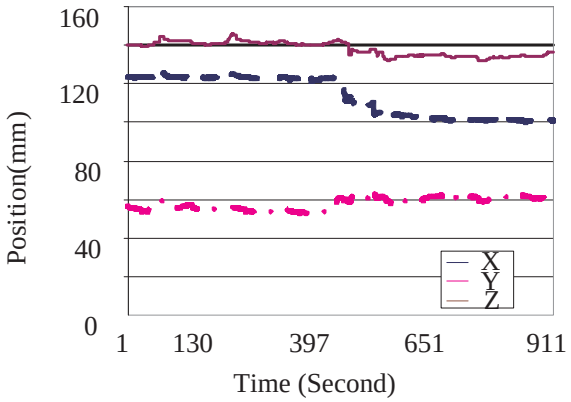

(a)

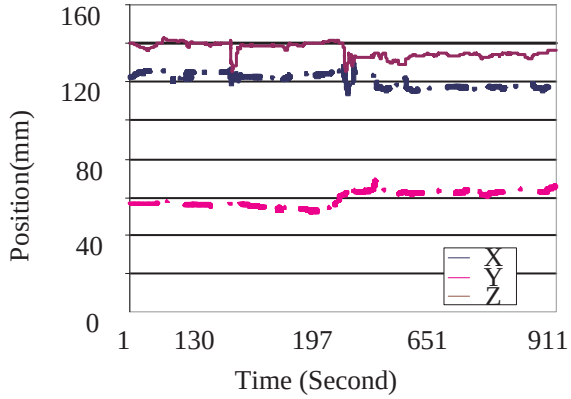

(b)

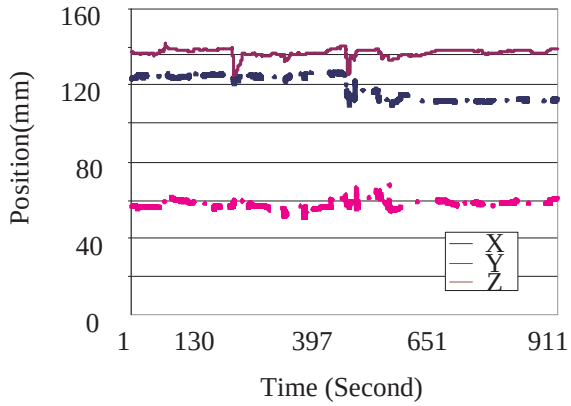

(c)

Figure 6.13: (a) Motion of one chest marker after RM correction. (b) Motion of one chest marker after RM and RBM correction. (c) Motion of one chest marker after RM, RBM and deformation correction.

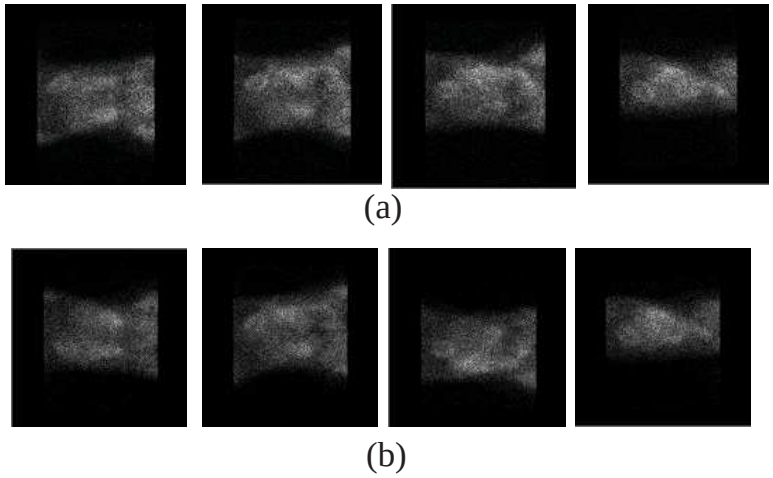

Figure 6.14: (a) Raw projections from the first acquisition. (b) Raw projections from the second acquisition with some motion involved.

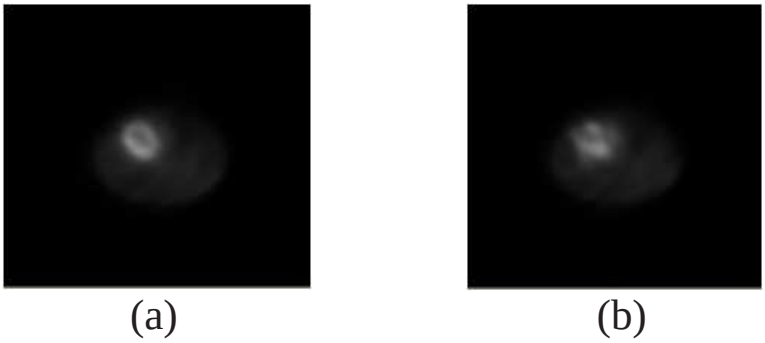

Figure 6.15: (a) One slice from the reconstruction of the first acquisition. (b) One slice from the reconstruction of the second acquisition.

We applied the motion correction modules for the second acquisition data. For comparison purpose we made two kinds of motion correction. To simplify the process, in this experiment, we omit the RM correction due to the small amplitude. The first correction was the traditional RBM correction (Feng et al., 2003), which considered the body as a whole object. In this procedure, all the markers were involved in the RBM estimation. The relative motion between different belts was omitted. We used R_{rigid} for the reconstruction volume with motion and RBM correction only. The second correction was the RBM correction combined with the deformation correction. RBM parameters were estimated from the abdomen belt markers and the deformation parameters were estimated from the chest belt markers after we applied RBM correction for the chest belt markers. Then we applied RBM correction and deformation correction for the reconstruction. We used $R_{allcorrection}$ for the reconstruction volume with motion, RBM correction and deformation correction. $R_{nomotion}$ is reconstructed from the first acquisition and the other 3 volumes are reconstructed from the second acquisition. The patient body did change between these two acquisitions. The difference between $R_{nomotion}$ and $R_{allcorrection}$ is inevitable.

Based on these parameter list and the projections, we could make our motion correction computation. In this reconstruction, RM is ignored due to the minor contribution to the entire motion. Figure 6.16 shows a comparison from the coronal plane. In Figure 6.16a, the liver is highlighted in the reconstruction volume. In Figure 6.16b and c, the liver area is dimmed. The motion degraded the concentration of the radioactivity. However, after our deformation correction, the liver area is bright again in Figure 6.16d.

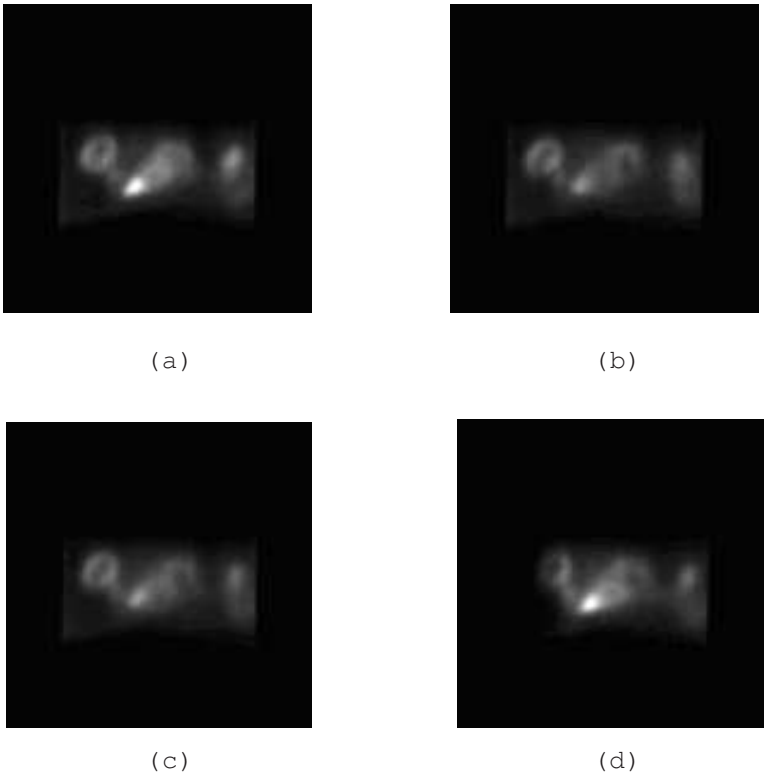

Figure 6.16: (a) Coronal slice from $R_{nomotion}$. (b) Coronal slice from $R_{no-correction}$. (c) Coronal slice from R_{rigid}. (d) Coronal slice from $R_{allcorrection}$. Note: the hot circle is the spleen.

The $RMSE_{recon}$ between the volumes $R_{no-correction}$, R_{rigid}, $R_{allcorrection}$ and $R_{nomotion}$ is going down from 0.19 (no correction), to 0.16 (RBM correction), to 0.10 (RBM and deformation correction). Note the maximum value of the voxels is 5.74. Based on our analysis, our deformation model improves the reconstruction quality and compensates for the deformation effectively.

Since the heart perfusion is the focus point of our study, we extract the heart area and analyzed the heart reconstruction. Figure 6.17 shows that we extract the heart area from the Figure 6.17a,b,c,d. Then we abstracted (a) from (b), (c) and (d). The difference images are shown in (e), (f) and (g). The difference between (a) and (d) are quite small, with the $RMSE_{recon}$ value only 0.17. However, we can see strong pattern in the difference images (e) and (f). The $RMSE_{recon}$ value is 0.50 between $R_{nomotion}$ and $R_{no-correction}$, and is 0.36 between $R_{nomotion}$ and $R_{rigidcorrection}$. Based on this comparison, we can claim we have restored the heart into the initial shape even with deformation in the acquisition. More sample slices are shown in Figure 6.18.

The experiment was repeated for a second patient. In Figure 6.19a, the patient's heart is shown clearly. After motion, this patient heart is distorted to be a bright point in Figure 6.19b. The reconstruction with RBM correction only is shown in Figure 6.19c. The reconstruction with RBM and deformation correction are shown in Figure 6.19d. The patient heart is corrected in $R_{allcorrection}$ since we can distinguish the two ventricles, not only a bright point in $R_{nocorrection}$ without any correction. The $RMSE_{recon}$ around the heart area goes down from 0.30 between $R_{nomotion}$ and $R_{nocorrection}$, to 0.23 between $R_{nomotion}$ and $R_{rigidcorrection}$, to 0.18 between $R_{nomotion}$ and $R_{allcorrecion}$. Note the maximum counts in $R_{nomotion}$ are 2.74. More results from this experiment are shown in Figure 6.20.

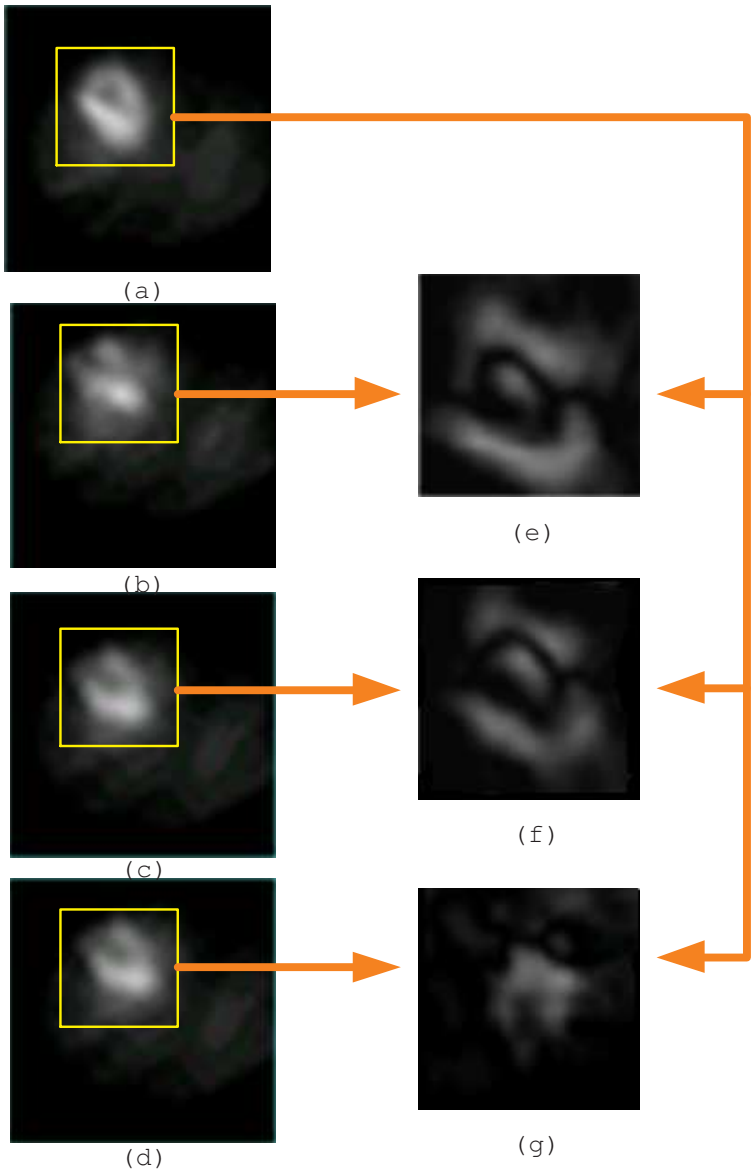

Figure 6.17: Comparison between transverse slices from the reconstructions of the first experiment. (a) 43^{th} slice from $R_{nomotion}$. (b) 43^{th} slice from $R_{nocorrection}$. (c) 43^{th} slice from R_{rigid}. (d) 43^{th} slice from $R_{allcorrection}$. Note: the hot circle is the heart. (e) Difference image between the heart area of (a) and (b). (f) Difference image between the heart area of (a) and (c). (g) Difference image between the heart area of (a) and (d).

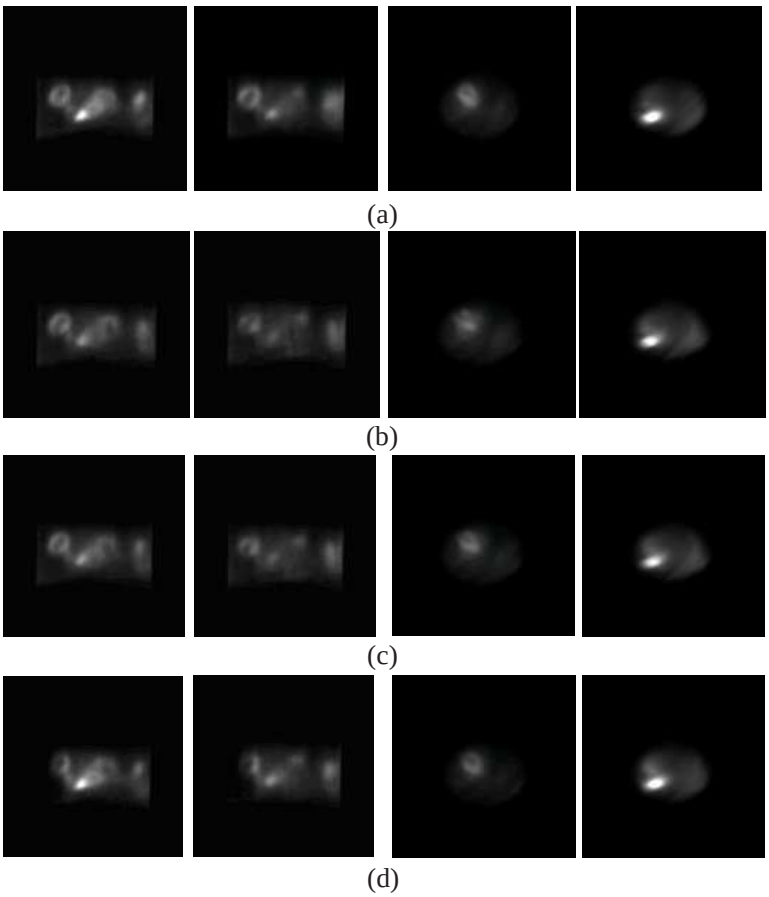

Figure 6.18: Transverse slices from the reconstructions of the first experiment. (a) Slices from $R_{nomotion}$. (b) Slices from $R_{no-correction}$. (c) Slices from R_{rigid}. (d) Slices from $R_{allcorrection}$. Note: the left two columns are the 56^{th} and the 60^{th} slices in the sagittal plane; the right two columns are the 43^{th} and the 56^{th} in the transverse plane.

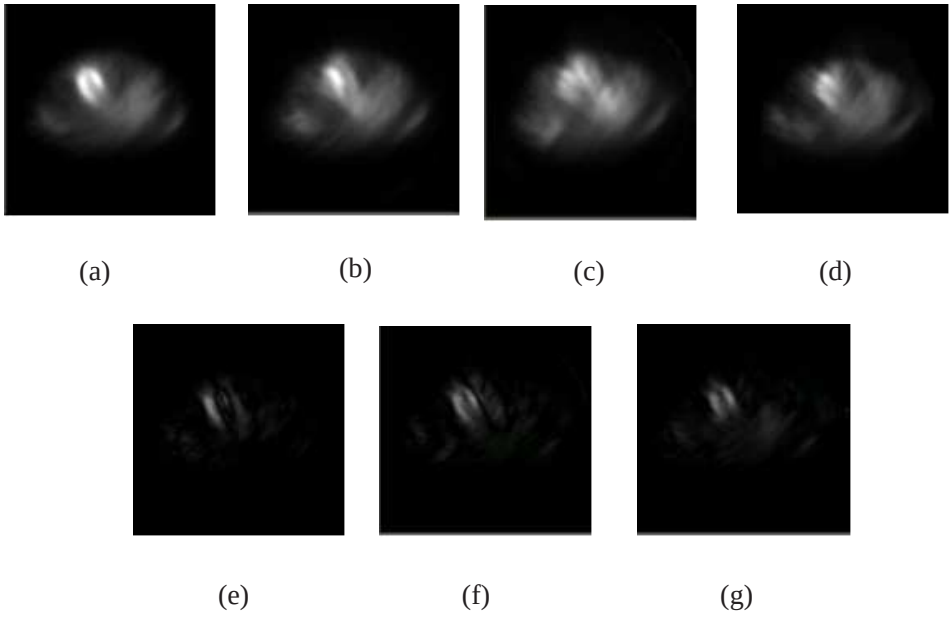

Figure 6.19: Comparison between transverse slices from the reconstructions of the second experiment. (a) 48^{th} slice from $R_{nomotion}$. (b) 48^{th} slice from $R_{no-correction}$. (c) 48^{th} slice from R_{rigid}. (d) 48^{th} slice from $R_{allcorrection}$. Note: the hot circle is the heart. (e) Difference image between the heart area of (a) and (b). (f) Difference image between the heart area of (a) and (c). (g) Difference image between the heart area of (a) and (d).

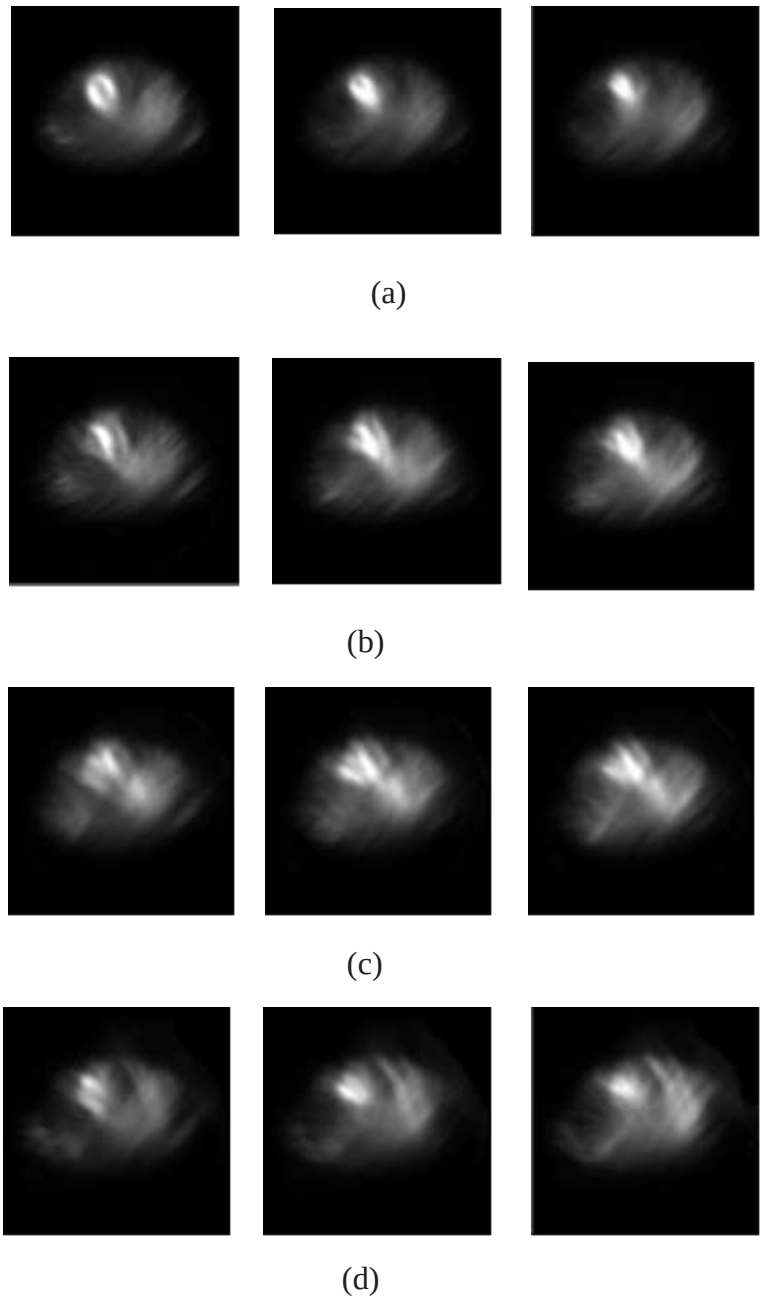

Figure 6.20: Transverse slices from the reconstructions of the second experiment. (a) Slices from $R_{nomotion}$. (b) Slices from $R_{no-correction}$. (c) Slices from R_{rigid}. (d) Slices from $R_{allcorrection}$.

In the third experiment, the patient made some RBM as well as RM. However, the patient did not have clear deformation during the acquisition. The marker's motion before and after motion correction is shown in Figure 6.21. We notice that after RBM correction the target marker is almost stable. Therefore, the deformation correction has a minor contribution to the motion correction.

Figure 6.22 is a set of sample slices in the same position of the reconstructed volumes. In Figure 6.22a, the patient's heart is shown clearly in $R_{nomotion}$. Again, after motion, this patient heart is distorted to be a bright point in Figure 6.22b. The reconstruction with RBM correction only is shown in Figure 6.22c. The reconstruction with RBM and deformation correction are shown in Figure 6.22d. The patient heart is corrected in $R_{allcorrection}$. The $RMSE_{recon}$ around the heart area goes down from 0.22 between $R_{nomotion}$ and $R_{nocorrection}$, to 0.17 between $R_{nomotion}$ and $R_{rigidcorrection}$, to 0.17 between $R_{nomotion}$ and $R_{allcorrecion}$. Note the maximum counts in $R_{nomotion}$ are 3.98. Since the patient had almost no deformation, the contribution of the deformation module was insignificant. However, our module does not degenerate the improvement made by the RBM correction module. More results from the third experiment are shown in Figure 6.23.

One Marker Motion with RM correction Only

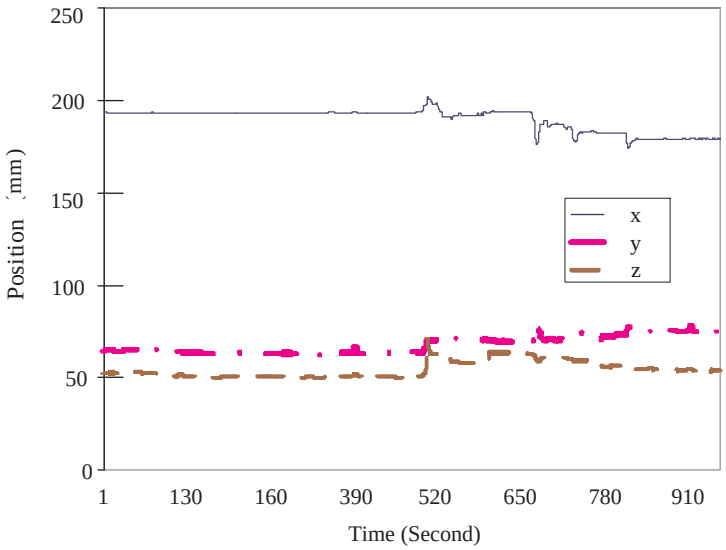

One Marker Motion after RM and RBM Correction

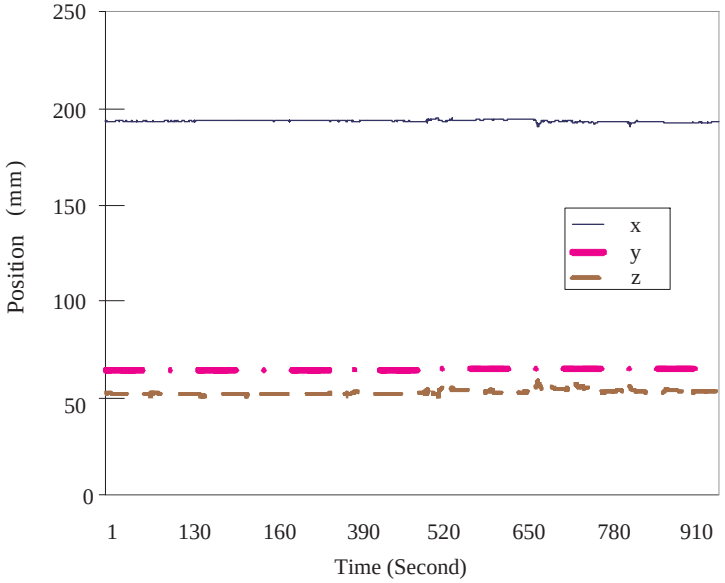

One Marker Motion after RM, RMB and Deformation Correction

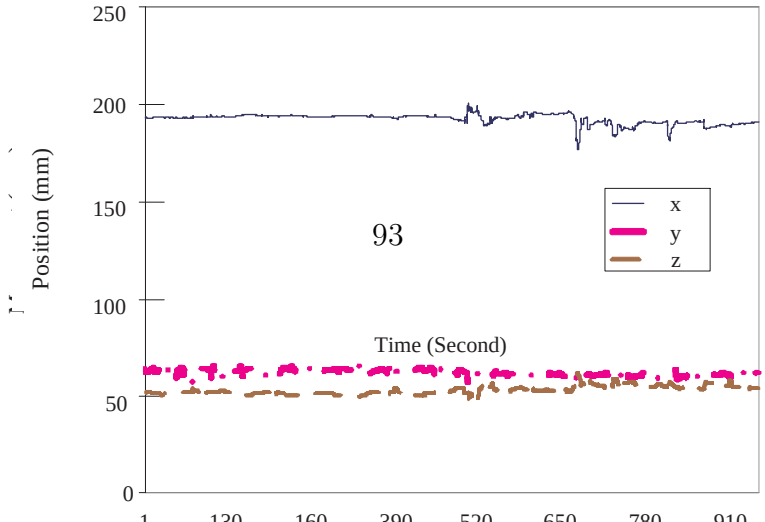

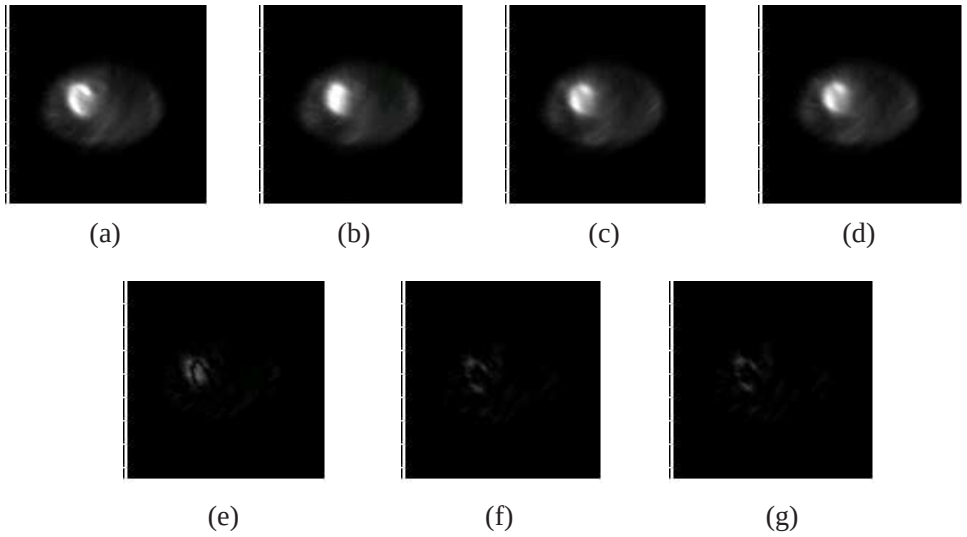

Figure 6.22: Comparison between transverse slices from the reconstructions of the third experiment. (a) 52^{th} slice from $R_{nomotion}$. (b) 52^{th} slice from $R_{no-correction}$. (c) 52^{th} slice from R_{rigid}. (d) 52^{th} slice from $R_{allcorrection}$. Note: the hot circle is the heart. (e) Difference image between the heart area of (a) and (b). (f) Difference image between the heart area of (a) and (c). (g) Difference image between the heart area of (a) and (d).

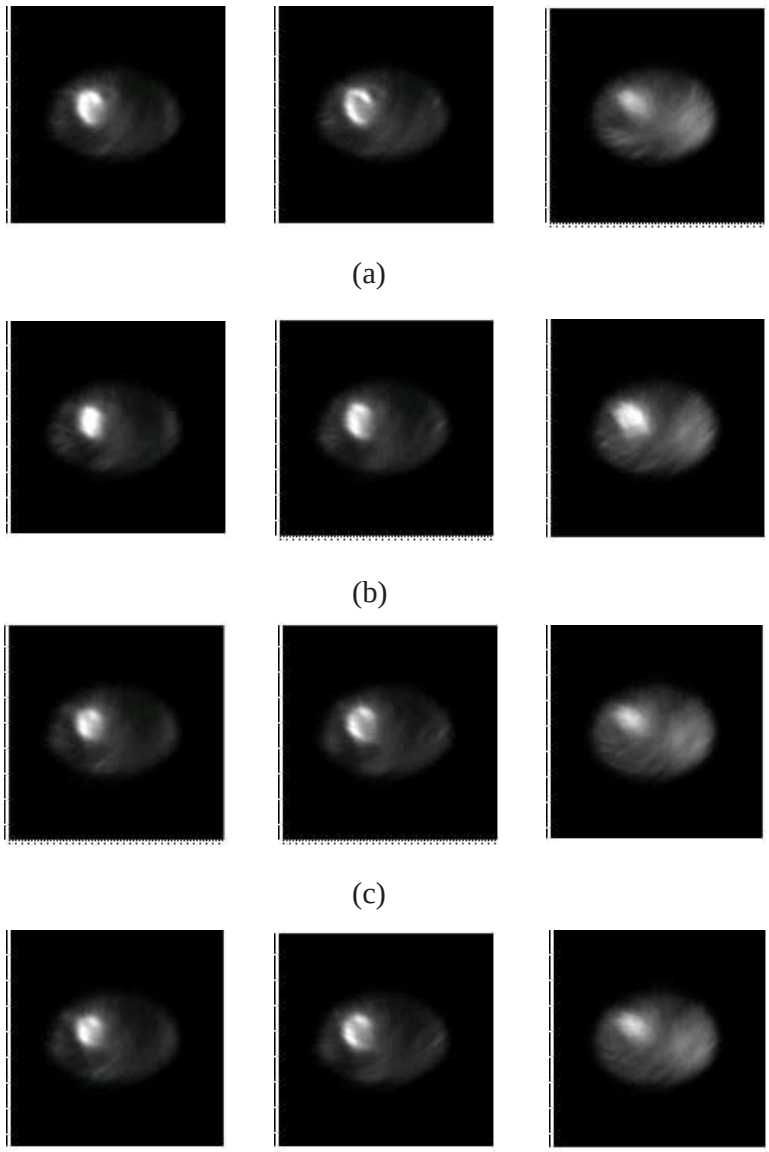

Figure 6.23: Transverse slices from the reconstructions of the third experiment. (a) Slices from $R_{nomotion}$. (b) Slices from $R_{no-correction}$. (c) Slices from R_{rigid}. (d) Slices from $R_{allcorrection}$.

Chapter 7

Discussion and Future work

We have developed methods for estimating the parameters of a model of body deformation and investigated its application to correcting the motion of markers for a human body as well as body deformation in a simulation study with moderate success. The frequency of occurrence of non-rigid body motion, its impact, and whether we can successfully separate it from respiratory motion and rigid-body patient motion in clinical studies are still open questions. We have put significant effort into investigation of respiratory and rigid-body motion, but this is our first attempt at non-rigid motion estimation and correction. It is motivated by our observation that after extracting RM and RBM components from multiple marker tracking data for patients we find cases where there is a residual motion that does not appear to be related to respiratory motion. This is illustrated in Figure 6.2, where the chest markers and abdomen markers show different extents of rotation about the body axis (twist) and change in the angulation of the planes associated with the belts (bend). Based on these observations we have started exploration into the detection and correction of these forms of deformation as our first step into non-rigid motion correction. Future studies will include an extensive investigation of the frequency of occurrence and success in separation of these types of motion in a large set of clinical acquisitions. We also anticipate more MRI based experiments to provide an anatomical assessment of our methods.

7.1 Correction of Motion of Markers on a Volunteer

Motion can cause parts of the body to move into and out of the field-of-view (FOV) of the camera heads. This happens every time there is axial motion with cardiac imaging, and can occur within the transverse plane, especially for larger patients and small FOV cardiac-dedicated SPECT systems. Since the heart is typically imaged within the central portion of the FOV, it is unlikely that such motion would lead to truncation of the heart in the projections. Thus this should not be a significant problem for visualizing the heart in cardiac SPECT. It could be a problem in portions of the slices away from the heart and in general SPECT imaging.

Our model is limited in the extent of the deformations we have included and by the number of assumptions we have employed to implement estimation and correction of deformation. Relaxation of such assumptions as the uniform progression of twist and bend of the spine between the two belts and accounting for the biomechanical properties of the other tissues of the body so that we consider more than just the spine would be good places to improve our model. One possible way to achieve such refinement would be to implement a finite-element model (FEM) of the chest and upper abdomen. FEM of this region has been performed by others (Sundaram and Feng, 1977) (Kimpara et al., 2005) (Merkle et al., 2008). We propose that such modeling be based on CT slices acquired with SPECT/CT (and PET/CT). The motion tracking could then serve to provide boundary condition information to the model such that the motion of the internal structures would be better estimated than with our current model.

7.2 Motion Separation

Motion separation is still an open topic. Though body motion is composed of three major components, RBM, RM and body deformation, the three motions are not orthogonal. RM correction usually considers individual markers only. RBM correction takes all the markers as one object and ignore the interior relative deformation. Our body deformation model considers each belt as one object and estimates the body deformation by the relative movement between the chest belt and abdomen belt. In this research, we start with the RM correction, followed by RBM correction and deformation correction. If we change the extraction order of the three components, the final

motion will be different. It is very hard to tell which order is correct. We can make some simple explanation why we extract the RM first, followed by RBM. When the patient is undergoing respiration, both abdomen belt and the chest belt will move up and down. Such high frequent oscillation is neither RBM nor deformation motion, since the heart is not moved up and down simultaneously. If we do not extract the RM first, these kind of high frequent oscillation will be considered as the RBM or deformation motion. The reconstruction will be degraded if we correct the respiratory motion with RBM or deformation correction module. Therefore, we claim that our motion correction order works for our deformation correction purposes.

Chapter 8

Contribution and Future Work

In this research, we presented a body deformation model, defined by the body twisting, body bending and bending direction. With this model, we can estimate a set of deformation parameters with multiple marker patterns. In turn, these deformation parameters and model can be used to improve the SPECT reconstruction. The correctness of our model was verified both by the marker based reversible validation and MRI based experiments. We also investigated the use of a deformation matrix based on our model in MLEM correction of deformation, and investigated how sensitive our model was to the estimation of the spine location. Compared to the reconstruction volume with deformation but no compensation, our compensated reconstruction volume shows a significant improvement. However, our correction was determined to be sensitive to the estimation of the spine location. We thus view this work as but a first step towards being able to estimate and correct patient deformation based on information obtained from marker tracking data. Since we have found a way to compensate for the deformation effects in body volume reconstruction, we applied our method to real patients. A real patient based deformation correction is done in clinic, which shows strong evidence that our method can be applied for clinical purposes in the future.

However, there is still some room for improvement. First of all, our deformation model is far from perfect. We can adopt refined spine motion modeling into our system to improve our deformation model and improve the reconstruction result. Another challenge is how to accelerate our computation speed. In this research, we only focused on the accuracy of the motion correction. Our method requires 90 minutes for one reconstruction procedure with deformation correction (1.8G hz CPU), which can be

improved a lot. Nowadays, computer hardware technology is developing very quickly. There are some hardware accelerations that probably can be used to speed up our deformation correction computation. MMX (SSE) instructions are implemented in most modern CPUs. Since a large part of our computation is projection and interpolation, we can rewrite our code with the MMX (SSE) instructions to accelerate our computation. Furthermore, the algorithms also can benefit from the modern GPGPU. The projection and back-projection computation is quite similar to volume rendering. Volume rendering algorithms are fully supported by the modern GPGPU. After restructuring our algorithm into a pipeline shape, we can use a GPGPU to accelerate the computation.

BIBLIOGRAPHY

Abdel-Aziz, Y. I. and H.M.Karara (1971). Direct linear transformation into object space coordinates in close-range photogrammetry. *Proc. Symp. Close-Range Photogrammetry*, pages 1–18.

Ablitt, N. A., Gao, J., Keegan, J., Stegger, L., Firmin, D., and Yang, G. (2004). Predictive cardiac motion modeling and correction with partial least squares regression. *IEEE Trans. Med. Imag.*, 23:1315–1324.

Armato, S. G., Giger, M. L., J.Moran, C., Blackburn, J. T., Doi, K., and MacMahon, H. (1999). Computerized detection of pulmonary nodules on ct scans. *Radiographics*, 19:1303–1311.

Armato, S. G., Giger, M. L., and MacMahon, H. (2001). Automated detection of lung nodules in ct scans: Preliminary results. *Med. Phys.*, 28:1552–1561.

Avidan, S. and Shashua, A. (2000). Trajectory triangulation: 3d reconstruction of moving points from amonocular image sequence. *IEEE Trans. on Pattern Analysis and Machine Intelligence*, 22:348–357.

Azarbayejani, A. and Pentland, A. (1995). Camera selfcalibration from one point correspondence. *Technical Report 341, MIT Media Lab.*

Beach, R. D., Depold, H., Boening, G., Bruyant, P. P., Feng, B., Gifford, H. C., Gennert, M. A., Nadella, S., and King, M. A. (2007). An adaptive approach to decomposing patient-motion tracking data acquired during cardiac spect imaging. *Div. of Nucl. Medicine*, 54:130–139.

Bittar, E., Tsingos, N., and Gascuel, M. (1995). Automatic reconstruction of unstructured 3D data: Combining medial axis and implicit surfaces. *Computer Graphics Forum*, 14(3):457–468.

Boening, G., Byrne, C. L., Gifford, H. C., Feng, B., Bruyant, P. P., Beach, R. D., and King, M. A. (2004). Motion correction for cardiac spect using a rbi-ml partial-reconstruction approach. *Nucl. Sci. Symposium Conference Record*, 21(41):2849–2853.

Boutchko, R., Balakrishnan, K., Reutter, B. W., and Gullberg, G. T. (2007). Patient motion correction in computed tomography by reconstruction on a moving grid. *MIC 2007 Conference Proceeding*, M06(7):2705–2707.

Brostow, G. and Essa, I. (1999). Motion based decompositing of video. *Seventh IEEE Inter. Con. on Computer Vision*, 1:8–13.

Bruderlin, A. and Williams, L. (1995). Motion signal processing. *SIGGRAPH 95*, pages 97–104.

Bruyant, P., Gennert, M., Nadella, S., and King, M. (2005a). The visual tracking system (vts) for patient motion detection in spect: Quality control of the stereo calibration. *IEEE Nucl. Sci. Symp. and Med. Imag. Conf.*, 5:2599–2602.

Bruyant, P., Gennert, M., Speckert, G., Beach, R., Morgenstern, J., Kumar, N., Nadella, S., and King, M. (2004). A robust visual tracking system for motion detection in spect: Improved design and validation against the polaris infra-red tracking system. *IEEE Nucl. Sci. Symp. and Med. Imag. Conf.*, 52(51):1288C1294.

Bruyant, P., Gennert, M., Speckert, G., Beach, R., Morgenstern, J., Kumar, N., Nadella, S., and King, M. (2005b). A robust visual tracking system for patient motion detection in spect: Hardware solutions. *IEEE Trans. Nucl. Sci.*, 52(5):1288–1294.

Bruyant, P. P. (2002). Analytic and iterative reconstruction algorithms in spect. *J. Nuc. Med.*, 43(10):1343–1358.

Bruyant, P. P., King, M. A., and Pretorius, P. H. (2002). Correction of the respiratory motion of the heart by tracking of the center of mass of thresholded projections : a simulation study using the dynamic mcat phantom. *IEEE Trans. Nucl. Sci.*, 49:2159–2166.

Byrne, C. (1998). Accelerating the emml algorithm and related iterative algorithms byrescaled block-iterative methods. *IEEE Tran. on Imag. Proc.*, 7:100–109.

Chablat, D. and Wenger, P. (2005). Design of a spherical wrist with parallel architecture: Application to vertebrae of an eel robot. *Proc. IEEE Int. Conf. Rob. and Automation*, pages 3336–3341.

Chen, Y., Glick, S. J., and King, M. A. (2007). Compensation of patient motion in pet using a rotator and list-mode reconstruction. *IEEE Nucl. Sci. Symp. and Medical Imaging Conf. Record*, M06-4:2692–2696.

Clough, A. V. (1986). A mathematical model of single-photon emission computed tomography. *Technical Report of University of Arizona*.

Cooper, J. and Ritter, N. (2003). Optical flow for validating medical image registration. *9th IASTED International Conference on Signal and Image Processing*, pages 502–506.

Dey, J., Feng, B., Johnson, K., Pretorius, P. H., and King, M. A. (2006). Estimation and correction of rigid and non-rigid respiration motion of the heart for spect. *Proc. 2006 IEEE Nucl. Sci. Symposium and Medical Imaging Conference*, M06(295):2111–2115.

Dey, J., Pan, T., Choi, D. J., Robotis, D. A., Smyczynski, M. S., Pretorius, P. H., and King, M. A. (2007). Investigation of respiratory motion of the heart by semi-automatic segmentation of non-contrast-enhanced 4d-ct cardiac datasets. *IEEE Trans. Med. Imag.*, M11(210):2557–2560.

Feng, B., Bruyant, P. P., Pretorius, P. H., Beach, R. D., Gifford, H. C., Dey, J., Gennert, M. A., and King, M. (2005). Estimation of the rigid-body motion from three-dimensional images using a generalized center-of-mass points approach. *IEEE Trans. Nucl. Sci.*, 53:2712–2718.

Feng, B., Gifford, H., Beach, R., Boening, G., Gennert, M., and King, M. (2006). Use of three-dimensional gaussian interpolation in the projector/backprojector pair of iterative reconstruction for compensation of known rigid-body motion in spect. *IEEE Trans. Med. Imag.*, 25:838–844.

Feng, B., King, M. A., Zeng, G. L., Pretorius, P. H., Bruyant, P. P., Beach, R., Boening, G., Jarkewicz, G., Cochoff, S., and Gagnon, D. (2003). The estimation of attenuation maps for cardiac-spect using cone-beam imaging of high-energy photons through parallel-hole collimators. *Nucl. Sci. Symposium*, 5:3262–3266.

Frey, E. C. and Tsui, B. M. W. (1993). A practical method for incorporating scatter in aprojector-backprojector for accurate scatter compensation in spect. *IEEE Trans. on Nucl. Sci.*, 40:1107–1116.

Frey, E. C. and Tsui, B. M. W. (1997). A new method for modeling the spatially-variant object-dependent scatter response funtion in spect. *Conf. Rec. Nucl. Sci. Symposium and Med. Imag. Conf.*, 32:1082–1086.

Fujioka, H., Inoue, T., and Ishimaru, Y. (1997). Compton-scatter correction using the triple energy window (tew) method in conventional single photon emission computed tomography without tew acquisition hardware. *J. Kaku Igaku*, 34(4):251–258.

Ganapathy, S. (1984). Decomposition of transformation matrices for robot vision. *Proc. IEEE Int. Conf. Robotics Automat*, 1:130–139.

Garbow, J. R., Dugas, J. P., and Conradi, M. S. (2003). Respiratory gating for mri and mrs in rodents. *Proceedings of the Third IEEE Symposium on BioInformatics and BioEngineering (BIBE03)*, page 126.

G.T.Gullberg (2004). Dynamic spect imaging: exploring a new frontier in medical imaging. *Biomedical Imaging: Nano to Macro. IEEE International Symposium on*, 1:607–610.

Hartley, R. and Zisserman, A. (2000). *Multiple View Geometry in Computer Vision.*

Horn, B. K. P., Hilden, H. M., and Negahdaripourt, S. (1988). Closed-form solution of absolute orientation using orthonormal matrices. *Optical Society of America*, 5:1127–1135.

Horn, B. K. P., Hilden, H. M., and Negahdaripourt, S. (2003). Volume-preserving nonrigid registration of mr breast images using free-form deformation with an incompressibility constraint. *IEEE TRANS. MED. IMAG.*, 22(6):730–741.

Hudson, H. M. and Larkin, R. S. (1994). Accelerated image reconstruction using ordered subsets of projection data. *IEEE Trans. Med. Imag.*, 13:601–609.

Ichihara, T., Ogawa, K., Motomura, N., Kubo, A., and Hashimoto, S. (1993). Compton scatter compensation using the triple-energy window method for single- and dual-isotope spect. *J. Nucl. Med.*, 34:2216–2221.

Isaksson, M., Jalden, J., and Murphy, M. J. (2005). On using an adaptive neural network to predict lung tumor motion during respiration for radiotherapy applications. *J. Med. Phy.*, 32(12):3801–3809.

James, A., Phelps, and Sorenson, M. E. (2004). Physics in nucl. medicine.

Kimpara, H., Lee, J. B., and Yang, K. H. (2005). Development of a three-dimensional finite element chest model for the 5th percentile female. *J. Stapp Car Crash*, 49:251–269.

Kovalski, G., Israel, O., Keidar, Z., Frenkel, A., Sachs, J., and Azhari, H. (2007). Correction of heart motion due to respiration in clinical myocardial perfusion spect scans using respiratory gating. *J. Nucl. Med.*, 48(4):630–636.

Krol, A. (2001). An em algorithm for estimating spect emission and transmission parameters from emission data only. *IEEE Trans. Med. Imag.*, MI-20(3):218–232.

Krol, A., Echeruo, I., Salgado, R. B., Lipson, E., Bowsher, J. E., Feiglin, D. H., and Thomas, F. D. (2002). Emintra spect algorithm with ordered subsets (osemis) for non-uniform attenuation correction in cardiac imaging. *Proc. of SPIE*, 4684:1022–1027.

Kuhl, D. and Edwards, R. (1963). Image separation isotope scanning. *Radiology*, 80:653–662.

Kyme, A. Z., Hutton, B. F., Hatton, R. L., Skerrett, D. W., and Barnden, L. R. (2003). Practical aspects of a data-driven motion correction approach for brain spect. *IEEE Trans. Med. Imag.*, 22(6):722–729.

Lalush, D. and Tsui, B. (2000). Performance of ordered-subset reconstruction algorithms under conditions of extreme attenuation and truncation in myocardial spect. *J. Nucl. Med.*, 41:737–744.

Lamare, F., Busch, M., Brinks, R., Clairet, J., Bruyant, P., and Visvikis, D. (2007). Local respiratory motion correction (lrmc) for pet/ct imaging. *IEEE Trans. on Nucl. Med.*, 48:196.

Lange, K. and Carson, R. (1984a). Em reconstruction algorithm for emission and transmission tomography. *J. Comp. Assist. Tomog.*, 8:306–316.

Lange, K. and Carson, R. (1984b). Em reconstruction algorithms for emission and transmission tomography. *J. Comput. Assist Tomogr.*, 8:306–316.

Lee, K. and Arjunan, S. (1991). A three-degrees-of-freedom micromotion in-parallel actuated manipulator. *IEEE Trans. on Rob. and Automation*, 7(5):634–641.

Len, R. K. and Tsai, R. Y. (1987). Techniques for calibration of the scale factor and image center for high accuracy 3d machine vision metrology. *IEEE Int. Conf. Robotics Automat.*, 5(10):68–75.

Li, J., Jaszczak, R. J., Greer, K. L., and Coleman, R. E. (1994). A filtered backprojection algorithm for pinhole spect with a displaced centre of rotation. *Phys. Med. Biol.*, 39:165–176.

Livieratos, L., Rajappan, K., Stegger, L., Schafers, K., Bailey, D. L., and Camici, P. G. (2006). Respiratory gating of cardiac pet data in list-mode acquisition. *Eur. J. Nucl. Med. Mol. Imaging.*, 33(5):584–588.

M. A. King, D. J. deVries, T.-S. P. P. H. P. and Case, J. A. (1997). An investigation of the filtering of tew scatter estimates used to compensate for scatter with ordered subset reconstructions. *IEEE Trans. on Nucl. Sci.*, 44:1140–1145.

Maiocchi, R. *3-D character animation using motion capture.*

Marie, P., Djaballah, W., Franken, P. R., Vanhove, C., Muller, M. A., Boutley, H., Poussier, S., Olivier, P., Karcher, G., and Bertrand, A. (2005). Osem reconstruction, associated with temporal fourier and depth-dependant resolution recovery filtering, enhances results from sestamibi and 201tl 16-interval gated spect. *J. Nucl. Med.*, 46(11):1789–1795.

McNamara, J. E., Bruyant, P. P., Johnson, K., Feng, B., Lehovich, A., Gu, S., Gennert, M. A., and King, M. A. (2006). An assessment of a visual tracking system *vts* to detect and compensate for patient motion during spect. *Nuclear Science Symposium Conference Record*, 6:3235–3238.

McNamara, J. E., Feng, B., Johnson, K., Gu, S., Gennert, M. A., and King, M. A. (2007). Motion capture of chest and abdominal markers using a flexible multi-camera motion-tracking system for correcting motion-induced artifacts in cardiac spect. *Record of IEEE NSS-MIC*, M26(60):4289–4294.

MedserVentures-Inc. http://www.medserventures.com/.

Merkle, A. C., Ward, E. E., O'Connor, J. V., and Roberts, J. C. (2008). Assessing behind armor blunt trauma (babt) under nij standard-0101.04 conditions using human torso models. *J. Trauma*, 64:1555–1561.

MIRG. http://www.phas.ubc.ca/mirg/.

Mitra, J., McNamara, J. E., Johnson, K. L., Dey, J., and King, M. A. (2007). Estimation of rigid-body and respiratory motion of the heart for spect motion correction. *Conference Record of IEEE NSS-MIC*, M18(326):3570–3576.

Mukherjee, J. M., McNamara, J. E., Johnson, K. L., Dey, J., and King, M. A. (2009). Estimation of rigid-body and respiratory motion of the heart from marker tracking data for spect motion correction. *IEEE Trans. Nucl. Sci.*, 56:147–155.

Natterer, F. (1993). Determination of tissue attenuation in emission tomography of optically dense media. *Inverse Problems*, 9:731–736.

Noumeir, R. and El-Daccache, R. (1998). Attenuation correction in spect using active surfaces. *Nucl. Sci. Symposium*, 3:1995–1999.

Noumeir, R., Mailloux, G. E., and Lemieux, R. (1996). Use of an optical flow algorithm to quantify and correct patient motion during tomographic acquisition. *ICIP*, 3:559–562.

Ogawa, K., Harata, Y., Ichihara, T., Kubo, A., and Hashimoto, S. (1991). A practical method for position-dependent compton-scatter correction in single photon emission ct. *IEEE Trans. Med. Imag.*, 10:408–412.

Paik, D. S., Beaulieu, C. F., Rubin, G. D., Acar, B., Jeffrey, R. B., Yee, J., Dey, J., and Napel, S. (2004). Surface normal overlap: A computer-aided detection algorithm with application to colonic polyps and lung nodules in helical ct. *IEEE Trans. Med. Imag.*, 23(6):661–675.

Park, C., Kim, S., Kim, H., and Lee, I. (2005). Real-time marker-free motion capture system using blob feature analysis. *Presented at the Society of Photo-Optical Instrumentation Engineers (SPIE) Conference*, 5671:237–246.

Reyes, M., Malandain, G., Koulibaly, P. M., Gonzlez-Ballester, M. A., and Darcourt, J. (2007). Model-based respiratory motion compensation for emission tomography image reconstruction. *Phys. Med. Biol.*, 52:3579–3600.

Rozumalski, A., Schwartz, M., Wervey, R., Swanson, A., Dykes, D., and Novacheck, T. (2007). The in vivo three-dimensional motion of the human lumbar spine during gait. *Gait and Posture*, 38:378–384.

Rueckert, D., Sonoda, L., Hayes, C., Hill, D., Leach, M., and Hawkes, D. (1999). Nonrigid registration using free-form deformations: application to breast mr images. *IEEE Trans. Med. Imag.*, 18(8):712–721.

Schumacher, H. and Fischer, B. (2007). A new approach for motion correction in spect imaging. *Bildverarbeitung fur die Medizin 2007*, 3:51–55.

Shepp, L. and Vardi, Y. (1982a). Maximum likelihood reconstruction for emission tomography. *IEEE Trans. Med. Imag.*, 1:113–121.

Shepp, L. and Vardi, Y. (1982b). Maximum likelihood reconstruction for emission tomography. *IEEE Trans. Med .Imag.*, pages 113–122.

SNM (2007). About nucl. medicine.

Sundaram, S. H. and Feng, C. C. (1977). Finite element analysis of the human thorax. *J. Biomechanics*, 10:505–516.

Sundaresan, A. and Chellappa, R. (2005). Markerless motion capture using multiple cameras. *CVIIE '05: Proceedings of the Computer Vision for Interactive and Intelligent Environment (CVIIE'05)*, pages 15–26.

Svoboda, T., Martinec, D., and Pajdla, T. (2005). A convenient multi-camera self-calibration for virtual environments. *Teleoperators and Virtual Environments*, 14(4):407–422.

Tsai, R. (1987). A versatile camera calibration technique for high-accuracy 3d machine vision metrology using off-the-shelf tv cameras and lenses. *IEEE J. Robotics Automat*, 3(4):323–344.

Tsai, R. Y. (1986). An efficient and accurate camera calibration technique for 3d machine vision. *Proc. of IEEE Conf. on Computer Vision and Pattern Recognition*, 1614:364–374.

Ue, H., Haneishi, H., Iwanaga, H., and Suga, K. (2005). Motion correction of respiratory-gated spect image and clinical usefulness of the extracted motion information. *Conference Record of 2005 IEEE Nucl. Sci. Symposium*, 4:2418–2422.

Vorro, J. and Johnston, W. L. (2003). A myoelectric model for thoracic spinal motion dynamics during clinical rotation test: Part 1. ipsilateral regional motor performance. *American Osteopathic Association*, 103(5):187–193.

Wang, S. and Royal, H. (1996). Diagnosis: Cavernous hemangioma.

Welch, A., Gullberg, G. T., Christian, P. E., Datz, F. L., and Morgan, H. T. (1995). A transmission-map-based scatter correction technique for spect in inhomogeneous media. *J. Med. Phy.*, 22(4):1627–1635.

Welch, A. S. (1997). Toward accurate attenuation correction in spect without transmission measurements. *IEEE Trans. Med. Imag.*, MI-16(5):532–541.

Witkin, A. and Popovi'c, Z. (1995). Motion warping. *SIGGRAPH 95*, pages 105–108.

Xu, D. and He, Z. (2006). Filtered back-projection in 4π compton imaging with a single 3d position sensitive cdznte detector. *IEEE Trans. on Nucl. Sci.*, 53(5):2787–2795.

Yang, B. P., Chen, L. A., and Ondra, S. L. (2007). A novel mathematical model of the sagittal spine: application to pedicle subtraction osteotomy for correction of fixed sagittal deformity. *J. Spine*, 8:359–366.

Zhang, Z. (1999). Flexible camera calibration by viewing a plane from unknown orientations. *Inter. Conf. on Computer Vision*, pages 666–673.

Zhang, Z. (2000). A flexible new technique for camera calibration. *IEEE Trans. on Pattern Analysis and Machine Intelligence*, 22(11):1330–1334.

Zhou, L. (2001). Structure and nonrigid motion analysis from 2d images.